University of Washington

Graduate School

This is to certify that I have examined this copy of a doctoral dissertation by

David J. Reiss

and have found that it is complete and satisfactory in all respects,
and that any and all revisions required by the final
examining committee have been made.

Chair of Supervisory Committee:

_____

Professor Christopher Stubbs

Reading Committee:

_____

Dr. Christopher Stubbs

_____

Dr. Craig Hogan

_____

Dr. Scott Anderson

Date: _____

In presenting this dissertation in partial fulfillment of the requirements for the Doctorial degree at the University of Washington, I agree that the Library shall make its copies freely available for inspection. I further agree that extensive copying of this thesis is allowable only for scholary purposes, consistant with "fair use" as prescribed in the U.S. Copyright Law. Requests for copying or reproduction of this dissertation may be referred to University Microfilms, 1490 Eisenhower Place, P.O. Box 975, Ann Arbor, MI 48106, to whom the author has granted "the right to reproduce and sell (a) copies of the manuscript in microform and/or (b) printed copies of the manuscript made from microform."

Signature_____

Date_____

University of Washington

Abstract

The Rate of Supernovae in the Nearby and Distant Universe

by David J. Reiss

Chair of Supervisory Committee

Professor Professor Christopher Stubbs
Astronomy

I present a measurement of the rate of supernovae (SNe) in nearby field and cluster galaxies, plus in distant field galaxies. The nearby rates are computed from the SNe discovered during the Mount Stromlo Abell Cluster SN Search (MSACSS), whose design, implementation, and results I discuss in detail. The distant rates are measured from the *High-Z* SN search, as a secondary result of the quest to measure the acceleration of the expansion of the universe using type-Ia SNe. The rates presented here provide a means of tracing the progenitor populations of the SNe through the ages of their host galaxies. In general, it is found that the rate of type-Ia SNe is largely independent of the age of the underlying stellar population, implying that the mean lifetime of SN-Ia progenitors is $\gtrsim 1$ Gyr, although there appears to be some evidence that their lifetimes must be shorter than a few Gyr. The rate of core-collapse SNe, as expected, seems to follow the same trend of star-formation in the field relative to clusters. Unfortunately the statistical and systematic uncertainties in these rates are large, and the significance of any of these trends is only at the ~ 1-σ level. However, the results do reveal the strength of using a *comparison* of SN

rates of various types and among different galaxy populations to constrain quantities from the nature of SN Ia progenitors to the star-formation and enrichment histories of the universe, to certain cosmological parameters. A measurement of supernova rates per unit volume independently confirms the previously-reported observation that the star-formation rate appears to have decreased markedly in the past few Gyr.

SUMMARY OF THESIS RESULTS:

1. *Cluster SN rates:* The rate of SNe in clusters is $0.180^{+0.054\ +0.046}_{-0.054\ -0.058}$ $(H_0/65)^2$ SNu (SNe Ia) and $0.124^{+0.076\ +0.085}_{-0.076\ -0.052}$ $(H_0/65)^2$ SNu (core-collapse SNe). Rates are also computed in SNu_R: 0.164 and 0.115 SNu_R for SNe Ia and core-collapse SNe are derived, respectively (with similar uncertainties). We find that the rates are (0.166 ± 0.065) and (0.159 ± 0.084) SNu for Ia and core collapse SNe in the bluer clusters and (0.209 ± 0.083) and (0.074 ± 0.097) SNu in the redder clusters.

2. *Nearby field SN rates:* The rate of SNe in nearby field galaxies are found to be $0.164^{+0.058\ +0.050}_{-0.058\ -0.056}$ $(H_0/65)^2$ and $0.997^{+0.54\ +1.21}_{-0.54\ -0.47}$ $(H_0/65)^2$ SNu, for type Ia and core-collapse SNe, respectively. These rates are $0.906 \pm 0.43 \pm 0.25$ and $7.8 \pm 2.4 \pm 0.58$ times those derived in the nearby rich clusters (errors are reduced after certain systematics cancel). In SNu_R the rates are 0.152 and 0.934 $(H_0/65)^2$ SNu, for SNe Ia and core collapse events. The SN Ia rate agrees well with previous measurements, whereas the core-collapse SN rate appears to be slightly higher than earlier estimates.

3. *"Unusual" SN rates:* Upper limits to the rates of "unusual" SNe like SN 1987A (extremely faint) and SN 1997cy (extremely luminous) are derived from the nearby search, and are found to be $\lesssim 0.8$ SNu and $\lesssim 6.6 \times 10^{-3}$ SNu, respectively.

4. *High-z SN rates:* We derive high-z rates (at mean redshifts of ~ 0.49) for SNe Ia and core-collapse events of $0.278^{+0.091\ +0.133}_{-0.091\ -0.120}$ $(H_0/65)^2$ SNu, and $r_{\mathrm{II}} \geq 0.423^{+0.71\ +0.33}_{-0.71\ -0.24}(H_0/65)^2$ SNu, respectively (the type-II rate being a lower limit).

Our R-band SN rates are $0.257\ (H_0/65)^2$ SNu_R for SNe Ia and $\geq 0.394(H_0/65)^2$ SNu_R for SNe II (with similar uncertainties to those derived in SNu).

5. *SN rates per unit volume:* We also derive rates per unit volume. We find High-z rates of $(0.66 \pm 0.24)(H_0/65)$ SNv and $\geq (0.92 \pm 0.92)(H_0/65)$ SNv, for SNe Ia and SNe II, in units of $1\,\mathrm{SNv} \equiv 1\,(\mathrm{Century} \times [10^{-2}\mathrm{Mpc}^3])^{-1}$ (recall that the SN II rate is a lower limit). The corresponding nearby SN rates are $(0.20 \pm 0.074)(H_0/65)$ SNv (type-Ia) and $(1.37 \pm 0.67)(H_0/65)$ SNv (type-II). The rates of both types of SNe have decreased significantly, *per unit volume*, during the past ~ 5Gyr.

TABLE OF CONTENTS

LIST OF FIGURES

LIST OF TABLES

ACKNOWLEDGMENTS

0.1 Acknowledgements

The author wishes to express sincere appreciation to Dr. Brian P. Schmidt, Mount Stromlo and Siding Springs Observatory for his generosity and guidance. I would also like to thank the observatory director at MSSSO for his selection of the Mount Stromlo Abell Cluster Supernova Search project for director's discretionary time. I am grateful to M. Postman, T. Lauer, and M. Strauss for donating their compilation of cluster data for our target selection, and to A. Riess for insightful comments on Chapter 1 of the manuscript. This research is supported by NSF grant AST 9617036 and by grants from the Seaver Institute and the Packard Foundation to the University of Washington.

Chapter 1

THE MOUNT STROMLO ABELL CLUSTER SUPERNOVA SEARCH: METHODS, TECHNIQUES, AND RESULTS

1.1 Abstract

We have recently completed a 2-1/2-year project to find supernovae (SNe) in a well-defined sample of high-density southern Abell clusters with redshifts $z \leq 0.08$. These observations have provided a volume-limited sample of SNe Ia to more than a magnitude below their peak brightness, and will enable us to: (1) measure the luminosity function of SNe, (2) further explore the correlation of light curve shape with the absolute luminosity of SNe Ia to better understand SNe Ia as distance indicators, (3) measure SN rates, (4) measure the bulk motion of the Local Group using SNe Ia, and (5) directly compare SN Ia distances to brightest cluster galaxy distances. We used the MaCHO wide-field 2-color imager on the 1.3m telescope at Mount Stromlo to routinely monitor $\sim$ 12 clusters per week. We describe our technique for target selection and scheduling search observations, and for finding and identifying SN candidates. We also describe the results from our program, including the detection of 52 SNe, several RR-Lyrae variables, and hundreds of asteroids.

1.2 Motivation

As extremely luminous point sources which represent a discrete physical event, SNe are attractive indicators of extragalactic distances. The CTIO/Calán group (Hamuy *et al.* 1995; Hamuy *et al.* 1996b) demonstrated that Type Ia SNe are not standard candles but instead show a range in peak luminosity of approximately one magnitude in V. However, they also proved that there exists a tight correlation between decline rate and peak brightness for SNe Ia in the sense that more luminous events decline more slowly than intrinsically faint ones (Phillips 1993). This property of SN Ia light curves provides a means to accurately estimate the intrinsic luminosity of the SN, thereby sharpening the precision of SNe Ia as standard candles to better than $\sigma_V < 0.2^m$. A somewhat more elaborate method developed by Riess, Press, & Kirshner 1995a, 1996 uses multi-band light curve shapes to estimate the luminosity of type Ia SNe and also predicts distance uncertainties and extinction for individual SNe. Using a sample of 20 SNe drawn from Hamuy *et al.* 1996c and their own observations, they were able to improve the distance estimate for each, decreasing the scatter in the Hubble diagram to $\sigma = 0.12^m$ (distance error of 6%).

For type Ia SNe to be useful for measuring distances, they must be discovered near peak brightness. Searches based on infrequent observations typically produce SNe that are too old to obtain good followup photometry and measure well-sampled light curves. In a systematic search in which each field is revisited periodically, the ages of any discovered SNe are constrained to be less than the time since the field was last observed. Such frequent visits enable more accurate light-curve shape measurements, and thus, more accurate distances. Systematic searches for distant SNe ($z \gtrsim 0.4$) are currently being carried out by Perlmutter *et al.* 1997 and Schmidt *et al.* 1997 while nearby searches are being conducted by groups at the Beijing Astronomical Observatory (d. Li *et al.* 1997), the Perth Observatory (Martin, Williams, & Woodings 1997), U.C. Berkeley (Treffers *et al.* 1997), and by R. Evans (Evans 1997).

These searches fill in the distant and nearby ends of the Hubble diagram, respectively. Though many SNe have been found at $0.002 < z < 0.2$, selection effects plague most samples, and are nearly impossible to quantify. A well-understood, complete sample of SNe in this intermediate distance range is needed so that we can understand the uncertainties and biases which arise from calibrating the distant samples using the nearby objects. The search described in this chapter has been optimized for finding SNe over the range of redshifts $0.02 \leq z \leq 0.08$ with a completeness limit fainter than $V > 20$. Complimentary searches scanning lower-redshift Abell clusters (Maza 1997) and Northern hemisphere Abell clusters (Adams *et al.* 1997) have also been initiated. The SNe produced by these searches, when combined with objects from the nearby and distant searches, will comprise a sample of SNe encompassing a broad range of distances with which we can accurately map out the expansion of the Universe from $0.002 \leq z \leq 1.0$.

To understand the systematics involved in using SNe as distance indicators, we need to better understand the SNe, their evolution, and their progenitors. Supernova rates, for example, place important constraints on models of progenitor evolution and the physical processes involved in the explosions, in addition to star formation and chemical enrichment. However, they are still subject to dispute, particularly due to interpretations of selection effects and control times and the large statistical uncertainties of small samples (see Cappellaro *et al.* 1993a, Tammann 1990). Our sample is unique in that it is volume-limited to more than a magnitude below the SN Ia average brightness for our most distant clusters, and its selection criteria are well understood. These properties will allow us to estimate and compare rates of SNe of different types, both in the clusters and in the field surrounding them.

Knowledge of the luminosity distribution of SNe Ia would enable us to place constraints on the systematics (such as Malmquist bias) introduced by using SNe Ia as distance indicators. However, the SN Ia luminosity function is largely unknown due to poor understanding of the selection effects of past searches (but see Hamuy

& Pinto 1999). An important aspect of this is the evolution of the luminosities of SNe Ia. Hamuy *et al.* 1996b have shown that there appears to be an intrinsic difference in the peak luminosity–decline-rate relationship between the nearby Phillips 1993 sample and their more distant sample of SNe Ia. In addition, there appears to be a strong correlation between the decline rate of SNe Ia and the host galaxy type; SNe Ia that occur in early-type galaxies have preferentially narrower light curves than those in their spiral counterparts. Fortunately, after correcting for light curve shape, there is no detectable difference between distances measured to early- and late-type galaxies (Schmidt *et al.* 1998). Our SN sample should allow us to construct a SN Ia luminosity function and to explore the effects of the host galaxy type, progenitor stellar population ages, and environment (cluster vs. field) on SN luminosities. This will enable us to place limits on these evolutionary effects and to estimate any biases which they might introduce into estimates of the deceleration parameter q_0 via SNe Ia.

The intermediate-distance SNe are also ideally suited for measuring the reflex motion of the Local Group (LG), unhindered by random peculiar velocities of nearby galaxies or large uncertainties in measuring distances of very distant objects. Lauer and Postman (1994) [LP94] determined distances to Abell clusters within $z < 0.05$ using brightest cluster galaxies (BCG) as distance indicators with an accuracy of 16%. Their controversial result suggested that these clusters participate in a large bulk motion (560 km sec^{-1}) pointing nearly 70° away from the direction of the dipole in the microwave background (CMB) as measured by COBE (Fixsen *et al.* 1994). The amplitude of their measurement within such a large volume contradicts many currently popular models (Feldman & Watkins 1994, Strauss *et al.* 1995). While other studies of Abell clusters (Hudson & Ebeling 1997, Branchini, Plionis, & Sciama 1996) have questioned the significance of the LP result, other reanalyses (Colless 1995, Graham 1996) have supported their claims, and simulations have confirmed the notion that dense clusters can readily be used to trace the large-scale

structure of the universe (Gramann *et al.* 1995).

Studies of large-scale motions using other distance estimators have since been attempted to test the validity of the LP result. In particular, Riess, Press, & Kirshner 1995b [RPK95] used a sample of 13 SNe Ia to measure peculiar velocities to galaxies in the field. Using the uncertainties in the SN Ia distance measurements which are computed directly from their multi-color light-curve shapes technique, they found that they can rule out the LP measurement at a confidence level better than 99.3%. Moreover, their velocity estimate is consistent with a bulk motion of similar amplitude and direction to the velocity dipole in the CMB. Still other peculiar velocity samples constructed using different distance indicators, such as Tully-Fisher measurements (Giovanelli *et al.* 1996), also seem to disagree with LP94. However, Watkins & Feldman 1995 argued that in contrast to the BCG sample of LP94, these more recent measurements are sensitive to small-scale motions, to different degrees (since motions of rich galaxy clusters are less sensitive to small-scale flows than are typical field galaxies) and this significant source of noise reduces their overall sensitivity to the large-scale motions. Therefore, because these samples probe different locations in space where the small-scale flows differ, this results in decreasing, but not eliminating, the significance of the disagreement between the bulk motion measurements of LP94 and RPK95 (and by extension the Tully-Fisher measurements of Giovanelli *et al.* 1996).

The Abell cluster targets in this search are a subset of the clusters currently being observed as part of a larger BCG survey by Postman, Lauer and Strauss (PLS). The resulting sample of cluster peculiar velocities from SNe Ia will be directly comparable to the BCG measurements which will emerge from the LP94 + PLS surveys, allowing a direct comparison of SN Ia distances and BCG distances to many clusters. This will enable us to measure the reflex motion of the LG with respect to a subset of the LP94 + PLS clusters using an independent distance indicator which offers significantly increased precision, and which can be directly compared to that of LP94

and/or PLS, in contrast to the other surveys mentioned above. The contribution that this SN search can make to the bulk motion question is examined in detail in Section 1.7. Finally, the large-scale velocity field of Abell clusters derived from our sample of SNe can be compared to those predicted by the gravity fields of all-sky galaxy catalogs and simulations, to test models of structure formation and constrain $\Omega_0^{0.6}/b$, where b is the biasing parameter, similar to the analysis performed on a sample of 25 SNe Ia in the field by Riess *et al.* 1997.

Additional projects of interest which may emerge from this project include: (1) placing limits of low-mass intracluster MaCHOs ($\sim 10^{-4} M_{\odot}$) by trying to detect microlensing light curves on top of the light curves of SNe which are found on the far side of their cluster fields (Kolatt & Bartelmann 1998), (2) detecting the tidal disruption and accretion of stars into the central black holes of AGN through flares in the AGN luminosity (Evans & Kochanek 1989), and (3) detecting RR-Lyrae in the halo of our galaxy, useful for tracing its kinematics.

1.3 Search Strategy

The difficulty in searching for intermediate-distance supernovae is that one cannot practically target individual galaxies with short exposure times as in nearby searches, while the volumes (and galaxy numbers) being sampled are much smaller than those in the high-redshift searches. One must survey a large area of sky at locations where the galaxy number density is the largest at the desired distance, using an intermediate-sized telescope. The Mount Stromlo Abell Cluster Supernova Search employs the MaCHO wide-field ($45' \times 45'$) dual-color mosaic imager (Stubbs *et al.* 1993) on the MSSSO 1.3m telescope (Hart *et al.* 1996). The camera's passbands are not standard and we refer to them as V_M for the 'blue' side and R_M for the red side. We specifically target all high-density ($N_{gal} \equiv$ number of galaxies within one Abell radius ≥ 65) clusters from the Abell, Colowin and Owen (ACO, 1989)

survey of nearby, rich galaxy clusters. The target clusters are further constrained to lie within $z \leq 0.08$ as measured in the BCG survey of PLS, and to be accessible at reasonable altitude from Stromlo ($\delta(J2000) \leq +15$). The complete sample of 74 clusters is listed in Table 1.3; their distribution in the sky is displayed in Figure 1.1. In all there are 20 clusters in our sample whose BCG distances were measured by LP94. Note that the sample's large-scale distribution on the sky is not uniform; in particular nearly 1/6 of the target clusters are located in the direction of the Shapely-Ames Supercluster near $(l, b) \simeq (315, +30)$.

Our project has been allocated 5% of the telescope time on the 1.3m, the remaining 95% belonging to the MaCHO project, with all of our images being observed by the MaCHO staff observer. A typical SN Ia at $z = 0.08$ has $M_B \simeq 18.5$ near maximum light. Type II and Ib/c SNe are 0 to 5 magnitudes fainter. In order to be complete in detecting point sources at 20th magnitude, the faintest objects which we can readily follow up with photometry and spectroscopy, with $2.5''$ FWHM seeing that is typical at MSO (Figure 1.2 shows the distribution of observed FWHM over the past year), we take 240-second exposures of each field. Therefore we have enough time to average ~ 4 to 5 observations night^{-1}. The telescope time is most efficiently used (with less overhead) by observing ~ 14 fields every third night. Allowing for weather ($\sim 50\%$), we average ~ 14 fields per week, enough to observe $\sim 1/3$ of the 74 fields in the two-week period that it takes for a SN Ia to reach peak brightness.

The Macho camera's pixel scale of $0.628''$/pixel, combined with the $\sim 2.5''$ typical FWHM, allows for good sampling of the PSF, which is important in the image subtraction process used to detect SNe, as described in §1.5. The dual mosaic focal plane is read out at 16 separate amplifiers, resulting in 15 separate 1024×2048-pixel images (8 in blue and 7 in red because of one dead amplifier) which sample the entire $45'$ field. This also is advantageous for the subtraction process, as will be explained below.

High-quality and frequent followup photometric and spectroscopic observations

are extremely important for the success of this project. In addition to the images from the 1.3m, [1] we obtain regularly scheduled observations on the MSSSO 2.3m (spectra and imaging), and the MSSSO 1.9m. The ARC 3.5m is also employed for spectroscopic followup on SNe detected at $\delta \gtrsim -30$. In addition, we use a semi-dedicated (shared with the MaCHO group) $30''$ at MSSSO as our main source of photometric coverage. The nightly observations are conducted by the RAPT group of amateur astronomers and observers, who are an invaluable asset to this program. [2]

1.4 Scheduling and Data Collection

An automated scheduling routine is used to determine which fields (of those that satisfy the criteria described in §1.3) are best for observing on a given night, and at what time. The algorithm is summarized below:

1. A field is ineligible for observing on any given night if:
   (a) its hour angle at evening twilight is $\mathrm{HA}_{eve} > 2$ hours, or
   (b) its hour angle at morning twilight is $\mathrm{HA}_{morn} < -4$ hours. This ensures that the clusters will be observable for at least 6 weeks (allowing sufficient followup).

2. Assign a weight w_i (which is a function of time, t) to each of the remaining fields, i:

$$w_i(t) = \left(\frac{N_{days,i}}{21}\right)^2 \times \frac{N_{gal,i}}{100} \times \frac{X_i(t)}{X_{min,i}}, \tag{1.1}$$

[1] The non-standard V_M and R_M passbands can be accurately transformed to rest-frame V and R_C (0.01 mag r.m.s.) as described by Kim, Goobar, & Perlmutter 1996, because they are well matched to these filters redshifted to $z \simeq 0.06$ (Reiss *et al.* 1999a).

[2] For more information on the RAPT group, please see http://www.tip.net.au/~bnc/.

where $N_{days,i}$ is the number of days since the i^{th} field's last observation, $N_{gal,i}$ is its ACO galaxy count, $X_i(t)$ is its current airmass, and $X_{min,i}$ is the minimum airmass which it reaches at Mount Stromlo.

(a) Special consideration is taken for fields which are being observed for the first time this season so that they don't dominate the schedule.

(b) If the night is dark and the seeing good (better than 2″), weights for fields which have not yet been observed are artificially inflated to allow more template observations on good nights (see §1.5.1).

(c) Weights for fields which have been observed within the past week are artificially reduced so they cannot be observed at the expense of other fields.

(d) Individual clusters can be given higher priority, as desired, for example, to increase the frequency of observations made of clusters with current SNe, or those with possible SNe which need confirmation.

3. The time, t_c, which maximizes the sum of weights of all observable fields, $\sum_i w_i(t)$, is chosen as the best time to observe.

4. Queue the fields which are observable at time t_c by their weight $w_i(t_c)$, filling up the allocated 15% of the night (including time for CCD readout and telescope slewing). [3]

(a) Skip those clusters which lie less than 20° from the moon.

(b) Also skip those clusters which lie at $X_i(t_c) > 2.0$.

[3]Though steps 4a and 4b logically should come prior to step 3, our scheduling follows this sequence so that we do not use more than our 5% share of dark time on the 1.3m. There are usually sufficient numbers of clusters needing observations that this procedure does not result in any wasted observing time.

(c) Fields are scheduled with their total observing time $\propto z_{clust}$. The observations of clusters within 10° of the ecliptic are divided into two observations (to help identify asteroids).

5. Sort the scheduled fields by their azimuthal angle to provide the telescope with the shortest slewing path between observations.

The routine creates a 'scheduler file' which lists the coordinates of the scheduled fields; this is fed directly into the MaCHO camera/telescope controller system at the requested time, t_c. The automated system takes over at that point until all exposures are finished. The resulting bias-subtracted, flat-fielded images are then copied to local disk for analysis.

The amount by which each factor in Eq. 1.1 contributes to the cluster weights has been tuned so that on average, each cluster is revisited every fortnight – even those with the lowest galaxy counts in our sample. This system has worked extremely well; to date $\sim$ 4.7% of the usable telescope time has been used to observe Abell clusters. As shown in Figure 1.3 (top), for the observations of the past year, the median time-between-observation (Δt) of each field is 12 to 15 days, with a strongly peaked distribution (this histogram also includes the observations taken during the first few months of the search, in which the scheduler was being 'tuned'). A very similar distribution is obtained from a simulation of 3 years' observations in which a random 50% of the nights are skipped (Fig. 1.3, bottom). It is evident from Fig. 1.3 that a number of clusters do not get observed for 3 weeks or more, but this is to be expected when random weather patterns, the moon, scheduled followup, and candidate object re-observations, etc. are considered. We have recently introduced other measures which we expect will decrease the large number (though still $< 10\%$) of observations for which $\Delta t = 3$ days. Still, 80% of the observations were made with $\Delta t \leq 21$ days, and although sparser clusters do slip through the cracks more easily, as Fig. 1.3 demonstrates, the amount of favor given to larger clusters is small.

The overall results are more than adequate, and we believe the scheduling could not be substantially improved by a human counterpart.

1.5 Searching for Supernovae

The software which searches the images for supernovae consists of a series of IRAF tasks and programs written in C, linked together and automated via a set of scripts written in PERL, with final cuts on potential discoveries being made interactively. Briefly, it involves subtracting an earlier observation of the field (a *template*) from the observation so that all objects which have increased in flux appear as new point-sources. No attempt is made to combine the 8 amplifier images for each color into one 4096×4096 image prior to searching; instead each amplifier is processed individually. This has several advantages and one disadvantage, which will be pointed out below. Figure 1.4 illustrates the method, which can be summarized by the following expression:

$$\mathcal{S} = b \times (a + \mathcal{O} * \mathcal{K}) - \mathcal{T}, \tag{1.2}$$

where the subtracted image, $\mathcal{S}$, is scanned for new objects. Here, $\mathcal{T}$ is the template of the field, $\mathcal{O}$ is the observation (registered to the template), $\mathcal{K}$ is a convolution kernel required to match the PSF of $\mathcal{O}$ with that of $\mathcal{T}$, and a and b are an additive constant and linear scale factor, respectively, which match the background and flux of objects in $\mathcal{O}$ to those in $\mathcal{T}$. The following sections describe the algorithm in detail.

1.5.1 Constructing the Template

Before any image subtraction can be done, a template of the field must be constructed. This involves (1) preprocessing – masking of saturated stars and bright pixels and removing any linear gradients in sky brightness (all observations are preprocessed identically); (2) detecting bright stars for image alignment (we use DoPhot, Schechter, Mateo, & Saha 1993, which also provides an analytic model of the stellar

PSF); (3) identifying isolated high S/N stars of differing brightness for use in PSF and flux matching, and (4) laying down a grid of (negative) false stars of known flux for quick assessment of searching depth after the template is subtracted from the observation. The template is made using an observation obtained preferably during a dark, transparent night with good seeing. If a later observation proves to be better than the template, the template is replaced after that observation has been searched. This is a simple procedure since the process is completely automated. A section of an example template is shown in Figure 1.4a.

1.5.2 Image Registration

The most important aspect of the image subtraction process is accurately aligning the observation images to the template images. The registration is accomplished using a triangle-matching algorithm (see Groth 1986) to determine the coordinate transform between bright stars found using DoPhot in the two images. In our case since the template and observations are always taken on the same telescope/camera system, we can constrain the rotation and scale in the transform, which allows a more robust convergence with fewer failures. The transform is then entered into the IRAF GEOTRAN routine which performs the flux-conserving linear geometric transform of the observation image, using a linear interpolation between pixels for subsampling. Since the PSF is well sampled, resampling errors are small. The registration typically requires a shift of < 50 pixels and is accurate to ~ 0.3 pixels across an entire individual amplifier image. This process is aided by not registering the entire $45'$ field at once; the effects of variations in pixel scale across the field are reduced and higher-order transformations rendered unnecessary. However, it does result in a loss of ~ 50 pixels of searchable area near the edges of each amplifier image after the registration. In Figure 1.4b we present a portion of an observation before (left) and after (right) it is registered with the template of Figure 1.4a.

1.5.3 PSF Matching

If the observation and template were both photometric and their PSFs were identical, a simple subtraction would now be suitable. Unfortunately, this is almost never the case. Instead, we must match the images' PSFs and intensities. For the sake of simplicity, we will assume that we are convolving the template, since the template is usually the better image, and the better of the two images is the one which must be degraded to match the poorer one. The convolution kernel which can be used to convolve the template so that its PSF matches that of the registered observation is computed using Andrew Phillips' implementation of the algorithm of Ciardullo, Tamblyn, & Phillips 1990 (see Phillips & Davis 1995) in IRAF (called QPSF, in the ALINEAR package). Briefly, the method computes the kernel in Fourier space, where a convolution is a simple multiplication. Since the PSF is very nearly Gaussian, its Fourier Transform (FT), and thus the convolution kernel, will also be very nearly Gaussian. However the high-frequency components of the FT become dominated by noise in the wings of the PSF where the signal becomes weakest. Still, one can model the high S/N components of the FT with an elliptical Gaussian, and the wings of such a model can be used in place of the noise-dominated components. Thus a single, bright, isolated star can be used to compute the required convolution kernel. In the case where the two images are similar (FWHMs differ by < 0.3 pixels), the convolution kernel may be very poorly resolved, or even undefined (as might be the case if the PSFs are elongated). One can overcome this problem by degrading the slightly poorer image using a Gaussian convolution kernel before performing the PSF matching. The Fourier method is applied to each of the individual amplifier images, sufficiently reducing the effects of any small-scale PSF variation across the focal plane. The template of Figure 1.4a is shown in Figure 1.4d after it has been convolved to match the registered image of Figure 1.4c.

1.5.4 Photometric Scaling and Subtraction

For the photometric scaling, as in the PSF matching, all that is required is a high S/N, isolated star or galaxy. The IRAF ALINEAR task, ITRAN (Phillips & Davis 1995), performs a linear least-χ^2 fit to the difference, in ADU, between the pixels which surround the chosen bright object in a subsection of the two images (registered observation and convolved template). The resulting slope (measuring the ratio in flux between the two images) and offset (measuring the difference in sky brightness) can then be applied to the registered observation. The slope, offset, and χ^2 give us further information on the quality of the observation and subsequent subtraction. For example, the star chosen for PSF-matching might be saturated in the observation, say, if the seeing was extremely good, and the χ^2 will be extremely high. In this case we can go back and match the PSFs and fluxes using a slightly fainter star and check the results. Again it is worth noting that having the focal plane divided into eight smaller images makes the scaling more accurate as any large-scale nonlinear gradients in sky brightness or scattered light (such as due to the moon) or even variation in transparency across the $45'$ field (due to thin clouds) are reduced. It makes even more sense when one considers that the individual images come from different CCDs and thus have different gains, bias levels, and color terms.

Finally, the intensity-transformed, convolved template now reflects the same atmospheric and photometric conditions as the registered observation, and a simple subtraction of the first from the second can be performed. The subtraction of the convolved template image (Figure 1.4d), after being photometrically scaled, from the registered observation (Figure 1.4c) is presented in Figure 1.4e. Here, a supernova is clearly visible where in the original observation (Figure 1.4b), it was hidden in the background light of its host galaxy. Five of the (now positive) sensitivity stars are also visible in the subtracted image. The corresponding magnitude limit for this image is $R_M \simeq 20.5$ (typical); the supernova is ~ 0.9 magnitudes brighter.

Note that the noise in the subtracted image is now a function of Poisson noise (from the shifted observation) plus correlated Poisson noise (from the convolved template) plus residual noise left over from the subtraction.

1.5.5 Object Detection

Once the subtraction is complete, a new supernova will appear as a point source in the subtracted image, with a FWHM which is the same size as other stars in the original observation. To find these, we use a point-source detection algorithm, written in C, which samples the subtracted image at many locations over the scale of the PSF to estimate the total noise (σ) within one correlation length. It then detects objects with a total flux that is 3 σ above the background. If a detection lies at the same location as a bright star on the template, it is assumed to be a poor subtraction, and is eliminated from the list. (Poor subtractions near bright stars are common because the large flux gradients magnify the effects of even a small registration or PSF-matching error; such a residual can be seen above and to the left of the supernova in Fig. 1.4e.) In addition, our routine tests if each detected object is consistent with a point source of given peak intensity and known FWHM. This helps eliminate cosmic rays, which resemble stars (since they have been convolved) but are slightly narrower than true stars in the image. Often a poor subtraction results in an area of negative flux next to a detected object. Our algorithm tests for these as well and eliminates any such suspicious objects. The routine then eliminates groups of objects which fall in straight lines (satellite trails or bad columns). As a check on the depth and robustness of the search, the false sensitivity stars which have been detected are identified, and the corresponding limiting magnitude is computed from the known flux of the faintest star detected.

Though the object-detection algorithm has been custom designed to reduce the number of false detections, several hundred usually pass the cuts for each observation. Most of these offenders are cosmic rays; thus, our ultimate defense is that we

have two observations made simultaneously, one in V_M and one in R_M. As a final check, the locations and fluxes of the objects detected in the V_M images are compared to those in the R_M images. This serves to cull nearly all cosmic ray hits. In the end, our detections are $\sim$4.5 σ above the correlated noise (recall this is *not* the Poisson noise of the original image, but can be similar to it in a good subtraction, or significantly greater than it in a poor subtraction). On average 5–15 objects per observation remain, and these comprise poor subtractions near bright galaxies and stars (somewhat common, particularly in poor seeing); cosmic rays which coincidentally lie at the same locations in both color images (rare); and true astronomical objects ($>$ 95% of which are asteroids). For each of these objects, a subraster image is created, and final cuts are made by eye.

1.5.6 Subrasters and Object Classification

The layout of a subraster image produced by the search software is shown in Figure 1.5, in this case, containing the SN seen in Figure 1.4e. The subrasters allow for quick examination, by including the candidate object in both colors (V_M on the left, R_M on the right), in the template (bottom), observation (top) and subtraction (center). They are archived on disk for quick retrieval and can be accessed at any time by running a script which displays the subrasters, and allows interesting objects to be scrutinized in detail using IMEXAM in a local XIMTOOL window. Alternatively, they can be viewed over the World Wide Web on an interactive web page which displays and then IMEXAMs them in a local XIMTOOL window, and allows object classifications to be recorded in a database for comparison to future observations (see below). Both methods also display the object's coordinates and approximate magnitudes in both colors. In addition, information on the quality of the observation, such as the scale and offset used in flux-matching, the FWHM, and the number of sensitivity stars detected, are all reported to the classifier. All of these data are used to quickly classify objects among poor subtractions and cosmic rays,

asteroids, variable stars which have increased in brightness, and supernova candidates. We find that the human eye is extremely efficient at classifying the objects. A great deal of experience is gained by examining subrasters day after day, and a certain amount of intuition certainly plays a role in object classification; however certain concrete rules also apply.

SNe, variable stars, and asteroids each have characteristics which aid in their identification, and the color information which we have is extremely helpful. Young supernovae are bluish objects ($V_M - R_M < 0.2$), and are usually associated with a galaxy. If an object lies directly on the nucleus of the galaxy, it is treated with suspicion and is often a poor subtraction or AGN; however we have detected several SNe very near the centers of their host galaxies, SN 1997bz being one example. Asteroids, on the other hand, are usually redder than the color of the Sun ($V_M - R_M > 0.3$), are usually not associated with a galaxy, and upon close inspection often exhibit slightly elongated PSFs (particularly the bright ones). Unfortunately there is a large dispersion (~ 0.5 magnitudes) in the rough uncalibrated $V_M - R_M$ colors computed by the software, thus color discrimination provides an aid but not an end in object classification. Variable stars are straightforward to identify as they are present as a star on the template image, as well as in the observation.

The classification-by-eye scheme is certainly not fail-proof (it is possible that we do misidentify some SNe as asteroids). We overcome this weakness by keeping records of the positions of all objects which we identify. If an object is identified as an asteroid, we can compare its location to those of other objects identified in a later observation of the same field. If it is present at the same location in both observations, it is likely to be a SN rather than an asteroid. On the other hand, any field with a probable supernova as identified by eye is re-observed as soon as possible to see if the object has moved or disappeared; if it has, it is most likely an asteroid. We perform such followup on all objects located near galaxies, regardless of color, and on blue objects not associated with galaxies. In the end, this conservative approach

eliminates all possibility of misidentifying an asteroid as a supernova. Our probability of misidentifying a supernova as an asteroid is not zero, but if we re-observe the field within the next few weeks, we are able to correct such misidentifications. However we still have a diminished sensitivity to SNe with undetected hosts.

1.6 Results

Once a promising supernova candidate is found, and has also been confirmed with a second observation, it is announced in an IAU Circular. A finder chart with positions accurate to better than $0.5''$ is immediately created using an automated routine, and all available information is placed on our web page. Information on the 52 supernovae discovered by this search to date are listed in Table 1.6 (we came on line in early June, 1996). The rate of discovery has been about 1.5 month^{-1}. Of the SNe for which redshifts have been measured, $\sim$1/2 appear to be associated with their host Abell cluster, while three are in foreground galaxies, and the remainder ($\sim$1/2) lie behind their target clusters. $\sim$2/3 of the SNe which have been spectrally classified are SNe Ia. Many of the other SNe have occurred in elliptical galaxies and can be identified as type Ia on that basis alone. We can also, with reasonable reliability, classify SNe using their multicolor light curves. In total, we find that $\sim$2/3 of the objects which have spectra and/or reduced light curves so far, are SNe $\sim$Ia, and $\sim$1/2 of these are associated with their host Abell clusters. Two classified SNe are type II and are associated with their host clusters, while one other, classified as type II, is not. Light curves, classification, and analysis will be presented in an upcoming paper (Reiss *et al.* 1999a).

We keep records of the limiting magnitudes resulting from each observation. The distribution for observations over the first year are shown in Figure 1.6. The median limiting search magnitudes are $\sim$ 20.4 in R_M and $\sim$ 20.5 in V_M, The large dispersion can be attributed to variation in sky conditions. A more complete discussion of our

magnitude limits and their effects on the completeness of our search, as well as implications for the SN rate, are presented in Chapter 3.

1.7 Determining the Motion of the Local Group

In this section we address how well we expect to be able to determine the motion of the Local Group (LG) relative to the Abell Clusters in our sample using SNe Ia. To do this, we have run a series of Monte Carlo simulations in which 10,000 fake samples have been created. The samples have varying sizes, geometries (in the sky), and bulk motion vectors. For the following discussion, all velocities mentioned are relative to the LG frame. In each case, the 'fake' supernovae have been given typical peculiar velocities of 400 km sec^{-1} (Marzke *et al.* 1995) on top of the flow velocity, distance uncertainties of 8%, and redshift uncertainties of 0.001 (in this redshift range, the overall errors are dominated by the distance uncertainties). The peculiar velocities which we are to use for our measurement are likely to be smaller ($\sim$ 250 km sec^{-1}) because we can use the average peculiar velocities of several galaxies in the host clusters for many of our SNe; however, note that we only include uncorrelated motions, and neglect small-scale correlated motions described in Watkins & Feldman 1995, which Abell clusters are less sensitive to than galaxies in the field. Still, the uncertainties are dominated by the distance uncertainties (a distance uncertainty of 8% at z=0.08 is a $\sim$ 1900 km sec^{-1} velocity uncertainty), so these simulations do not present unrealistic errors (this was verified by running simulations using different uncertainties and peculiar velocities). The redshift distribution of the SNe in the simulations mimics that of our cluster sample. Once the simulated SN sample is created, the best-fit values for the Local Group velocity vector, $\vec{v}_{LG}$, and the Hubble Constant, H_0, for this sample are determined simultaneously by minimizing the statistic

$$\chi^2 = \sum_i \frac{\left(cz_i - H_0 d_i + \vec{v}_{LG} \cdot \hat{r}_i\right)^2}{\sigma_i^2}, \tag{1.3}$$

where d_i is the distance of the ith supernova, z_i is its redshift, $\hat{r}_i$ is the unit vector pointing in its direction in the sky, and σ_i^2 is the quadrature sum of all errors mentioned above.

Of primary interest is estimating the accuracy with which our sample can be used to measure the reflex motion of the LG. To answer this, we compute the 1-σ dispersions in the 10,000 simulated dipole measurements for a sample geometry which matches that of our cluster targets. These are presented in Table 1.7 for the 3 velocity components, for a 20-, 40-, and 60-SN sample, using the parameters described above. The dispersions are identical for all sample geometries which we explored, and are independent of the direction of the input velocity vector. By blindly comparing these uncertainties to those quoted by LP in their 1994 measurement, ($\pm$250, $\pm$273, $\pm$198) km sec^{-1}, we find that applying $\sim$35 SNe Ia distances collected in our sample to the problem results in a comparable measurement to that made using the 124 BCG distances of the LP sample. This is not surprising noting that SNe Ia are $\sim$ 2$\times$ more accurate as distance indicators. For example, were we to make a velocity measurement, using the SNe Ia in our sample, that is consistent with the LP result, it would be significant at 2.3 σ, 3.7 σ, and 4.9 σ levels for 20, 40 and 60 SNe Ia, respectively, compared to the COBE measurement. On the other hand, a measurement which coincides with the COBE dipole would rule out the LP result at the 1.9 σ, 2.6 σ, and 2.9 σ levels (using the uncertainties of LP94). Note, however, that the simulated distance uncertainties of 8% are slightly greater than that estimated by Riess, Press, & Kirshner 1996 for their well-sampled SNe Ia light curves; this along with the high velocity dispersions used in the simulations, as pointed out above, implies that the results described here are probably slightly conservative. A comparison of the uncertainties listed in Table 1.7 for 20 SNe with those quoted by RPK95 (for 13 SNe) of ($\pm$370, $\pm$510, $\pm$220) confirms this notion.

In addition to estimating the expected uncertainties, the simulations also allow us to confirm that there will be a small geometric bias in any dipole measurement

which is made using our sample, due to its non-uniform geometry (see Fig. 1.1). By comparing the fits resulting from the simulated samples to their input dipole velocity vectors, we find that there will likely be a $\sim \pm 5$ km sec^{-1} offset in each vector component from the true value. The value will of course depend upon the actual geometry of the sample and the measured bulk motion, and can be easily computed and corrected, but it is still reassuring to find that it will be small compared to the expected uncertainties. We will investigate this, and other possible sources of systematic error, in a subsequent paper on the distance measurements from our first year's set of SNe.

Table 1.1: List of target clusters in the Mount Stromlo Abell Cluster Supernova Search. Table continues on next page.

	J2000			
Abell	α	δ	z	N_{gal}
119	0 56.35	-1 15.78	0.044	69
151	1 8.87	-15 25.02	0.053	72
168	1 15.16	0 13.85	0.045	89
279	1 56.37	1 3.65	0.080	70
401	2 58.95	13 34.93	0.074	90
423	3 11.29	-12 6.72	0.080	89
514	4 47.67	-20 26.73	0.078	78
5481	5 45.17	-25 52.00	0.042	80
5482	5 48.67	-25 27.00	0.042	80
754	9 8.83	-9 39.20	0.054	92
1020	10 27.84	10 24.67	0.065	68
1066	10 39.40	5 10.35	0.070	68
1317	11 35.13	-13 31.60	0.072	82
1644	12 57.24	-17 22.22	0.048	92
1648	12 59.00	-26 38.18	0.070	68
1736	13 26.87	-27 7.55	0.046	104
1773	13 42.14	2 14.88	0.078	66
1780	13 44.64	2 52.97	0.079	71
1809	13 53.31	5 10.25	0.079	78
2029	15 10.98	5 45.70	0.077	82
2362	21 40.73	-14 16.35	0.061	69
2401	21 58.87	-20 6.63	0.057	66
2480	22 46.08	-17 41.18	0.072	108
2559	23 13.12	-13 41.67	0.080	73
2661	23 46.67	-10 25.33	0.064	147
2670	23 54.17	-10 24.30	0.076	142
2819	0 45.82	-63 35.62	0.075	90
2889	1 14.76	-48 30.15	0.067	65
2954	1 54.47	-71 28.32	0.057	121
2995	2 15.18	-24 50.07	0.038	69
3094	3 11.44	-26 55.73	0.068	80
3108	3 15.24	-47 37.95	0.062	73
3112	3 17.94	-44 14.10	0.075	116
3122	3 22.30	-41 20.33	0.064	100
3128	3 30.21	-52 33.80	0.060	140
3135	3 34.04	-39 0.02	0.063	111
3142	3 36.71	-39 48.17	0.066	78
3158	3 43.01	-53 38.57	0.059	85
3188	3 57.77	-27 2.45	0.076	67
3202	4 0.25	-53 39.62	0.069	65
3223	4 8.57	-30 49.13	0.060	100
3231	4 11.87	-64 36.40	0.057	65
3266	4 31.16	-61 28.67	0.059	91
3301	5 0.80	-38 40.67	0.054	172
3341	5 25.59	-31 35.43	0.038	87
3381	6 9.92	-33 35.65	0.038	69
3392	6 27.07	-35 28.90	0.055	77

Table 1.2: List of target clusters in the Mount Stromlo Abell Cluster Supernova Search (continued from previous page).

	J2000			
Abell	α	δ	z	N_{gal}
3490	11 45.31	-34 26.67	0.069	91
3528	12 54.30	-29 1.27	0.053	70
3549	13 14.36	-29 26.87	0.075	65
3558	13 27.91	-31 29.53	0.048	226
3559	13 29.90	-29 31.47	0.046	141
3560	13 31.84	-33 13.42	0.013	184
3562	13 33.53	-31 40.37	0.050	129
3566	13 38.99	-35 33.22	0.050	100
3571	13 47.48	-32 51.95	0.040	126
3577	13 54.34	-27 50.72	0.050	103
3651	19 52.18	-55 5.27	0.060	75
3667	20 12.50	-56 49.00	0.056	85
3698	20 35.98	-25 16.57	0.020	71
3716	20 51.55	-52 42.73	0.046	66
3744	21 7.23	-25 28.90	0.038	70
3775	21 31.60	-43 18.75	0.080	76
3781	21 34.63	-66 50.63	0.057	79
3806	21 46.63	-57 17.12	0.076	115
3809	21 46.96	-43 54.10	0.062	73
3822	21 54.10	-57 50.82	0.076	113
3825	21 58.37	-60 23.67	0.075	77
3831	22 3.33	-45 49.47	0.065	81
3879	22 27.83	-69 1.68	0.067	114
3990	23 18.77	-67 46.58	0.029	98
4008	23 30.29	-39 19.45	0.055	66
4038	23 47.70	-28 8.33	0.029	117
4059	23 56.68	-34 40.30	0.049	66

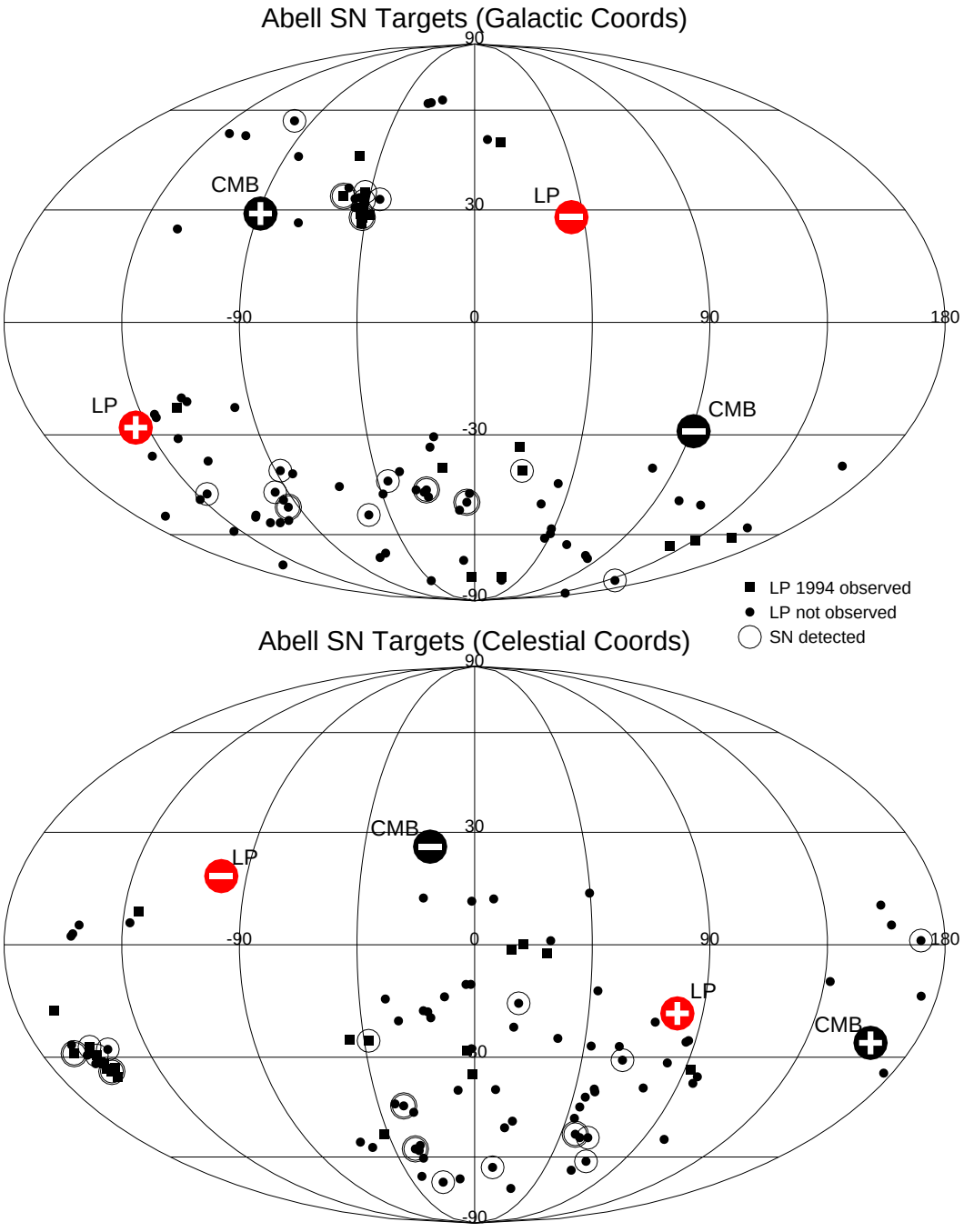

Figure 1.1: The distribution of target clusters in the sky. Galactic (top) and equatorial (bottom) coordinates are shown. Filled square symbols represent clusters whose BCG distances were measured by LP94, filled circles were not. Thin circles enclose those clusters in which this project has found a supernova since June 1996 (several have two SNe). Also shown are the direction of the LP94 bulk flow (LP), and the direction of the Fixsen *et al.* 1994 microwave background dipole (CMB).

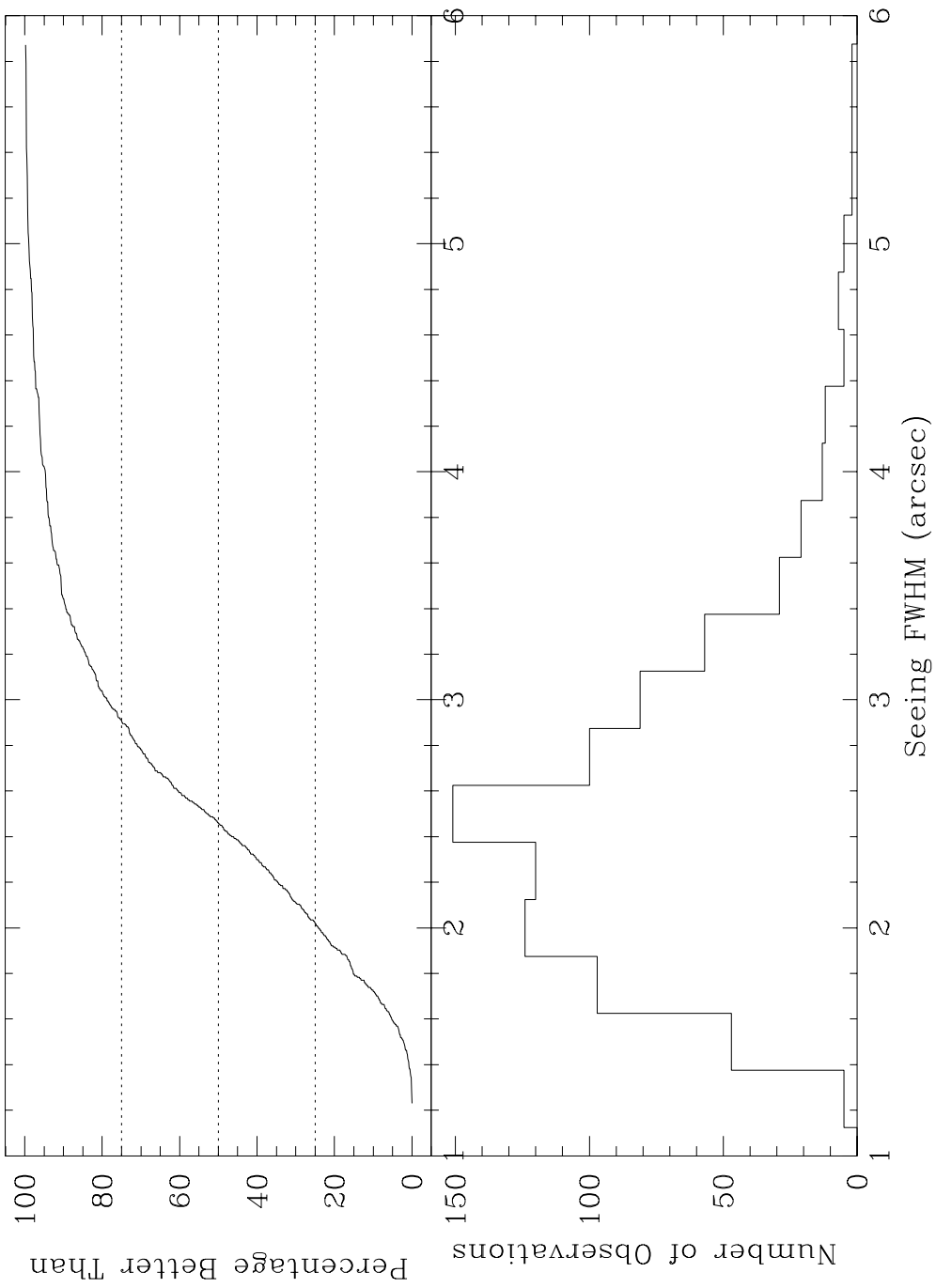

Figure 1.2: The distribution in seeing FWHM on the 1.3m telescope at Mt. Stromlo over a year. Median seeing is $\sim 2.5''$.

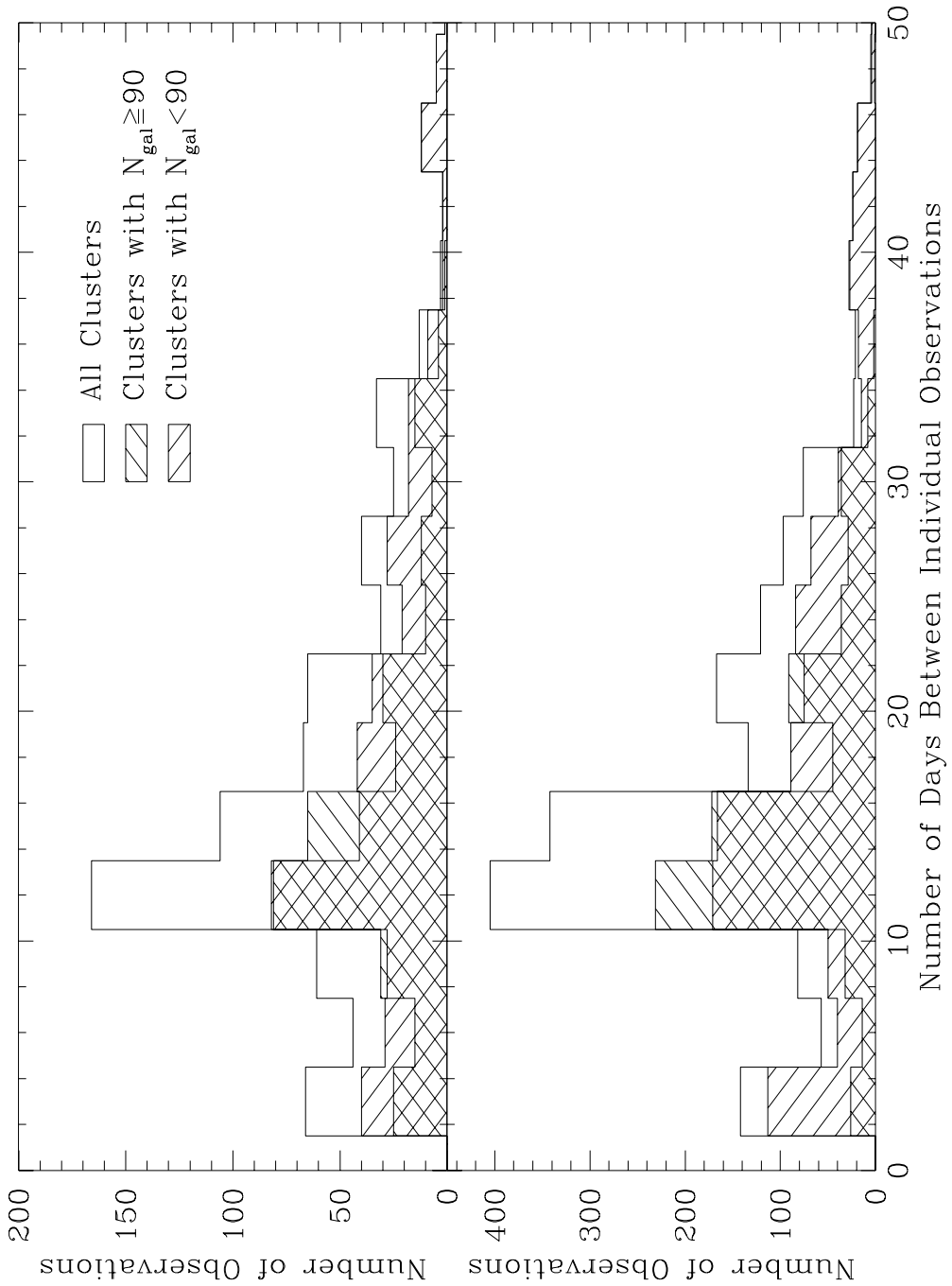

Figure 1.3: A histogram of the number of days between each cluster observation (Δt). Top: The observations of June 1996 to the present; Bottom: A simulation of observations for a 3-year period.

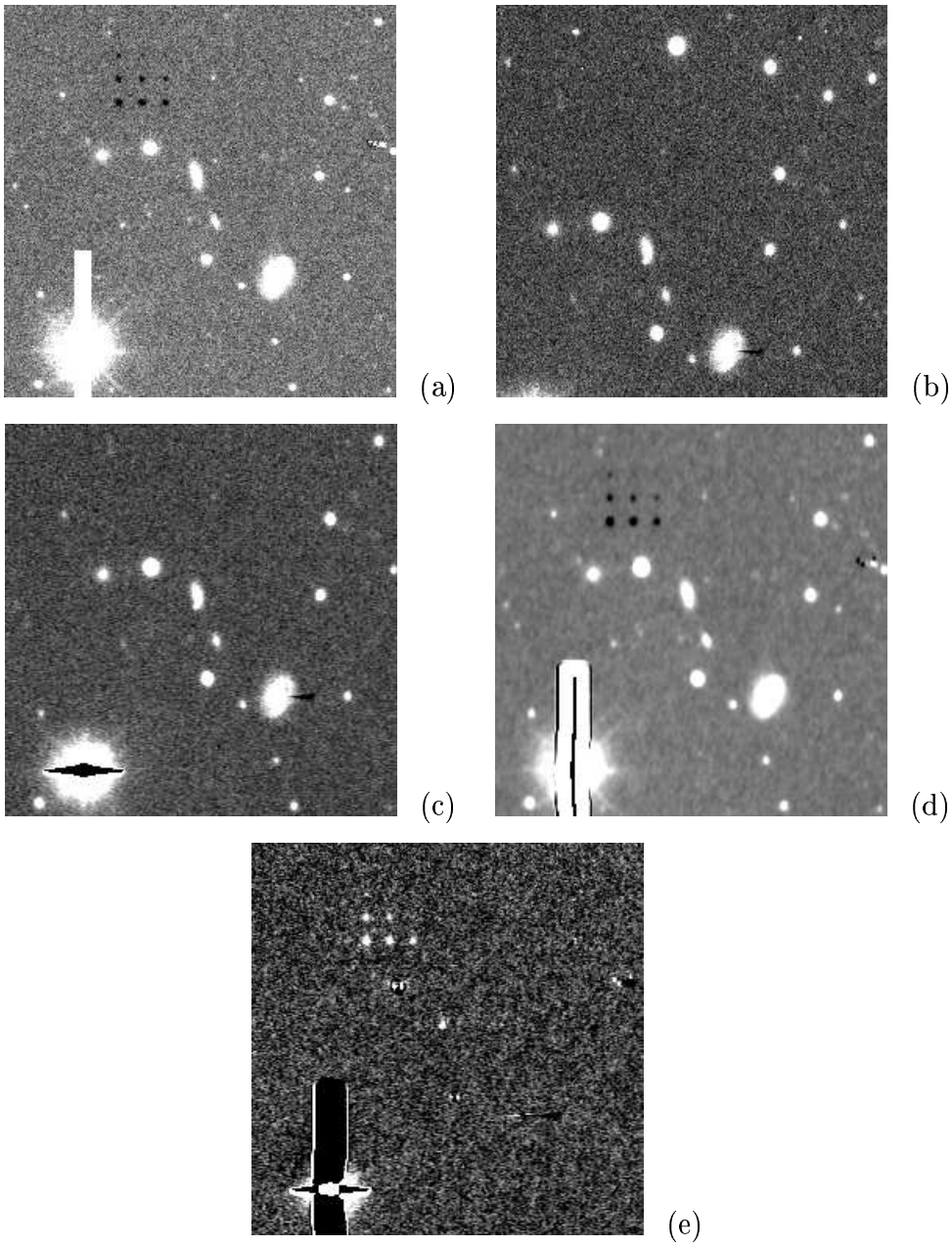

Figure 1.4: The search process illustrated on a subsection of the images in which SN 1996aj in Abell 3559 was detected. Fig. (a) shows a template, with a grid of 9 false sensitivity stars and masked saturated regions. The observation (b) is registered to the template (c). Fig. (d) shows the template of Fig. (a) after it has been convolved so that its PSF matches that of the registered image (c). After the registered image has been flux-matched to the convolved template, the template is subtracted. The residual is shown in Fig. (e), with the supernova (center) and five sensitivity stars clearly visible.

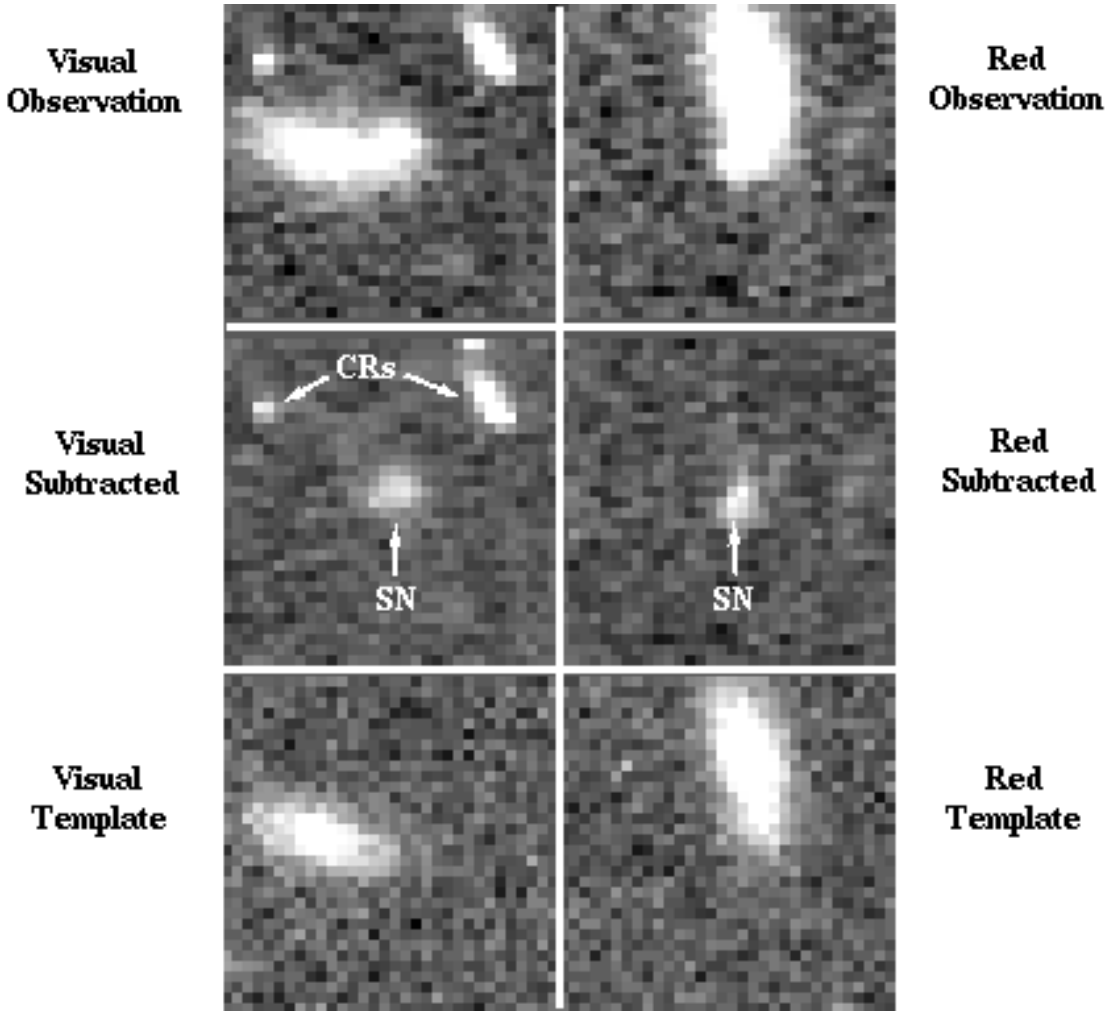

Figure 1.5: Subraster of a SN candidate, produced by the search software.

This is the actual subraster created for SN 1996aj seen in Fig. 1.4e. The supernova is clearly visible in both colors (SN), as are two cosmic rays (CRs, convolved during the subtraction process) in the V observation and subtraction.

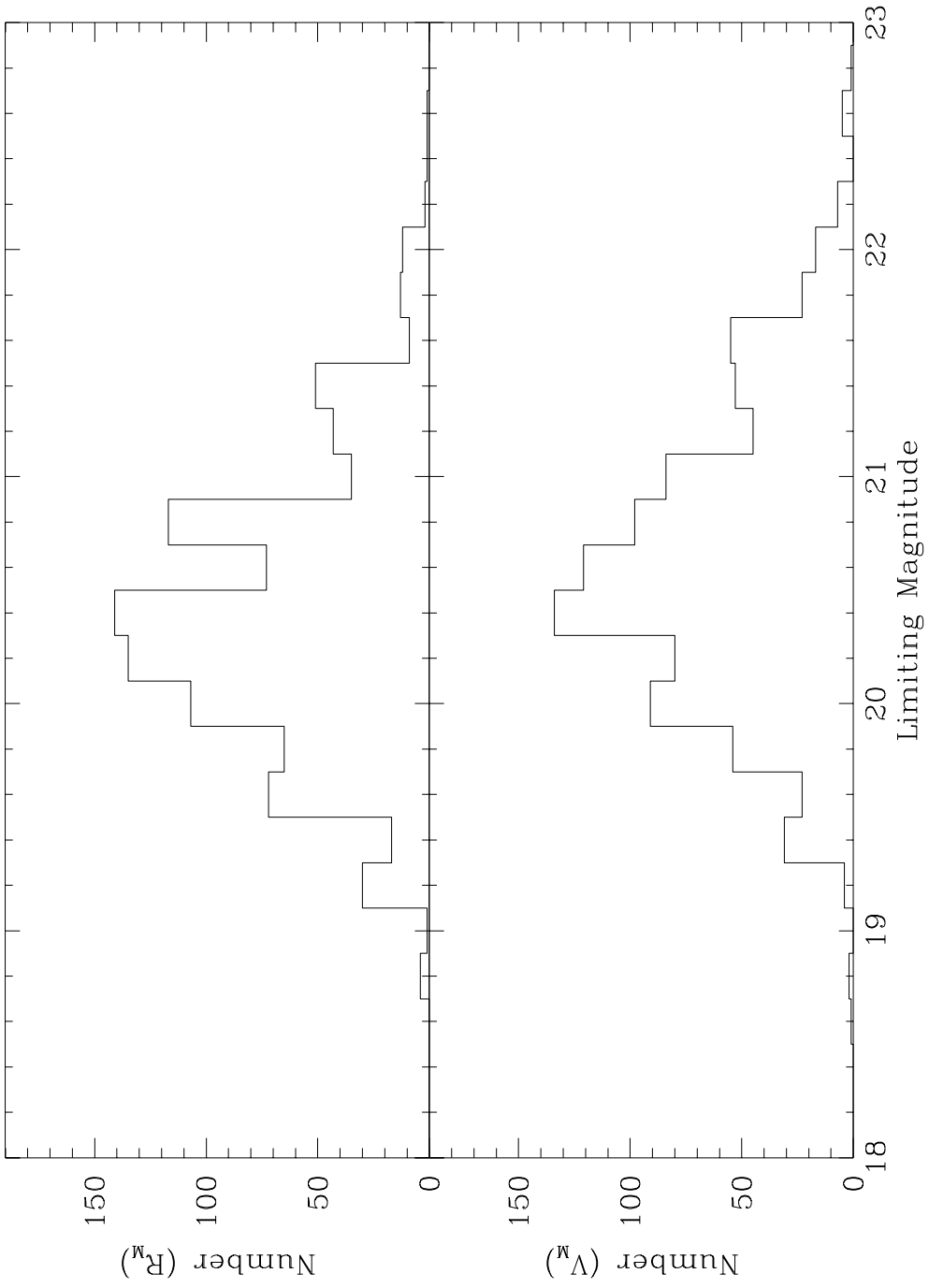

Figure 1.6: Distribution of limiting magnitudes in the MSACSS, for all observations for which this was measurable. Typical median limits have been ~ 20.4 in R_M and ~ 20.5 in V_M.

Table 1.3: Supernovae discovered in the MSACSS

SN	Date Found	Not Present	Abell	Type	z	Cluster z
1996af	12 Jun 96	16 May	3879	Ia	0.100	0.067
1996ag	12 Jun 96	22 May	3809	Ia?	0.140	0.062
1996aj	15 Jun 96	28 May	3559	Ia	0.110	0.046
1996am	12 Jul 96	3 Jul	3809	Ia	0.065	0.062
1996ao	2 Aug 96	24 Jun	3128	Ia	0.058	0.060
1996ap	11 Aug 96	2 Aug	3806	?	0.075	0.076
1996bm	4 Oct 96	1 Sep	2819	II?	0.164	0.075
1996bx	18 Nov 96	23 Aug	3202	Ia	0.058	0.069
1997Q	27 Jan 98	19 Jul	3562	II-P?	0.040	0.050
1997by	27 Apr 97	4 Apr	1736	Ia	0.045	0.046
1997bz	27 Apr 97	11 Apr	1238	Ia	0.030	0.072
1997cl	2 May 97	5 Aug	3577	II-n	0.047	0.050
1997cm	2 May 97	15 Mar	3528	II?	0.071	0.053
1997cp	2 Jun 97	11 May	3806	Ia?	0.160	0.076
1997cr	2 Jun 97	17 Aug	3744	II	0.077	0.038
1997cu	4 Jul 97	25 Feb	3128	Ia	0.062	0.060
1997cv	7 Jul 97	10 Jun	3565	II?	0.024	0.012
1997cy	16 Jul 97	12 Mar	3266	II-pec	0.063	0.059
1997cz	19 Jul 97	26 Apr	3565	II?	0.048	0.012
1997df	8 Sep 97	27 Aug	3223	II?	0.059	0.060
1997dr	7 Nov 97	17 Oct	3112	Ia?	0.075	0.075
1997fb	31 Dec 97	19 Dec	3301	Ia	0.053	0.054
1997fc	31 Dec 97	19 Dec	3301	Ia	0.054	0.054
1997fd	28 Dec 97	12 Dec	3158	?	0.190	0.059
1997fe	31 Dec 97	7 Nov	3266	Ia?	0.059	0.059
1998O	27 Jan 98	19 Jul	3566	II?	0.049	0.050
1998P	27 Jan 98	19 Jul	3566	II?	0.097	0.050
1998Z	16 Mar 98	18 Feb	3341	Ia	0.038	0.038
1998bq	18 Apr 98	10 Mar	2029	II?	0.095	0.077
1998br	28 Apr 98	18 Apr	2029	Ia?	0.081	0.077
1998bs	18 Apr 98	10 Mar	3558	?	??	0.048
1998bt	10 Mar 98	27 Jan	1736	II?	??	0.046
1998ch	18 May 98	30 Apr	3559	II	0.047	0.046
1998cm	10 Jun 98	18 May	1780	Ia	0.080	0.079
1998cq	17 Jun 98	19 Dec	2819	Ia	0.150	0.075
1998do	1 Aug 98	4 Dec	168	?	0.092	0.045
1998dp	14 Aug 98	8 Jun	2401	?	0.057	0.057
1998du	14 Aug 98	1 Aug	2819	?	0.076	0.075
1998dv	22 Aug 98	1 Aug	3266	?	0.155	0.059
1998dw	28 Aug 98	22 Dec	151	Ia	0.049	0.053
1998dy	14 Jul 98	13 Apr	3266	?	??	0.059
1998dz	3 Sep 98	22 Aug	3122	Ia	0.091	0.064
1998ea	6 Sep 98	31 Aug	3266	Ia	0.057	0.059
1998el	22 Oct 98	3 Oct	3122	?	0.10	0.064
1998ez	8 Dec 98	24 Oct	3188	?	0.072	0.076
1998fb	20 Dec 98	29 Nov	3128	?	??	0.060

Table 1.4: Expected uncertainties in the measurement of the three components of the reflex motion of the Local Group in a sample of SNe Ia of size N_{SN}.

	km s^{-1}		
N_{SN}	σ_x	σ_y	σ_z
20	545	545	300
40	325	325	185
60	245	250	140

Chapter 2

THE RATE OF SUPERNOVAE IN NEARBY FIELD GALAXIES FROM THE MOUNT STROMLO ABELL CLUSTER SUPERNOVA SEARCH

2.1 Introduction

The nearby rate of supernovae (SNe) is an important number in many areas of astrophysics. The structure, chemical enrichment, and dynamics of the interstellar medium are directly related to SN rates (van den Bergh & Tammann 1991 and references therein). Since they mark the end-points of the evolution of many types of objects from massive stars to white dwarfs (see Cappellaro *et al.* 1993a for references), SN rates additionally place important constraints on star formation and stellar evolution theories, through a comparison of rates among different stellar populations.

The primary source for SN rate estimates during the past decade has come from the Asiago and Crimean photographic search program (Cappellaro *et al.* 1993a, Cappellaro *et al.* 1993b), the visual search of Rev. Evans (van den Bergh, McClure, & Evans 1987, Cappellaro *et al.* 1997), and the photographic Calán/Tololo (Cappellaro *et al.* 1997, Hamuy & Pinto 1999) searches. Not until recently has the analysis of systematics in such searches reached a level so that they all result in consistent derivations of SN frequencies. However, all have required large and complicated efficiency corrections due to the nature of the searches. This will change now that wide-field CCD-based searches will enable unbiased searches through image-subtraction (Reiss *et al.* 1998 [Chapter 1]). Here we discuss the first results from such a search

with a large enough detection rate at low-redshift to allow a determination of the SN rate in nearby field galaxies.

During the 30 months of the Mount Stromlo Abell Cluster Supernova Search (MSACSS), between June 1996 and December 1998, a total of 92 rich Abell clusters were each observed an average of $\sim$ 27 times, for a total of 2540 observations. Some 46 supernovae were detected prior to the end of 1998 (and two were found in Jan. 1999, but will not be included in the statistics of this paper), and as listed in Table 1.6, nearly all of these (42) have measured redshifts by now, and most (35) have been at least tentatively classified. Of those for which redshifts have been measured, nearly half (20) appear to lie in field galaxies, projected either in front of (3) or behind (17) the target clusters. In this chapter , we describe the procedure by which we determine the SN rates for the roughly one-half of detected SNe which occurred in galaxies that were *not* members of the targeted clusters.

Because any measured frequency of supernovae is naturally expected to be proportional to the number of stars surveyed (at least to first order), SN rates are commonly reported in "supernova units," (SNu; van den Bergh & Tammann 1991):

$$1\,\mathrm{SNu} \equiv \frac{1\,\mathrm{SN}}{\mathrm{Century} \times 10^{10} L_{B_\odot}}, \tag{2.1}$$

where $L_{B_\odot}$ refers to the total integrated blue luminosity of stars, in solar units, within which a SN could have been detected by the SN survey in question; this is referred to as the "control luminosity". By its very nature, a measurement in SNu is strongly dependent on the age of the underlying stellar population; as galaxies evolve their blue luminosities decrease, even though the total number of stars does not change significantly. This measure should therefore be used with caution when comparing measured SN rates between different galaxy samples. For this reason, we will also report the field and cluster SN rates in SNu_R, *i.e.* per $10^{10} L_{R_\odot}$, as well as in SNu, allowing a better disentanglement of the effect of the host galaxy environment

on the SN rates from the (better understood) effects of the galaxy samples' stellar populations (Cappellaro, Evans, & Turatto 1999).

We will describe the sample of field supernovae in detail §2.2. We then discuss our technique for determining accurate limiting magnitudes for each search observation in §2.3. In section 2.4 we will describe our method for computing control times for each field, and in section 2.5, we determine the "control luminosity," or the integrated luminosities of the galaxies to which the search has been sensitive. Section 2.6 summarizes the integration of the control times and the method of combining these with the galaxy control luminosity to derive the supernova rates. Finally we will analyze the uncertainties and possible sources of systematic error in the derived SN rates in section 2.7, and discuss these results with respect to other measurements of local supernova rates in section 2.8.

2.2 The Sample of Field Supernovae

To select field SNe, we impose the constraint,

$$|cz_{\rm SN} - cz_{\rm cluster}| > 2\overline{\sigma}_v, \tag{2.2}$$

where we used $\overline{\sigma}_v = 800$ km sec^{-1} for the typical velocity dispersion of these rich clusters. As it happens, all of the 20 SNe that obey expression 2.2 also have recession velocities that differ by > 3000 km sec^{-1} from the clusters in their fields. Meanwhile, only three additional clusters are added to the field SN sample when the velocity delimiter is decreased to $\overline{\sigma}_v = 600$ km sec^{-1}, suggesting that while this criterion for selection of a field SN seems arbitrary, it serves as a simple and reasonable criterion. Figure 2.1 supports this notion clearly with a comparison of the cluster redshifts ($z_{\rm cluster}$) to the SN redshifts ($z_{\rm SN}$) for all of the MSACSS SNe for which redshifts have been measured; cluster SNe (open symbols) stand out clearly agains the scattered points marking the field SNe that will be considered in this chapter .

Table 2.1 lists the 20 field SNe which will be considered for the calculation of the field SN rate in this chapter . In addition to these, four SNe to this date have not had redshifts measured, and are listed at the bottom of Table 2.1. We will make the reasonable assumption that the same fraction of SNe with measured redshifts which are field SNe applies to these four. Therefore the total number of field SNe used in this chapter is ~ 22.

2.3 Magnitude Limits of the Search

To accurately determine the rate of SNe from a SN search, the efficiency of detecting objects must be accurately assessed. The most important aspect of this is the effective limiting magnitude of the search. The general characteristics of the Abell cluster search and its magnitude limits were described in Chapter 1. By the very nature of this CCD-based search, the detection efficiencies can be more accurately characterized than ever before; this aspect of the search alone can reduce the uncertainties and all but eliminate several pesky systematic effects which have plagued estimates of SN rates which have been computed in the past.

More specifically, in Chapter 1, section 1.5, a method of accurately computing limiting search magnitudes was described, namely by placing a grid of negative "sensitivity stars" artificially into the template image of each field when it is first constructed. Then when the template is subtracted from each subsequent observation, some of the (now positive) artificial stars with known magnitudes are detected along with all of the new SN candidate objects. The magnitude of the faintest of these sensitivity stars which is detected by the software is approximately equal to the effective limiting magnitude of the search.

The relationship between the magnitude of the faintest detected sensitivity star and the true magnitude limit of the search was more quantitatively measured through an extensive series of simulations in which false stars were placed by the thousands

on many different observations of varying quality, both in galaxies and on blank sky. The purpose of this analysis was to determine the shape of the efficiency curve, whether this shape was consistent in observations of varying quality, and whether it is a function of the surface brightness of the host galaxy of the SN and the position of the SN in its host galaxy. Moreover, it was important to determine whether the shape of this curve could be accurately predicted from the number of sensitivity stars that is detected from the grid of nine artificial stars in every observation.

The results of these simulations are summarized in Figure 2.2, which shows the derived efficiency curve for a typical observation. The most important result portrayed in this plot is that the efficiency of detecting point sources on blank sky (solid line) is essentially identical to that of detecting them on the centers of galaxies (dashed line). This is an important result that reveals the major strength of the image-subtraction process which gives this CCD-based search a distinct advantage over previous searches performed on Schmidt plates or by eye. We do not have to correct our detection efficiency based on position relative to galaxies; the search is sky-limited (but see Chapter 4 and Pain *et al.* 1996).

We choose the analytic form

$$\varepsilon = \frac{T}{\mathrm{e}^{(m-m_\mathrm{c})/S}+1}, \tag{2.3}$$

to describe the observed efficiency curve. We show the least–χ^2 best-fit curves to the observed distribution, of the form in eq. 2.3 in Figure 2.2, with the best-fit parameters listed in the figure. Qualitatively, T is the maximum efficiency, which peaks around 95% for all observations. This is offset from unity due to the average lost area caused by the pointing accuracy of $\pm 16''$ (± 25 pixels) of the MSSSO 1.3m telescope. Therefore an annulus of $\sim$ 25 pixels ($\pm 3\%$ of each image) on average cannot be searched on each 1024×2048–pixel amplifier-image. m_c, the "cutoff magnitude," is the apparent magnitude where the efficiency falls to $T/2$. The parameter S may be

thought of as the "sharpness" of the efficiency curve, and is the only parameter that defines the curve's shape. It was found that S depends very little on the quality of the observation, and the efficiency curve only shifts from higher to lower apparent magnitude (varying m_c) as the seeing and sky brightness of the observation changes. The other two parameters vary little, and we used the median values $T = 95\%$ and $S = 0.16$, determined from the Monte-Carlo artificial star tests, throughout this project.

Another set of Monte-Carlo simulations revealed that the apparent magnitude of the faintest sensitivity star (in the grid of nine) that is detected in each observation ($m_{\rm sens}$) does not equal m_c, the cutoff magnitude of the corresponding efficiency curve of that observation. This is to be expected due to the discreteness of the magnitude increment between subsequent sensitivity stars ($m_{\rm step}$), since on average, stars that are brighter than m_c will be detected while those that are fainter will not. For $S = 0.16$ and $m_{\rm step} = 0.5$ (the value we used throughout the search), we find that $m_c = m_{\rm sens}+0.185\pm0.29$. With all of this information, we can now use the magnitude of the faintest sensitivity star detected from the grid of nine, which we have recorded for each of the 2540 observations considered here, to accurately predict the shape of the efficiency curve of each observation to within ±0.3 mag.

Of the 92 fields in the survey, all but four have been photometrically calibrated via $BVRI$ observations of the fields obtained on the CTIO 0.9m in during a total of seven photometric nights in August, 1998 and January 1999. The calibrations were performed in the usual manner. Once the nightly airmass and color terms were determined from regular observations of southern and equatorial Landolt (Landolt 1992) standard fields, the magnitudes of secondary stars in each of the Abell fields were converted to normalized MaCHO magnitudes via the relationships given by Bessell & Germany 1999. The uncertainty in the photometric calibration was computed from the magnitudes of calibrated stars of several fields which were observed on more than one separate night at CTIO; it is around ±0.02 mag. There is like-

ly to be a systematic uncertainty in the calibration, largely due to the conversion of standard $BVRI$ to V_M and R_M, of roughly ± 0.1 mag. The photometric offsets computed in this way were used to calibrate the magnitudes of the sensitivity stars in each field by determining the photometric offset required to calibrate each field's template image. For the calibration of the four fields which we were unable to observe at CTIO, the mean of the offsets utilized to calibrated the other 88 fields, ~ 0.1 mag in both V_M and R_M, were used.

Unfortunately one further complication exists. As was explained in Chapter 1, the final cut on the supernova candidate list that is created by the automated search software is made by eye. There are a rather subjective set of criteria which are used to make the collective decision of which objects are worthy of reporting to the IAU. Objects that appear to be real but are too close to the level of noise to be trustworthy are recorded but not reported unless they are seen in later search observations. Other bright objects that appear to be too red, or do not have an apparent nearby host galaxy are similarly noted for future confirmation. These criteria cannot be quantitatively incorporated into the detection efficiencies. Rather, it was noted that no SNe in our sample of 46 objects were detected at magnitudes fainter than 20.5, even though $m_{\rm c}$, as determined from the faintest sensitivity star detected, often reached fainter than 21. This "magnitude ceiling", $m_{\rm ceil}$ was then imposed in the calculation of the control times (§2.4) to reflect this fact. Effects of the uncertainty in $m_{\rm ceil}$ on the derived rates will be discussed in Section 2.7.

2.4 Control Times

The first part in the definition of a SNu (Equation 2.1) is the total time during which a SN could have been detected by the SN survey in question, in SN century^{-1}. The notion of the "control time" of a SN search was first introduced by Zwicky 1938, Zwicky 1942. Until a decade ago (van den Bergh & Tammann 1991, Cappellaro *et*

al. 1993a, Cappellaro *et al.* 1993b), it was assumed that type-Ia and -II SNe each exhibit uniform peak brightnesses, and that they then required large inclination corrections to take extinction by the SN host galaxy into account. van den Bergh & McClure 9894 were the first to bring both of these assumptions into doubt in their calculation of the SN control times. Our SN search, which scans a large sample of anonymous galaxies at a wide range of redshift requires a further refinement in the control times calculations, combining the methods of van den Bergh & McClure 9894 and Cappellaro *et al.* 1997 with those of Pain *et al.* 1996. We describe it below.

The amount of time which a SN is detectable, its "control time", $t_{\rm c}$, is of course dependent on many variables:

- The intrinsic magnitude of the SN. Here it will be parameterized with Δ, the difference between a SN's peak magnitude and the mean peak magnitude for its type, $\overline{M}_{\rm peak}$. For type Ia SNe, Δ also parameterizes the width of the light curve (*e.g.* Phillips 1993).

- The shape of the SN light curve. SNe with slower-declining light curves are visible for a longer amount of time. This is largely parameterized by the SN type; however for SNe Ia it is also related to Δ.

- The redshift of the SN. More distant SNe are less easily detectable and therefore have a smaller $t_{\rm c}$ because they appear fainter as their luminosity distance increases. A SN's apparent brightness also changes with z due to variations in its K-correction as different parts of its spectrum are shifted in and out of the passband of the detector; therefore the effect of redshift differs between different SN types. The control time of a SN also increases with z due to the time-dilation of its light curve.

- The reddening, E_{B-V}, that the SN experiences due to dust along its line of

sight. This selectively extinguishes shorter wavelengths more strongly and is therefore also dependent on the SN's type and redshift.

In summary, the total control time for a search must then be a function of the type, peak brightness, redshift, and extinction (reddening) of the SNe, *i.e.*

$$t_{\rm c} = t_{\rm c}\left(\text{type}, \Delta, z, E_{B-V}\right). \tag{2.4}$$

The control time is also dependent on the chosen cosmology. For the remainder of this paper, computations are performed for a universe consistent with the distant SN Ia observations: a flat universe with Hubble parameter $H_0 = 65$ km sec^{-1} Mpc^{-1} and $(\Omega_{\rm M},\, \Omega_\Lambda) = (0.3,\, 0.7)$. The SN rates scale as H_0^2. We will also do the computations for $(\Omega_{\rm M},\, \Omega_\Lambda) = (0.3{,}0.0)$ and $(1.0{,}0.0)$ cosmologies (table 2.4), although the effect of these two parameters on the rates will be small at these modest redshifts.

2.4.1 Template Light Curves

The computation of $t_{\rm c}$ for each field is performed over a grid of values for type, Δ, z, and E_{B-V}, by first computing the SN light-curve at each value. For this search, light curves are computed in each of V_M and R_M from a template light-curve for each type. For the remainder of this manuscript, calculations will be performed for SNe of type Ia, II-L and II-P. While the population of SNe Ia is homogeneous and is rather well understood, and therefore their SN rates may be readily computed, type II-P and II-L SNe comprise an extremely broad range of characteristics, from light-curve shape to spectral evolution. Our understanding of these objects as a population is further complicated by their wide range of peak brightnesses and extinctions, making the shape of their luminosity distribution essentially unknown. The extremely underluminous SN 1987A is a perfect example of this predicament; it is not known whether extremely faint type-II SNe are rare events, or actually dominate the luminosity

distribution. SNe Ib and Ic are not considered here since the diversity of their light curves is less understood than that of SNe Ia, and we have no such objects in our entire set of spectrally classified SNe. For the purposes of this chapter , we primarily consider the two basic classifications of supernovae: type Ia SNe and core-collapse SNe. The rate of core-collapse SNe cannot be well-constrained, but our approach is to attempt to place limits on their rate by assuming that type II-P and II-L light curves can be used to reasonably bracket the range of characteristics that is seen in the population of core-collapse SNe, overall.

For type Ia SNe, the first-order multi-color light-curve shape vectors of Riess, Press, & Kirshner 1996 are used for template light curves. These consist of a fiducial template light curve $\mathcal{F}(t)$, and a vector $\mathcal{R}(t)$, the linear offset which describes how the light-curve shape changes as the peak brightness (Δ) varies from that of the template. It is a convenient way to parameterize the peak-brightness – light-curve width correlation of SNe Ia first quantified by Phillips 1993, *i.e.* $\mathcal{M}(t) = \mathcal{F}(t) + \mathcal{R}(t)\Delta$. The first-order description was deemed to be better for our purposes than the more recent second-order refinement of Riess *et al.* 1998 and Jha *et al.* 1999, which exhibits unrealistic behavior for unusual SNe Ia ($|\Delta| \gtrsim 0.6$) which were not present in the original training set, but will be required here. By using these MLCS vectors for our template light curves, intrinsically brighter SNe Ia have a greater control time not only because they are brighter, but also because they remain bright for a longer amount of time than fainter SNe Ia. The template SN Ia light curves are supplemented by imposing a rising profile that matches that seen in the nearby sample of SNe by Riess *et al.* 1999b: $L \propto (t + t_r)^2$, where $t_r = 19.98 \pm 0.15$ days is the observed "rise time" in the sample of nearby SNe Ia. It was claimed by Riess *et al.* 1999a that this nearby rise-time is significantly different from the rise time of $t_r = 17.50 \pm 0.40$ days seen by Goldhaber 1998 in distant SNe Ia; if this is indeed true, this evolution in the rise-times will have to be incorporated into the calculations of distant SN Ia rates.

Because of their diversity, a simple description of SN-II light curves has not been developed. Theoretically, Popov 1993 has computed model core-collapse light curves which depend on the characteristics of their progenitors, but these are complicated by factors such as evolution and mass loss. We, instead, divide SNe II into two classes, SNe II-P (plateau) and SNe II-L (linear). For the SNe II-P, the well-observed $BVRI$ light curve of SN 1990E Schmidt *et al.* 1993 is used as a template, and the BV light-curve of SN 1980K Barbon, Ciatti, & Rosino 1982 is used as the template light curve for SNe II-L. Furthermore, the SN-II light curves are simply shifted to brighter/fainter magnitudes for lower/higher values of Δ, without changing the shapes of their light curves.

To calculate $t_{\rm c}$, we begin by creating a SN template light curve, in multiple standard passbands, of the supernova's *absolute* magnitude M as a function of epoch, or time past peak brightness, t. From this template, the observed V_M and R_M SN light curves are computed. The light-curves must be K-corrected, for a given redshift, to derive light-curves which would be observed through the MaCHO passbands (Kim & Perlmutter 1996). The V_M and R_M filter profiles (transmission as a function of wavelength), computed by Bessell & Germany 1999 by measuring colors of a wide range of standard stars, are used here. The homogeneity of the spectral evolution of SNe Ia enables us to use a collection of SN Ia spectra covering epochs between $-11 \leq t \leq 75$ days to determine generalized type Ia K-corrections. The spectral evolution of type-II SNe varies greatly from SN to SN if traced as a function of epoch. However, SNe II follow a more regular spectral sequence when traced as a function of color, *i.e.* temperature of the expanding photosphere (Schmidt, Kirshner, & Eastman 1992). K-corrections were computed using the SN 1987A spectra of Phillips *et al.* 1990, over a range from ~ 0 to 800 days past explosion. II-L and II-P K-corrections as a function of epoch were then estimated by finding the epoch in the in which the $B-V$ color of SN 1987A equaled that of the II-L or II-P template light-curve. A second-order spline was used to interpolate K-corrections for epochs for

which there was no available spectrum. Finally, the redshifted spectra are artificially reddened using the extinction law of Schlegel, Finkbeiner, & Davis 1998 to derive $K_c(t, z, E_{B-V})$. K-Corrections were calculated from R to R_M and from V to V_M, *i.e.* , from the closest respective standard passband to its corresponding MaCHO filter, in order to minimize the uncertainties.

The final *observed* SN light-curve (apparent magnitude m as a function of epoch t) is derived for the two MaCHO filters F_M from the expression

$$m(t, z, E_{B-V}, \text{type}, F_M) = M\left(t \times (1+z), \text{type}, F\right) + 5\log\left(\frac{c}{H_0} D_L(z)\right) + K_{c,F_M \Rightarrow F}\left(t \times (1+z), z, E_{B-V}, \text{type}\right) + E_{B-V} \times R_F + 25, \quad (2.5)$$

where the luminosity distance $D_L(z)$ depends on ($\Omega_{\rm M}$, Ω_Λ), F is the standard filter (V or R) that the template light curve was observed in, and R_F is the extinction coefficient used to derive the total extinction A_F experienced by an object observed in filter F, for which there is a reddening E_{B-V}. Note that the generalized K-correction $K_{c,F_M \Rightarrow F}$ (which includes the cross-filter color term from the MaCHO filter F_M to the standard filter F) is *added* in equation 2.5, because we are calculating the observed brightness in non-standard pass-bands, given the intrinsic brightness in standard filters. The uncertainties in the template light-curves and their various corrections are expected to contribute to systematic uncertainties in the derived SN rates; this will be discussed in Section 2.7.

2.4.2 Probability of Detection

The next important variable in the computation of the control time is the time of explosion of the SN. A period of time in which no search observations are made, even if a bright SN occurs in the field, will not contribute to the control time.

Therefore the total control time for a SN of a given type, redshift, and reddening value is computed for a given passband from the total probability that it would be detected over all possible times at which the SN could have exploded. A SN light-curve is produced, as described above, with a given date of explosion (in the observer's frame), t_e. For each date, t_o, in which a search observation was obtained, the apparent magnitude m_o of the SN is derived, as is its apparent magnitude when the template observation was taken, m_t. The flux corresponding to the latter value is subtracted from that of the prior, to derive the apparent magnitude of the SN as it would appear in the template-subtracted image, $m_o - m_t$. The subtraction of the template flux is an important detail as it can decrease the control time substantially, especially at low redshifts, if the time between template and search observations is $t_o - t_e \lesssim 30$ days for SNe Ia ($\lesssim 100$ days for SNe II-P with their slower-evolving light curves). This subtraction is not as big an issue here since $t_o - t_e$ is typically $\gtrsim 2$ months (this is because once a template is constructed it is used indefinitely until a better-quality image of the same field is observed, even though each field is still observed every 2–3 weeks on average), but it becomes important for the targeted high-redshift searches where $\Delta t \simeq 2$ weeks by design (Chapter 4).

The probability of detection of an object with a given observed magnitude (including subtraction), $\mathcal{P}(m_o - m_t)$, is estimated from the magnitude of the faintest sensitivity star that was detected in that observation, as described in Section 2.3. This calculation is performed for both MaCHO filters, and then the probabilities are multiplied together to satisfy the requirement that the SNe must be detected simultaneously in both passbands. The total probability that the SN which exploded at time t_e will be detected by any of the numerous observations of a given field, is then

$$\mathcal{P}\left(t_e\right) = 1 - \prod_o \left[1 - \mathcal{P}\left(m_o - m_t\right)\right]. \tag{2.6}$$

Next, t_e is incremented by one day, and $\mathcal{P}(t_e)$ is calculated anew, for all reasonable

times of explosion. Finally, the control time, in days, is then

$$t_{\rm c} = \sum_{e} \mathcal{P}\left(t_e\right). \tag{2.7}$$

The control time, $t_{\rm c}({\rm type}, \Delta, z, E_{B-V})$ was calculated for each of the 92 fields, individually, following this prescription.

2.4.3 Integrated Control Times

The calculation of $t_{\rm c}({\rm type}, \Delta, z, E_{B-V})$ is straightforward given a SN light curve shape and absolute peak magnitude, and is not subject to any assumptions about the overall population of the SN types in question. To make the total control times tractable requires us to make some assumptions, in order to narrow down the number of parameters upon which $t_{\rm c}$ is dependent. We choose reasonable probability distributions $\mathcal{F}(\Delta)$ (the SN luminosity function) and $\mathcal{F}(E_{B-V})$ (the extinction distribution), for each SN type, and then integrate:

$$t_{{\rm c},tot}({\rm type}, z) = \int \left[\int t_{\rm c}\left({\rm type}, \Delta, z, E_{B-V}\right) \mathcal{F}(\Delta) d\Delta \right] \mathcal{F}(E_{B-V}) dE_{B-V}. \tag{2.8}$$

The resulting total (integrated) control time for all SN types, given their luminosity and extinction distributions, is a function of SN type and redshift only. The distinct advantage of computing $t_{\rm c,tot}$ in this manner is that one needs to perform, only once, the extensive calculations necessary to derive $t_{\rm c}({\rm type}, \Delta, z, E_{B-V})$, for each field. Integrating the control time in equation 2.8 is a much quicker calculation, allowing a complete exploration of the parameter space (the shape of $\mathcal{F}(\Delta)$ for example), for all of the parameters which may influence the derived SN rates.

2.4.4 SN Population Parameters

The luminosity function of SNe Ia is the best understood distribution of those SN types considered here. Since our template SN Ia light-curves are taken from those of Riess, Press, & Kirshner 1996, we will use the distribution of MLCS Δ parameters which they computed using the first-order MLCS vectors as fitting templates. These were calculated for a large sample of well-observed objects, using a more realistic empirical E_{B-V} distribution than that used by Riess *et al.* 1998 (but see Jha *et al.* 1999). The Cepheid-calibrated absolute magnitude of the fiducial ($\Delta = 0$) template light curve is given by Jha *et al.* 1999 as $M_B(\mathrm{peak}) = -19.34 \pm 0.20$ ($H_0 = 65$). The sample of 20 SNe Ia, when fit using the linear MLCS vectors, have a mean Δ of 0.010 with a dispersion of 0.41 mag. This is very similar to the more recent measurement by Jha *et al.* 1999 who find a dispersion in M_{peak} of 0.366 (private communication). Similarly, Hamuy *et al.* 1996b computed the distribution of SN Ia peak luminosities for their Calán/Tololo SN Ia sample (a significant number of which are also used by Jha *et al.* 1999), and obtained very similar values for the SN Ia luminosity distribution, $M_B(\mathrm{peak}) = -19.28 \pm 0.38$ ($H_0 = 63.3$). Note that these values are not corrected for selection effects experienced by the Calán/Tololo SN search (whose SNe comprise most of the well-observed nearby SN Ia sample); however Hamuy & Pinto 1999 assures us that these will have negligible effect on the derived SN rates, as using a better M_B distribution has a 2nd-order effect on the computed rates. Other recent Cepheid-calibrated SN Ia peak magnitudes (Kochanek 1997, Tammann & Reindl 1999) agree with the values we have chosen to use here, when the same Hubble parameter is used. We therefore adopty a Gaussian SN Ia distribution with a mean of $\overline{M}_{B,\mathrm{Ia}} = -19.33 \pm 0.20$ and dispersion of $\overline{\sigma}_{\Delta,\mathrm{Ia}} = 0.41 \pm 0.05$ for our model SN Ia luminosity distribution.

In contrast to the relatively well-constrained luminosity function of SNe Ia, the heterogeneity, relatively poor quality of observations, and wide range of extinctions

experienced by core-collapse SNe makes their luminosities much more difficult to characterize. This is most clearly illustrated by Patat *et al.* 1993. Tammann 1990 plotted a histogram of SN II peak brightnesses, and showed a roughly Gaussian-shaped distribution with a large ($\sim$ 2 mag) dispersion. Miller & Branch 1990 analyzed the SN II-L and SN II-P absolute magnitude distributions, and found $M_B = -17.2 \pm 0.35$ with $\sigma_B = 1.39$ for SNe II-P and $M_B = -17.8 \pm 0.44$ with $\sigma_B = 1.24$ for SNe II-L ($H_0 = 65$ km sec^{-1} Mpc^{-1}). These values are uncorrected for reddening. Since we are going to attempt to include a modelled reddening distribution for type II SNe, which only increases the uncertainties in the luminosity distributions, and because we would also like to incorporate the large uncertainties in light-curve shapes and generalized K-corrections for SNe II, we choose to use $\overline{M}_{B,\mathrm{II-L}} = -18.0 \pm 0.5$, $\overline{M}_{B,\mathrm{II-P}} = -17.0 \pm 0.5$ and $\overline{\sigma}_{\Delta,\mathrm{II}} = 1.25 \pm 0.5$ mag. As a final detail of our calculations, in the computation of the total type-II SN rate, we fix the ratio of II-L and II-P to 1:5. We choose this ratio because although SNe II-L are $\sim$ 2.5 times brighter than SNe II-P (on average), roughly twice as many SNe II-P have been detected (*e.g.* Miller & Branch 1990), suggesting that they occur $\sim$ 5 times more frequently. The exact size of this ratio has very little effect on the final SN II rates because of the intrinsic infrequency and faintness of SN-II-L events relative to SNe-II-P.

Hatano, Branch, & Deaton 1998 modelled the extinction that would be experienced by SNe placed in exponential disks with random inclination. The model includes only a smooth dust distribution, most applicable to SNe Ia, and results in a sharply peaked distribution that falls off with a broad tail to higher A_B. The observation that some SNe Ia are correlated with the spiral arms of spiral galaxies (van den Bergh 1990) suggests that perhaps a fraction of them can be attributed to a younger stellar population, in which a smooth dust distribution might not be applicable for SNe Ia either. The recent measurements of A_V for 42 local SNe Ia by Jha *et al.* 1999 via the 2nd-order MLCS light-curve fitting technique of Riess *et al.*

1998 support this notion, with a broader reddening distribution than that predicted by Hatano, Branch, & Deaton 1998 and an overabundance of significantly reddened SNe. This empirically derived reddening distribution has a major caveat in that it is difficult to define which SNe are reddening-free, and therefore the entire reddening distribution can shift to higher or lower values depending on the form of the zero-extinction SN selection. Because of the poor match between the model distribution of Hatano, Branch, & Deaton 1998 and the observed one, we will use the observed A_V distribution of Jha *et al.* 1999 for our distribution of SN Ia extinctions.

The extinction distribution of core-collapse SNe, $\mathcal{F}_{\rm II}(E_{B-V})$, is much more difficult to constrain, either observationally (because of the inhomogeneity in the color evolution of SNe II), or theoretically. While Hatano, Branch, & Deaton 1998 attempted to model it using a smooth dust distribution, and still found that many core-collapse SNe experience more extinction than SNe Ia due to their smaller vertical scale height in the disk, they did not include the clumpy dust distribution that one would expect a large fraction of core-collapse SNe to experience. Any model of $\mathcal{F}_{\rm II}(E_{B-V})$ which includes such clumpiness will be ad-hoc, but must be consistent with observations of extinction experienced by massive stars in star-forming regions. These observations, such as those of OB associations in M31 (Magnier *et al.* 1997), HII regions in M101 (Scowen *et al.* 1992), or bright HII regions in several nearby galaxies (Kennicutt *et al.* 1984; McCall *et al.* 1985), all support broad ($\sigma \gtrsim 1$ mag) extinction distributions that extend as high as $A_V \simeq 3$ mag, with means near $\overline{A_V} \simeq 1.0$ mag. More directly, Schmidt *et al.* 1994, comparing $(B-V)$ and $(V-I)$ colors of their 16 EPM SNe II to colors of well-observed SNe (including SN 1987A), found a mean extinction of $\overline{A}_V \simeq 0.6$ mag with a dispersion of ~ 0.75 mag. They found that a reasonable number of SNe experience an extinction of $\gtrsim 1$ mag (and even as high as $A_V \simeq 2.7$ mag), while several appeared to undergo very little (~ 0) reddening. We have therefore chosen to use a Gaussian distribution for $\mathcal{F}_{\rm II}(E_{B-V})$, with a mean extinction of $\overline{A}_V = 1.0$ mag ($\overline{E_{B-V}} \simeq 0.35$) and a width of

$\sigma_{A_V} = 1.0$ mag (truncated at $E_{B-V} = 0$). Of course, to try to differentiate $\mathcal{F}_{\rm II}(\Delta)$ from $\mathcal{F}_{\rm II}(E_{B-V})$ is probably unrealistic, but it is nonetheless the way we choose to model the SN II population, enabling an independent exploration of the effects on the SN II rate of the luminosity function and extinction distribution.

The E_{B-V} distributions described above are shifted by the amount equal to the foreground galactic extinction prior to integrating equation 2.8. These values are calculated at the coordinates of each Abell cluster from the E_{B-V} maps provided by Schlegel, Finkbeiner, & Davis 1998, and provide a means of incorporating the effects on the control times of both the reddening and extinction caused by dust in our own galaxy.

Using the model parameters described above, and integrating the total control time via equation 2.8 reveals the effectiveness of our search as a function of redshift. This is displayed in Figure 2.3, for SNe Ia (solid line) and SNe II-P + II-L added together with the ratio 5:1 (dashed line; see above). The y-axis has been normalized to units of total control time per field, in years, suggesting that, for example, the MSACSS would have detected roughly 1/3 of the SNe Ia which occurred at $z = 0.05$ during the 30 months of the search in our target fields. This small fraction can be attributed entirely to the amount of time that the clusters were behind the Sun, plus weather.

2.5 Integrated Galaxy Luminosity

The integrated luminosity of the galaxies which were surveyed is among the quantities which contribute the most uncertainty to the derived SN rates. It is necessary because it defines the galaxy control sample of the search. Earlier SN rate calculations have been based largely on the products of nearby SN searches, which have targeted individual galaxies. They therefore utilize the catalogued luminosities of the targeted galaxies to derive the total luminosities of their control sample, such

as the extinction-corrected magnitudes of the Third Reference Catalogue of Bright Galaxies (de Vaucouleurs *et al.* 1991), used by Cappellaro *et al.* 1997. Deeper searches, such as the MSACSS, the Calán/Tololo survey (Hamuy *et al.* 1995), and the high-redshift SN searches (Schmidt *et al.* 1998, Perlmutter *et al.* 1995), cannot use this technique however since they do not target individual galaxies but rather survey large fields of anonymous galaxies and even empty space where no galaxies are visible. Here, the total galaxy luminosity must instead be estimated from other measurements of the local galaxy luminosity density and the total volume surveyed.

Several galaxy redshift surveys conducted during the past decade have contributed to our knowledge of the local galaxy luminosity density. They are usually computed by integrating the galaxy luminosity function of the high surface-brightness galaxies in their surveys. Examples include the oft-referenced measurements of Loveday *et al.* 1992, Marzke, Huchra, & Geller 1994, and Lilly *et al.* 1995, who derived local luminosity densities of $\mathcal{L}_{B,\mathrm{local}} = 1.35, 2.1$, and $2.18 \times 10^8 h L_\odot \mathrm{Mpc}^{-3}$, respectively. Fukugita, Hogan, & Peebles 1998 review the recent measurements of $\mathcal{L}_{B,\mathrm{local}}$ and conclude that the evidence supports

$$\mathcal{L}_{B,\mathrm{local}} = (2.0 \pm 0.2) \times 10^8 h L_\odot \mathrm{Mpc}^{-3}, \tag{2.9}$$

and this is the value we choose. It should be noted that this value is not corrected for extinction, and cannot be compared directly with rates derived using extinction-corrected luminosities. Hamuy & Pinto 1999 used $\mathcal{L}_{B_T,\mathrm{local}} = (1.65 \pm 0.42) \times 10^8 h L_\odot \mathrm{Mpc}^{-3}$ provided by Marzke (Lilly, S. J., private communication), where B_T is defined to account for the whole integrated light of his sample. While this value is surprisingly *lower* than the one we have adopted, the uncertainties overlap. The SN rate reported by any group is directly (inversely) proportional to the $\mathcal{L}_{B,\mathrm{local}}$ used, so a comparison of the rates derived here to those of Hamuy & Pinto 1999 or Cappellaro *et al.* 1997 is straightforward.

With a limiting magnitude that sometimes reaches $V_M \gtrsim 21$, our search has a non-negligible control time for $z \gtrsim 0.25$ (where a SN Ia with $\Delta \simeq -0.3$ has $M_B \simeq 21.0$). Even at these modest redshifts, recent observations have shown that there is a significant increase in the blue galaxy luminosity density over the local value. Lilly *et al.* 1996 integrated the galaxy luminosity functions, in different redshift bins, from the Las Campanas Redshift Survey to derive the comoving galaxy luminosity density at 4400 Å as a function of redshift, $\mathcal{L}_B(z)$. They found that it is well-fit by a power-law, $(1+z)^{\alpha_L}$, with $\alpha_L = 2.7 \pm 0.5$ for $q_0 = 0.5$, $\Omega = 1.0$. At a redshift of ~ 0.3 this is an increase of a factor of two. The redshift-dependence in the comoving luminosity density is directly proportional to the redshift-dependence of $\mathcal{L}_B(z)$ in the comoving differential volume element (private communication). We therefore scale the redshift-dependence reported by Lilly *et al.* 1996 by the volume element for our ($\Omega_{\rm M} = 0.3$, $\Omega_\Lambda = 0.7$) cosmology to derive a final redshift-dependent blue galaxy luminosity density. This offset in the $(1+z)^{\alpha_L}$ dependence can be approximated by an offset of ~ -0.80 in α_L, from the $q_0 = 0.5$, $\Omega = 1.0$ calculations of Lilly *et al.* 1996. Thus the blue galaxy luminosity density used here may be expressed by the following approximation:

$$\mathcal{L}_B(z) \simeq (2.0 \pm 0.2) \times (1+z)^{(1.9 \pm 0.5)} \times 10^8 h L_\odot \mathrm{Mpc}^{-3}. \qquad (2.10)$$

It should be reiterated that this expression is only an approximation to the Lilly *et al.* 1996 result modified for our cosmology and is included only for reference; we instead use the true differential volume ratios for our calculation. The total galaxy luminosity surveyed, $L_B(z)$, is then simply $\int \mathcal{L}_B(z) dV(z,\Omega)$, where $dV(z,\Omega)$, the comoving cosmological volume element, is integrated to redshift z, and over the total area on the sky surveyed (Ω), here, 47.84 deg^2 (92 fields, each providing 0.52 deg^2 of sky coverage), or 0.0145 steradians.

Modelling the R-band luminosity density to estimate the rates in SNu$_R$ is not

so straightforward since there have been fewer redshift surveys conducted in the red rather than the photographic $b_{\rm J}$ of earlier surveys. The Canada-France Redshift Survey (CFRS; Lin *et al.* 1996) was performed in Gunn-r, and they report an anomalously shallow luminosity function with $M^* = -20.29$, $\alpha = -0.70$ and $\phi^* = 0.019$ Mpc^{-3} ($H_0 = 100$) for a total local luminosity density of $1.19 \times 10^8 L_{r_\odot}$ Mpc^{-3}. The more recent and significantly deeper Century Survey (CS; Geller *et al.* 1997) conducted in R, found $M^* = -20.73$, $\alpha = -1.17$ and $\phi^* = 0.0250$ Mpc^{-3}, integrated to derive $2.96 \times 10^8 L_{R_\odot}$ Mpc^{-3}. The obvious disparity (of more than a factor of two) between the two is explained by Geller *et al.* 1997 by the much greater depth of the latter survey, however noting that $r - R = 0.35$ for a "typical" field galaxy (Jorgensen 1994), we derive for the CFRS a local luminosity density of $1.64 \times 10^8 L_{R_\odot}$ Mpc^{-3}. We adopt the average of these two values, $2.3 \times 10^8 L_{R_\odot}$ Mpc^{-3}. It is refreshing to confirm that, as Geller *et al.* 1997 point out, with $b_{\rm J} - R_{\rm KC} = 1.3$ for the mix of morphological types found in the CS, a mean blue luminosity density from this value of exactly $2.0 \times 10^8 L_{B_\odot}$ Mpc^{-3} may be found. To estimate a power-law increase in the red-band luminosity density with redshift similar to eq. 2.10, we must interpolate between the Lilly *et al.* 1996 exponents of $\alpha_L = 2.1$ at 1μm and 2.7 at 4000 Å, and then offset by ~ -0.8 to be consistent with our chosen cosmology (see above). We therefore use a value of 1.4 ± 0.5 for $\alpha_{L(R)}$.

Figure 2.4 shows $L_B(z)$, for a single MaCHO field, as the solid line, integrated in bins of 0.02 in redshift. Also plotted for reference as dotted lines are the $\pm 1\sigma$ uncertainties (assuming that the two uncertainties in equation 2.10 are uncorrelated) as well as the values one would derive if there were no increase in comoving luminosity density with redshift, ($\alpha_L = 0$), whereby the total luminosity would only increase with volume (dashed line).

As one additional detail peculiar to this search, in our final SN rates calculation, we do not count any control luminosity computed within the redshift range range $|cz - cz_{\rm clust}| < 1500$ km sec^{-1} ($z_{\rm clust}$ is the measured redshift of the cluster) because,

according to eq. 2.2, no supernovae in these redshift ranges are included as *field* supernovae. This increases the resulting rates by $\lesssim 10\%$.

2.6 The Field Supernova Rates

If the supernova rate in SNu, $r_{\rm SN}$, is constant with look-back time (a verifiable supposition, and one that we will assume is true over the small range of redshifts relevant to the MSACSS; see also Chapter 4), then by equation 2.1, one would expect that, for a given SN type,

$$N_{\rm SN}(z) = r_{\rm SN} \times t_{\rm c,tot}(z) \times (1+z) \times L_B(z), \tag{2.11}$$

where the control time must be time-dilated to derive the true rest-frame rate. In other words, the observed redshift distribution of field supernovae detected in a search, of a given type, can be predicted by the total control time (as portrayed in figure 2.3) $\times$ the total galaxy luminosity (shown in figure 2.4) surveyed. These two factors multiplied together give the total SNu^{-1} surveyed, and the constant of proportionality in eq. 2.11, $r_{\rm SN}$, is the value we seek.

The observed distribution can be compared to the predicted distribution of SNe with redshift to compute the overall SN rate,

$$r_{\rm SN} = \int_z \frac{N_{\rm SN}(z)}{t_{\rm c,tot}(z) \times L_B(z) \times (1+z)} dz, \tag{2.12}$$

and in this manner, we derive a rate of supernovae in field galaxies from the MSACSS of $r_{\rm Ia} = 0.164$ SNu and $r_{\rm II} = 0.997$ SNu.

Given these rates, figure 2.5 shows the expected number of supernovae $N_{\rm SN}(z)$ computed via equation 2.11 plotted alongside the observed redshift distribution of field supernovae from this search, where SNe II are shown in the top-left to bottom-

right hatched histogram, SNe Ia in the bottom-right to top-left hatched histogram, and unclassified SNe in the un-hatched histogram. In computing the SN rates, the unclassified SNe were given probabilities that they were either a type Ia or type II SN based upon the relative values of the $N_{\rm SN}$ curves at their redshifts. Additionally the four SNe whose redshifts were not measured are assigned SN types based simply in the ratio of the total SN numbers predicted by the curves (*i.e.* $\int_z N_{\rm SN}(z)dz$). The rates are repeatedly re-computed until convergence is reached. This iterative procedure slightly increases the uncertainty of the derived rates, but it is much more acceptable than only including classified SNe in the rates calculation and then having to quantify the extremely complicated selection criteria that influenced whether a SN could be successfully redshifted and/or classified. Therefore, the SN Ia and SN II rates are computed simultaneously and are somewhat correlated as a result of the calculation.

Some useful information may be gleaned from a close examination of Figure 2.5. The most important feature is the fine match between the predicted and observed redshift distributions of the SNe of both types. A simple Komolgorov-Smirnov test shows that we can reject the null hypothesis that the predicted and observed distributions are *not* the same with a probability of only $\sim 30\%$. With a larger sample size (and greater statistical accuracy), the authors envision using this technique to constrain certain SN population parameters while simultaneously measuring the SN rates, perhaps even as a function of redshift, through a maximum-likelihood technique. This will allow not only a more direct evaluation of the systematic effects involved in using SNe Ia as cosmological distance indicators, but also will provide a method to trace the evolution of the SN rates and other SN characteristics with look-back time.

Additionally, the mean, or effective, redshift for which the rates have been computed may be estimated from the $N_{\rm SN}(z)$ curve,

$$\overline{z_{\rm eff}} = \frac{\int N_{\rm SN}(z) z dz}{\int N_{\rm SN}(z) dz}. \tag{2.13}$$

For this search, $\overline{z_{\rm eff}} = 0.114$ for the SNe Ia, and 0.084 for the fainter core-collapse SNe (whose redshift distribution is dominated by the brightest SNe in the broad SN-II luminosity distribution).

We have also derived the rates in SNu_R for comparison. They have essentially the same uncertainties, but slightly smaller values due to the greater local R-band galaxy luminosity density. We find rates of 0.152 and 0.934 SNu_R for SNe Ia and core collapse events, respectively. This number cannot be compared to other measurements of the same quantity but will offer interesting insight when compared to the rates derived in clusters and at higher redshift (chapters 3 and 4).

2.7 Uncertainties and Systematic Errors

All of the parameters used to compute the integrated control times (described in Section 2.4.4) and the estimate of the total control luminosity (summarized in Section 2.5) have uncertainties which contribute to systematic errors in the computed SN rates. Additionally the uncertainties in the estimation of the limiting magnitudes will contribute statistical and systematic errors to the rates. There is also a large statistical contribution to the uncertainties in the rates, which are made slightly more complicated by the iterative process required to compute the rates that was described at the end of Section 2.6. In the estimation of all of these contributions to the uncertainties in the derived rates, we attempt to remain on the conservative side, and where the uncertainties are difficult to quantify, we will attempt to over-estimate their sizes.

The calculation of the uncertainties is complicated by the probabilistic "assignment" of SN classifications to those whose types are not known (described in §2.6).

Furthermore, there are four SNe whose redshifts are unknown, and we are therefore not able to ascertain which of these are cluster, or field, SNe. A reasonable fraction of these four are given field SN status, based on the relative fraction of SNe which were identified as field SNe (very close to 1/2). The SN numbers, before and after the "re-assignment" (identified as "observed", and "expected" numbers), are listed in Table 2.2.

The statistical uncertainty $\sigma_{\rm stat}$ for each SN type is simply taken as Poisson, $\sqrt{N_{\rm exp,tot}}$. We must also make a estimate of the uncertainty that arises from the need to assign probabilities of SN classifications to the few SNe that were not spectrally classified. We believe that it is reasonably conservative to assume that 1/2 of these probabilistically-assigned SNe could have been "mis-classified", and herefore an additional uncertainty $\sigma'_{\rm stat} = [(N^{\rm Ia}_{\rm exp,tot} - N^{\rm Ia}_{\rm obs}) + (N^{\rm II}_{\rm exp,tot} - N^{\rm II}_{\rm obs})]/2$ is added to $\sigma_{\rm stat}$, in quadrature, to derive the final statistical uncertainty $\sigma_{\rm tot}$. These uncertainties are all listed in Table 2.3.
The uncertainty due to the un-classified SNe is then at the $\sim 20\%$ level, but only adds $\sim 10\%$ to the total statistical uncertainty when added in quadrature.

The various parameters which contribute to the systematic uncertainty in the SN rates were all described in Sections 2.3, 2.4 and 2.5. They are listed in Table 2.4, column 1, and the values used for the derived rates are in column 2. Columns 3 and 4 list the estimated ranges in these parameters which increase, respectively, the upper and lower ranges on the systematic uncertainties. The contributions to the uncertainty in the rates were computed by altering each parameter by the specified amount, and then either re-integrating the total control times (equation 2.8), or where necessary, re-computing the specific control time for each field (equation 2.4) and then integrating to re-derive the rates. These uncertainties are listed in columns 5-6 and 7-8, for the SN Ia and SN II rates, respectively. The total systematic uncertainty, taken as the quadratic sum of the individual contributions, is listed at the bottom.

Whereas most of the values and their uncertainties that are listed in table 2.4 were explained in earlier sections of this chapter , others will be explained here. We believe that while there was an observation-by-observation uncertainty in the limiting magnitude of 0.3 mag, there is also a $\sim$ 0.1 mag overall systematic uncertainty involved in the process of calculating limiting magnitudes from the magnitudes of the faintest sensitivity stars detected by the search software, as described in §2.3. The first of these uncertainties [m_{lim}(statistical)] fortunately averages out in the computation of the total control times, as our simulations revealed. This is also the case for the $\pm 3\%$ uncertainty, due to telescope pointing errors, in the area of each individual observation that is searched. Also listed in the table, for illustrative purposes only, are the uncertainties derived with a wide range of different SN Ia extinction distributions, and these are not included in the total uncertainty. The SN rates scale as H_0^2 and are also dependent on the cosmology ($\Omega_{\rm M}$, Ω_Λ). However we have not included the uncertainty due to these parameters in the total uncertainty. We have simply chosen to list the amounts by which these parameters affect the rates, for several popular cosmological models.

What is surprising is that, even for SNe Ia whose populations are extremely well understood, the systematics are as large as the statistical uncertainties, suggesting that a better understanding of the SN population and galaxy distribution is more important than significantly increasing the SN sample size (more so for core-collapse SNe).

In summary, the final SN rates are $0.164^{+0.058+0.050}_{-0.058-0.056}(H_0/65)^2$ and $0.997^{+0.54+1.21}_{-0.54-0.47}(H_0/65)^2$ SNu, for type Ia and core-collapse SNe, respectively.

2.8 Discussion

Although these SN rates are the first measurement of the local field SN rates from a completely CCD-based SN search, there are some other recent rates measurements

that are worthy of comparison. The most recent calculation by Cappellaro, Evans, & Turatto 1999, using a large SN sample collected from a variety of photographic and visual searches, obtained a total rate of $(0.20 \pm 0.06)\ (H_0/75)^2$ SNu for SNe Ia and $(0.48 \pm 0.19)\ (H_0/75)^2$ SNu for core-collapse (*i.e.* SN II+Ib/c) SNe. As Hamuy & Pinto 1999 pointed out, the work of Cappellaro, Evans, & Turatto 1999 uses extinction-corrected galaxy luminosities; therefore their rates, while more accurate, will be biased low relative to the rates which we compute here. In Hamuy & Pinto 1999, Capellaro provided an adjusted SN Ia rate, computed with galaxy luminosity uncorrected for internal extinction of $(0.22 \pm 0.06)\ (H_0/75)^2$ SNu. The corresponding core-collapse rate will then be $(0.53 \pm 0.20)\ (H_0/75)^2$ SNu. Converted to our units, these rates are (0.165 ± 0.05) and $(0.40 \pm 0.15)\ (H_0/65)^2$ SNu, respectively. It is startling that although they use a SN Ia luminosity function slightly different from ours, and additionally they employ an empirical inclination-dependent extinction correction that is difficult to compare to the extinction distributions used here, the two SN Ia rates measurements are in good agreement.

For a second recent measurement of the local SN Ia rate, Hamuy & Pinto 1999 computed a value from the Calán/Tololo SN search of $(0.17^{+0.25}_{-0.11})\ (H_0/65)^2$ SNu (scaled to a local galaxy luminosity density of $2.0 \times 10^8 h L_\odot \mathrm{Mpc}^{-3}$). This rate, which does *not* contain any correction for extinction, would be higher if such a correction were made (because the control times would be lower). On the other hand, they include no increase of galaxy control luminosity with redshift as we do; this would decrease their rates by a small amount. Again, the rates are in excellent agreement. It appears that a consensus on the nearby rate of SNe Ia in field galaxies may have been reached.

In general the agreement between the SN Ia rate computed here and the most recent measurements of Cappellaro, Evans, & Turatto 1999 and Hamuy & Pinto 1999 for nearby field galaxies is excellent, regardless of the systematic differences in the particular method of control time and galaxy control luminosity calculations

utilized in the different investigations. We have done our best to quantify both of these uncertainties in our measurement, to reveal exactly how difficult a problem it is to pin down the rate to better than 10%. Our calculations, being based on a CCD-based search, and incorporating the most detailed efficiency, control time and control luminosity calculations, remove some outstanding questions in modern SN rate calculations. However, the agreement with earlier searches suggests that such details, while important, are not required to obtain a reasonable result in the end.

There is no surprise that the core-collapse rate of Cappellaro, Evans, & Turatto 1999 of $(0.53 \pm 0.20)\ (H_0/65)^2$ SNu is lower than the value found here of $(0.997 \pm 0.54)\ (H_0/65)^2$ SNu, even with the large uncertainties of both. This may be partly due to the fact that, as Cappellaro *et al.* 1993a point out, the nearby sample of SNe and the control galaxy sample used by Cappellaro, Evans, & Turatto 1999 is dominated by the Virgo cluster, which will bias their core-collapse rate to be lower than the true field rate. More importantly, the computation of core-collapse rates are subject to large and uncertain extinction corrections. In this paper, they are modelled analytically and incorporated via $\mathcal{F}(E_{B-V})$ into the integrated control time (eq. 2.8). Modelling it as a distribution (rather than with just one mean value, $\overline{E_{B-V}}$), is important because it permits the existence of less-extinguished members of the population, which are more readily detectable. Cappellaro, Evans, & Turatto 1999 used the $\overline{M_B}$ values of Miller & Branch 1990 for SNe Ib/c and II-L/P, which are not corrected for extinction, and then justifiably did not include a mean extinction for these SNe. They then found that their SN rates were higher in spiral galaxies with small inclinations than in those with large inclinations, and made an empirical correction to equalize the values. Whereas this is a reasonable technique to correct for the greater extinction seen in high-inclination galaxies, it does not provide an overall correction for the extinction experienced by the SN sample as a whole, *i.e.* it does not bring the extinctions down to a zeropoint (as we have here, in a model-dependent fashion). In fact, the reddening values found by Schmidt *et al.* 1994 in a sample

of SNe II, or those found by Magnier *et al.* 1997 for OB associations, suggest that core-collapse SNe experience a large average extinction, with individual extinctions ranging over three magnitudes. Which of these reddening distributions best describes the extinctions seen by core-collapse SNe is still unknown. We have computed the core-collapse rates for both cases (*i.e.* the reddening distribution observed in SNe II by Schmidt *et al.* 1994 or the one seen by Magnier *et al.* 1997 in OB associations), and these are described in table 2.4. For example, using an extinction distribution consistent with the Schmidt *et al.* 1994 measurement decreases our type-II rate to ~ 0.747, which is substantially close to that of Cappellaro, Evans, & Turatto 1999.

On the other hand, the MSACSS search is very much a magnitude-limited search, and most SNe II were found very close to the magnitude limits; the sample is then very sensitive to the extinction and magnitude distributions of the underlying population. The sample of Cappellaro, Evans, & Turatto 1999 is largely not subject to the same sensitivities, since most of their sample was collected from nearby SN searches which targeted individual nearby galaxies. The overall picture is that the rate of core-collapse SNe is extremely model-dependent and until we have much better observational constraints on the model distributions, the true value of the core-collapse SN rate will remain quite uncertain. Again, a comparison of these rates among different galaxy populations holds the promise of revealing more about the SNe and their progenitors than does any attempt to measure an actual rate by itself (Ruiz-Lapuente, Canal, & Burkert 1996).

In summary, it is difficult to compare the rates of both SN Ia and core-collapse SNe computed by different authors due to differing assumptions required by the calculations. Because the SN Ia characteristics are so much more easily quantified than those of core-collapse SNe, the agreement between different SN searches on the SN Ia rate is good. Still, a greater amount of information may be gleaned, without as much worry about systematics, by comparing the SN rates derived for different galaxy/stellar populations using the same selection effects and assumptions

throughout, rather than by comparing the SN rate calculations of different authors based on different searches. Cappellaro, Evans, & Turatto 1999 have done just this in computing the SN rates among various galaxy types, and we will do the same by comparing the nearby field SN rates derived here with those seen in nearby rich galaxy clusters as well as with those in distant field galaxies from the High-Z supernova search.

Table 2.1: Table of field supernovae discovered in the MSACSS, including the observed type and redshift, if available, and the redshift of the Abell cluster projected in its direction. "nIa" signifies that the SN is probably *not* type-Ia, but may be of type-Ib/c or type-II.

SN	Abell	Type	z	Cluster z
1996af	A3879	Ia	0.100	0.067
1996ag	A3809	Ia?	0.140	0.062
1996aj	A3559	Ia	0.110	0.046
1996bm	A2819	II?	0.164	0.075
1996bx	A3202	Ia	0.058	0.069
1997Q	A3562	IIP?	0.040	0.050
1997bz	A1238	Ia	0.030	0.072
1997cm	A3528	II?	0.071	0.053
1997cp	A3806	Ia?	0.160	0.076
1997cr	A3744	II	0.077	0.038
1997cv	A3565	II?	0.024	0.012
1997cz	A3565	nIa?	0.048	0.012
1997fd	A3158	?	0.190	0.059
1998P	A3566	nIa?	0.097	0.050
1998bq	A2029	nIa?	0.095	0.077
1998cq	A2819	Ia	0.150	0.075
1998do	A168	?	0.092	0.045
1998dv	A3266	?	0.155	0.059
1998dz	A3122	Ia	0.091	0.064
1998el	A3122	?	0.10	0.064
1998bs	A3558	?	??	0.048
1998bt	A1736	II?	??	0.046
1998dy	A3266	?	??	0.059
1998fb	A3128	?	??	0.060

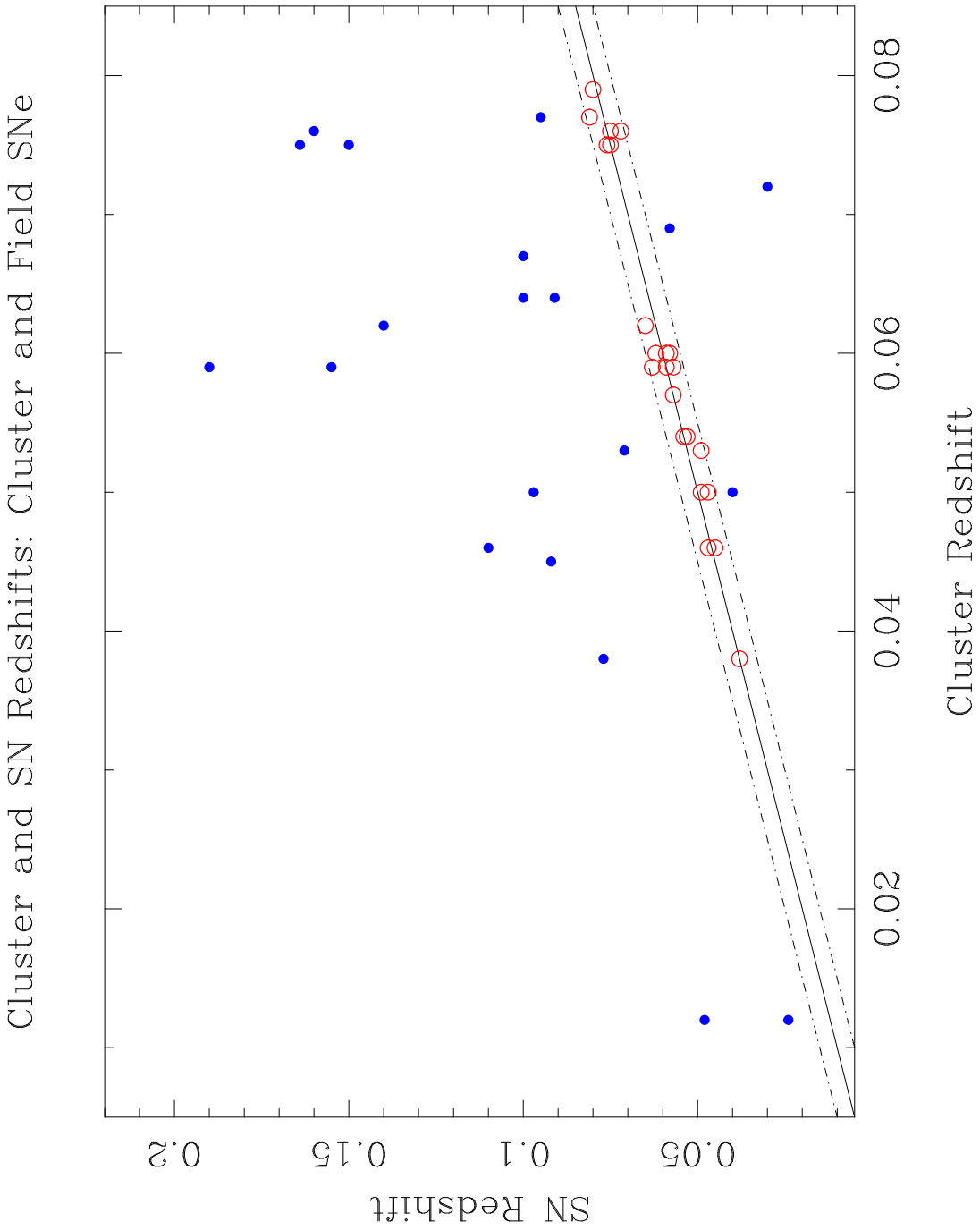

Figure 2.1: SN redshifts plotted as a function of their clusters' redshifts. Field (filled symbols) and cluster (open symbols) SNe are easily distinguished. The dashed lines mark the ± 0.005 redshift range used to discriminate between the two subsets of SNe.

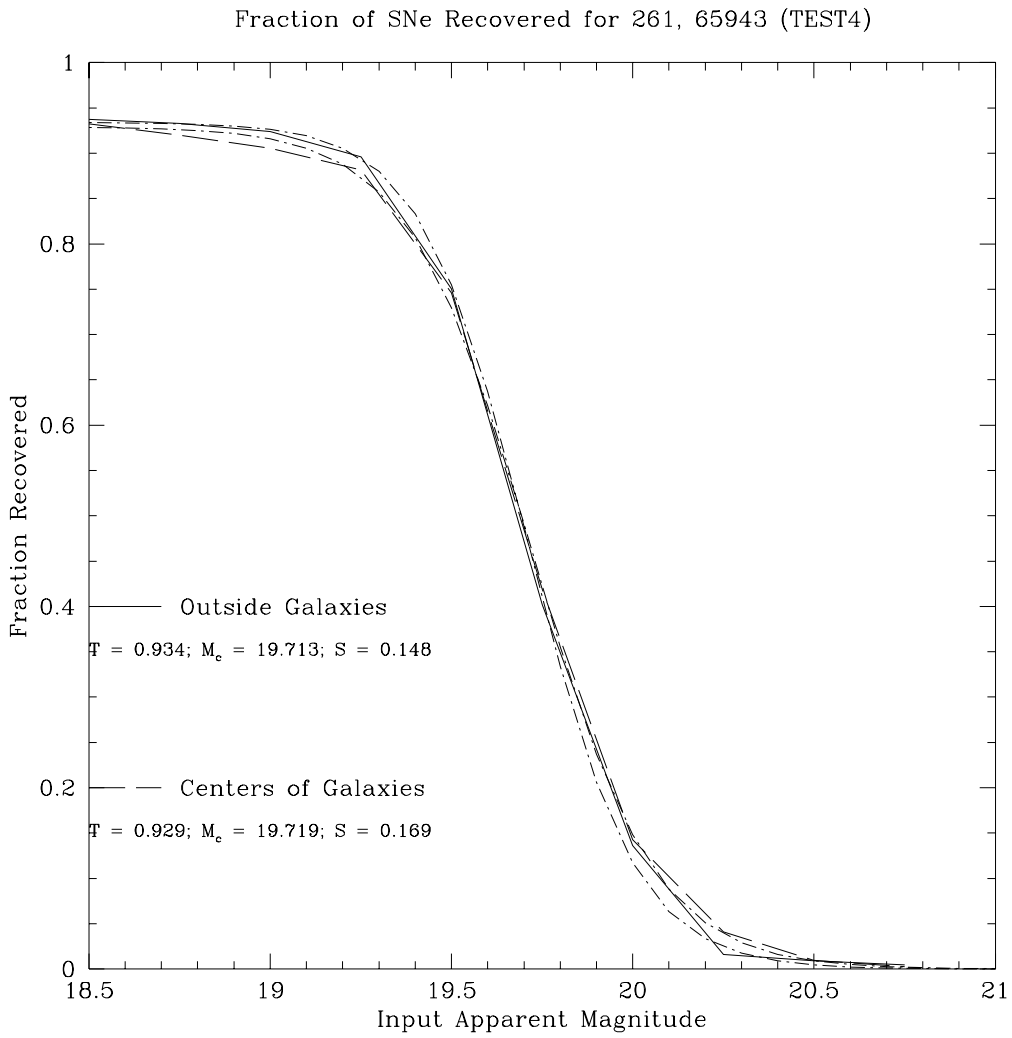

Figure 2.2: A SN detection efficiency curve for a typical MSACSS search observation. The observed curve for SNe on blank sky (solid line) and on the centers of bright galaxies (dashed curve) are shown with their parameterized fits (dot-dashed curves).

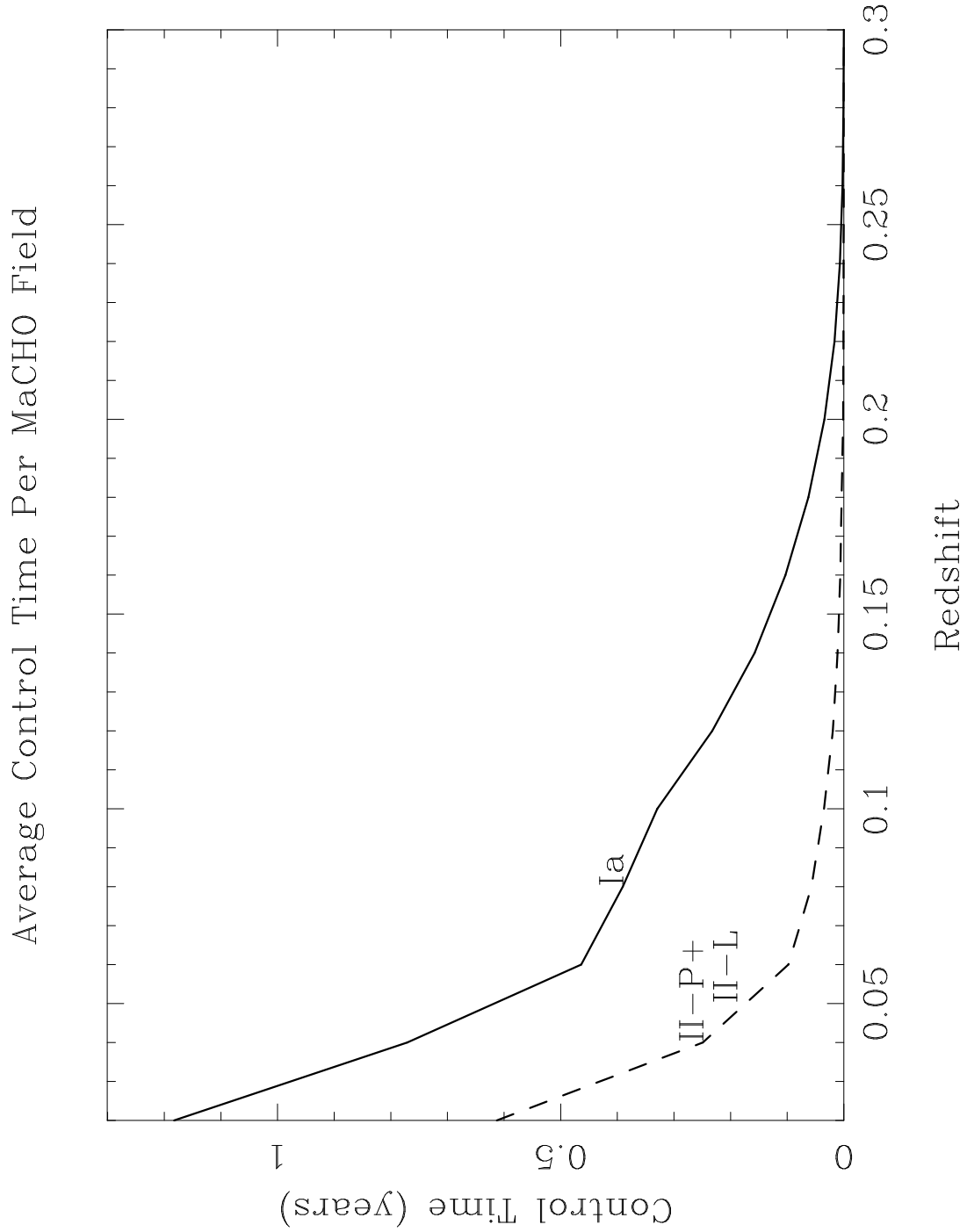

Figure 2.3: Integrated average control time per field of the MSACSS, as a function of redshift. Shown are total control times for SNe Ia (solid curve) and for SNe II-P + II-L added together in the ratio 5:1.

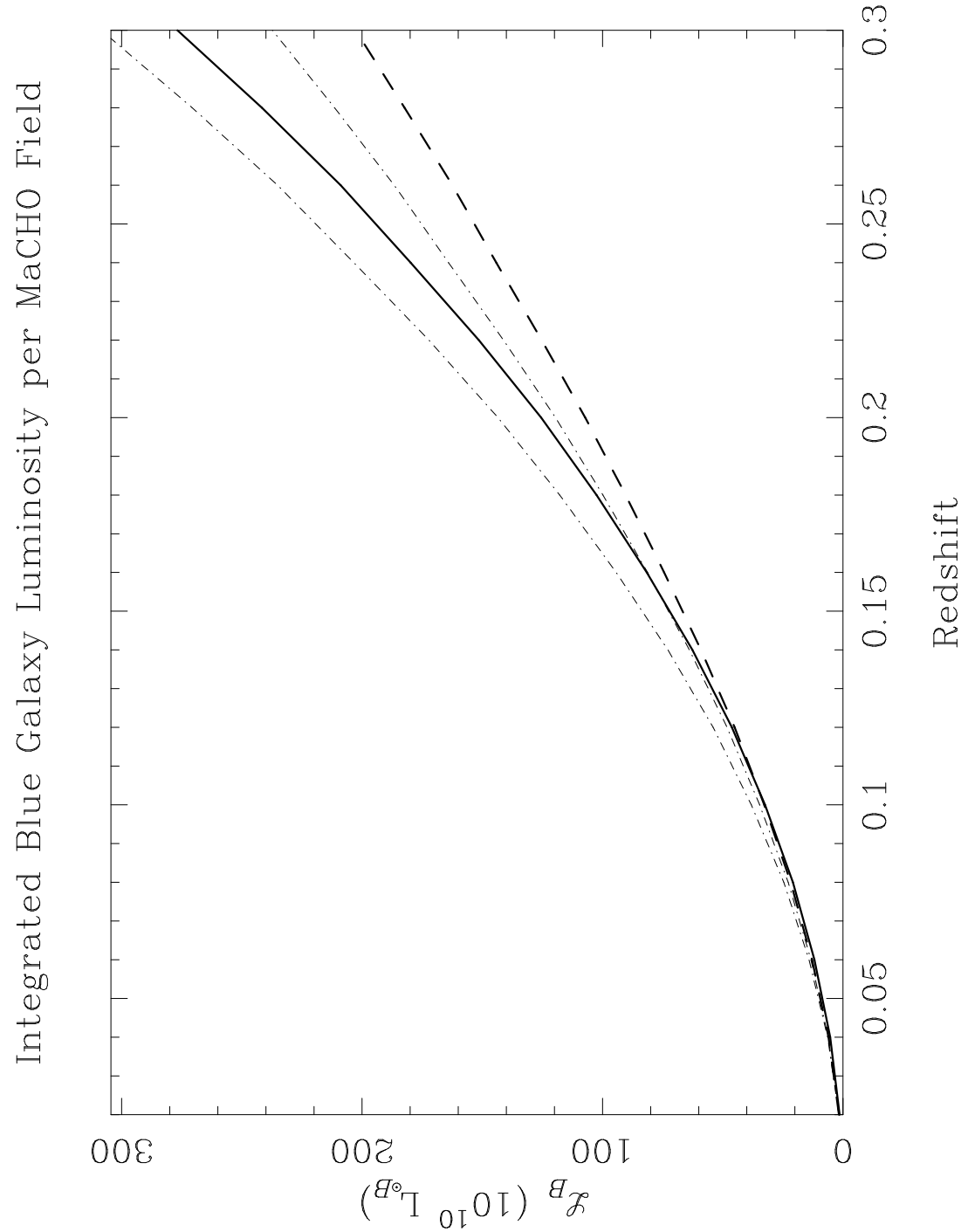

Figure 2.4: The total blue galaxy luminosity per MaCHO field per redshift bin of 0.02 (solid line). Also shown are the $\pm 1\sigma$ uncertainties in the luminosities (dotted lines) as well as the values if the luminosity density did not increase with redshift ($\propto$ volume; dashed line).

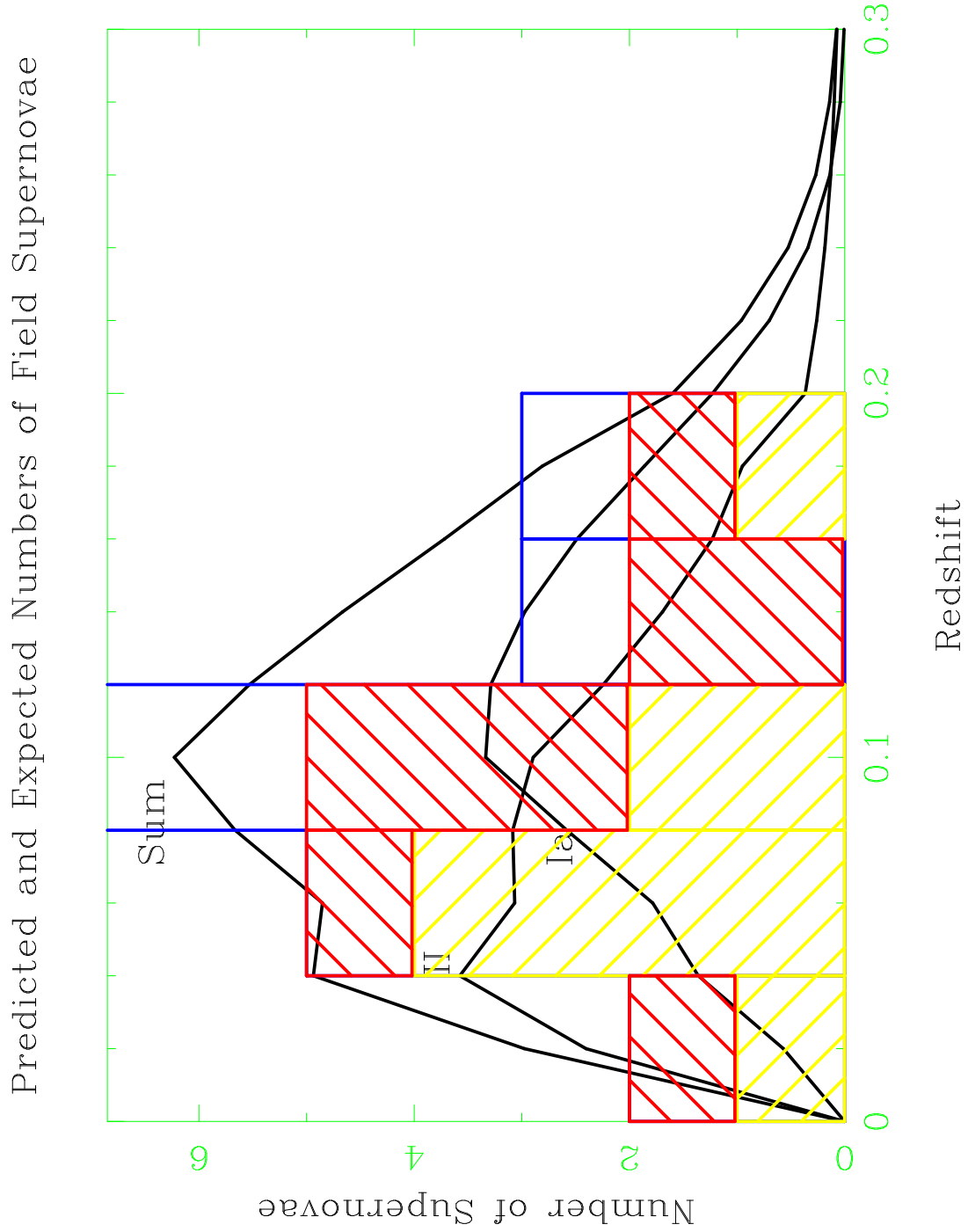

Figure 2.5: The expected and observed numbers of field SNe as a function of redshift, calculated for a SN rate of 0.164 (Ia) and 0.997 (II) SNu. Also shown is the observed distribution, with SNe Ia in red, SNe II in yellow, and unclassified SNe in blue.

Table 2.2: Field SN numbers, before and after assignment of SN type: observed, expected (with redshifts) and expected (total, including those without redshifts).

SN Type	$N_{\rm obs}$	$N_{{\rm exp},z}$	$N_{\rm exp,tot}$
Ia	8	10.59	12.06
II	8	9.41	9.84
Total	16	20.00	21.90

Table 2.3: Statistical uncertainties in the field SN rates: $\sqrt{N}$ statistical uncertainty, uncertainty due to possible mis-classification of SNe, and total uncertainty, in SNu.

SN Type	$\sigma_{\rm stat}$	$\sigma'_{\rm stat}$	$\sigma_{\rm tot}$
Ia	0.045	0.036	0.058
II	0.39	0.37	0.54

Table 2.4: Systematic uncertainty in field SN rates: parameters contributing to the uncertainty, the values used to compute the rates, ranges in those parameters, and resulting ranges in SN rates (SNu). The total systematic error is the quadratic sum of all listed contributions except for those marked by an (*).

Parameter	Value	+ limit	- limit	Ia Uncert.		II Uncert.	
H_0 (km sec^{-1} Mpc^{-1})(*)	65	+10	-10	+0.046	-0.040	+0.296	-0.254
Ω_M, Ω_Λ(*)	0.3, 0.7	1.0, 0.0	–	+0.000	-0.021	+0.000	-0.090
Ω_M, Ω_Λ(*)	0.3, 0.7	0.3, 0.0	–	+0.000	-0.014	+0.000	-0.058
$\mathcal{L}_{B,\mathrm{local}}(h \times 10^8 L_\odot Mpc^{-3})$	2.00	+0.2	-0.2	+0.023	-0.006	+0.134	-0.054
α_L	2.27	+0.5	-0.5	+0.015	-0.001	+0.066	-0.005
$\overline{M}_{B,\mathrm{Ia}}$ (mag)	-19.33	+0.2	-0.2	+0.033	-0.027	+0.013	-0.009
$\overline{\sigma}_{\Delta,\mathrm{Ia}}$ (mag)	0.41	+0.05	-0.05	+0.006	-0.000	+0.000	-0.000
Gaussian $F_{\mathrm{Ia}}(E_{B-V})$ w/ $\sigma = 0.3$ mag				+0.000	-0.040	+0.000	-0.010
Gaussian $F_{\mathrm{Ia}}(E_{B-V})$ w/ $\sigma = 0.5$ mag(*)				+0.000	-0.018	+0.000	-0.003
No SN Ia extinction (delta-func. at $E_{BV} = 0$)(*)				+0.000	-0.057	+0.000	-0.016
$\overline{M}_{B,\mathrm{II-P}}$; $\overline{M}_{B,\mathrm{II-L}}$ (mag)	-17.0, -18.0	+0.5	-0.5	+0.002	-0.005	+0.599	-0.339
$\overline{\sigma}_{\Delta,\mathrm{II}}$ (mag)	1.75	+0.5	-0.5	+0.012	-0.003	+0.956	-0.196
$\overline{A_{V,\mathrm{II}}}$ (mag)	1.0	+0.5	-0.5	+0.002	-0.002	+0.378	-0.212
$\sigma_{A_V,\mathrm{II}}$ (mag)	1.0	+0.5	-0.5	+0.001	-0.000	+0.134	-0.012
$\overline{A_{V,\mathrm{II}}} = 0.6$ mag; $\sigma_{A_V,\mathrm{II}} = 0.75$ mag(*)				+0.000	-0.002	+0.000	-0.249
m_{lim} (systematic; mag)	–	+0.1	-0.1	+0.017	-0.015	+0.100	-0.088
m_{lim} (statistical; mag)	–	+0.3	-0.3	+0.000	-0.001	+0.002	-0.001
m_{ceil} (mag)	20.5	21.0	–	+0.000	-0.021	+0.000	-0.063
calibration error (mag)	–	+0.1	-0.1	+0.014	-0.004	+0.090	-0.090
area searched (% of image)	95%	+3%	-3%	+0.001	-0.002	+0.005	-0.007
Total				+0.050	-0.056	+1.214	-0.471

Chapter 3

THE RATE OF SUPERNOVAE IN CLUSTER GALAXIES FROM THE MOUNT STROMLO ABELL CLUSTER SUPERNOVA SEARCH

3.1 Introduction

The methods used to calculate the SN rates in rich galaxy clusters from the SN sample found by the Mount Stromlo Abell Cluster Supernova Search are very similar to the ones we used in Chapter 2 to estimate the field galaxy SN rate. The resulting rates will not be subject to uncertainties as large as those derived in field galaxies, simply because our cluster sample was volume-limited, *i.e.* $z \leq 0.08$. With our faint limiting magnitudes of ~ 20.5, the faint end of the SN luminosity function in the surveyed clusters was much better sampled than in the field, where SNe were detected out to $z \simeq 0.2$.

We describe the cluster SN sample in Section 3.2, and briefly summarize the calculation of the total control time in Section 3.3. The primary difference between the computation of the cluster SN rates and that of the field SN rates involves the computation of the control galaxy luminosity. This is described in Section 3.4. In section 3.5, we discuss how the control times are integrated and combined with the galaxy luminosity estimate to derive supernova rates. We will summarize the uncertainties and possible sources of systematic error in the derived SN rates in section 3.6, and compare these results to those of Chapter 2 in section 3.7. Finally, we investigate the rates of "unusual" core-collapse SNe like the under-luminous SN 1987A and extremely over-luminous SN 1997cy in section 3.8.

3.2 The Sample of Cluster Supernovae

Analogous to the criteria used to define the field SN sample (Chapter 2, Equation 2.2), the cluster SN sample is chosen such that

$$|cz_{\rm SN} - cz_{\rm cluster}| \leq 2\overline{\sigma}_v, \tag{3.1}$$

with $\overline{\sigma}_v = 800\,{\rm km\,sec}^{-1}$ again being used as the typical cluster velocity dispersion. The 22 SNe that fit these criteria are listed in Table 3.1. Moreover there are four SNe whose redshifts were not measured (and are listed at the bottom of Table 3.1); we will make the reasonable assumption that the same fraction of SNe with measured redshifts which are cluster SNe (out of a total of 46, listed in Chapter 1, Table 1.6) applies to these four. Therefore the total number of cluster SNe used in this chapter is ~ 24.

3.3 The Total Control Time

The computation of the total control time for each field progresses along the same lines as those described in Chapter 2 , section 2.4. The only difference is that for each field the control time for detecting cluster SNe need not be computed over a range of redshifts; the redshift of the cluster is known. However, the cluster sample as a whole does cover a range of redshifts. In this way, we can compute an average control time per redshift bin. This is shown in figure 3.1, which is analogous to the figure in Chapter 2. Included are errorbars showing the statistical uncertainties based on the number of clusters available per redshift bin. It is evident that even over this small range of redshift, the control times decrease more quickly for the faint, heavily extinguished type II SNe. However, the relative flatness of the control time curve for SNe Ia suggests that we are sampling a large portion of the SN Ia luminosity function within our cluster sample. This was one of the primary goals incorporated into the design of the search from its inception. The two curves might

seem surprisingly similar, despite the great disparity in SN populations. This is largely due to the large dispersion (1 mag) incorporated into the core-collapse SN luminosity function (Chapter 2 ,section 2.4.4), enabling a small number of rather bright SNe II to increase the control times at greater redshift.

3.4 The Integrated Cluster Luminosities

The control luminosity must be computed from our search images, since there have been few published wide-field observations of most of these southern clusters. We therefore performed photometry on each of the template images of our fields, in both V_M and R_M. These non-standard filters present a problem since the galaxy magnitudes must be converted to standard B and R to compare to field SN rate measurements (in SNu and SNu_R).

3.4.1 Galaxy Photometry

The galaxy photometry was conducted using the SourceExtractor artificial neural network and object classifying software developed by Bertin & Arnouts 1996. The poor-seeing images of the MSSSO 1.5m made it somewhat difficult to choose fail-proof parameters for the software to use in discriminating stars from galaxies, and it is possible that some very compact, unresolved galaxies were (in the $FWHM \gtrsim 2''$ images) erroneously classified as stars. Certain parameters that were required by SourceExtractor (such as the PSF $FWHM$) were measured for each image individually, on bright stars using the DoPhot stellar photometry package (Schechter, Mateo, & Saha 1993). The other parameters necessary for star-galaxy discrimination were selected for all images by repeatedly running SourceExtractor on several images of varying quality and checking the results by eye until the detections and classifications performed by the software were deemed to be as good as (or better than) could be done interactively. The default (PSF) convolution kernel was used

for object detection; this is the ideal filter for detecting all but the lowest surface-brightness galaxies (Irwin 1985). In the end, detected objects were chosen to be those whose which contained $1.1(FWHM)^2$ (≈ 35 in $2''$ seeing) pixels that were at least 1.2σ above the background. It was found that this resulted in the detection of essentially all of the objects visible by eye with very few apparently spurious detections. Objects were classified as galaxies if they had stellarity index < 0.6 (Bertin & Arnouts 1996), $FWHM$ greater than the seeing $FWHM$ or smaller than one-third the size of the seeing $FWHM$ (as measured by SourceExtractor, this was required for those that were too faint for an accurate $FWHM$ to be measured). The final magnitude reported by SourceExtractor (adaptive aperture or corrected isophotal; see Bertin & Arnouts 1996) was used.

The galaxy photometry was brought to a photometric zero-point just as the limiting magnitudes of SNe detections were photometrically calibrated, as described in Chapter 2. The uncertainty in each field's individual calibration was ~ 0.05 mag, and there is likely to be a systematic offset of ~ 0.1 mag due to the conversion of standard $BVRI$ to V_M and R_M, for the secondary standards, that is necessary to perform the calibration.

Finally, the galaxy magnitudes were corrected for foreground extinction and reddening, which was computed for each field from the E_{B-V} maps of Schlegel, Finkbeiner, & Davis 1998. The median size of the reddening was 0.031 ± 0.024 in E_{B-V}, and was converted to magnitudes of extinction via the standard $R_V = 3.1$ extinction curve (Schlegel, Finkbeiner, & Davis 1998), where the extinction coefficients R_V and R_R were used for V_M and R_M, respectively. The expected uncertainty in this correction to the galaxy magnitudes is a random contribution of ~ 0.05 mag. The galactic dust also selectively extinguishes low surface-brightness galaxies the most where isophotal magnitudes are used (Gaidos 1997); SourceExtractor uses isophotal magnitudes for only $\sim 20\%$ of the detected objects (Bertin & Arnouts 1996). We do not include this systematic effect in calculating the total cluster magnitudes since

it is not likely to affect the total cluster magnitudes significantly (see Gaidos 1997, Figure 6).

3.4.2 Fitting the Galaxy Counts

In the most straightforward method, the total luminosity of a cluster cannot be measured until all of the cluster galaxies have been identified. Since this is an impractical task to perform by obtaining redshifts of all bright galaxies in the field, the only reasonable solution is to do a statistical subtraction of the background galaxies in the field. In this way, individual cluster galaxies are *not* identified, rather a statistical description of the cluster galaxy population is obtained. Several methods of background subtraction are often used to measure, for example, cluster galaxy luminosity functions or cluster profiles. One of these is to obtain deep images of blank (*i.e.* non-cluster) fields, using the same camera/telescope as the observations of the cluster fields, and then subtract the galaxy counts. The primary drawback of this technique is that the density of field galaxies fluctuates by a significant amount from field to field, particularly surrounding rich clusters which our search specifically targeted, and using an average of field galaxy observations could result in an over- or under-subtraction of the field contribution to the field+cluster counts. The second (preferred) technique is to do a subtraction of counts taken from the periphery of wide-field images of the cluster fields, with the assumption that at a large enough radius one is only seeing field galaxies. The obvious disadvantage to this method is that unless the images are extremely wide-field and the clusters distant ($z \gtrsim 0.1$) one cannot reasonably expect this assumption to be true. Our cluster images, with many at $z \lesssim 0.04$, were not suitable for this method of background galaxy subtraction.

The galaxy counts (number per apparent magnitude bin) of a typical search field of the MSACSS, measured as described in Section 3.4.1 (in this case for Abell 3266), are shown in Figure 3.2, for both the red and blue images (points). The typical characteristic of these counts are a "hump" near $V_M \simeq R_M \simeq 16$ from

the cluster galaxies, which then fades into the characteristic power-law increase at fainter magnitudes as the galaxies in the background field begin to outnumber those in the cluster. Many researchers have shown (Metcalfe *et al.* 1991, Gaidos 1997 and references therein) that the field galaxy apparent magnitude counts are well-described by a power-law at brighter magnitudes that is steeper as one goes towards shorter wavelengths. On the other hand, motivated by the Press-Schechter formalism (Press & Schechter 1974), there is much observational (Gaidos 1997, Lumsden *et al.* 1997, Valotto *et al.* 1997, Garilli, Maccagni, & Andreon 1999 and references therein) work showing that cluster galaxy counts are well-fit by a Schechter (Schechter 1976) luminosity distribution which is fainter and increases more steeply (at the faint end) in blue passbands than in the red.

Given these simple analytical distribution functions for field and cluster galaxy counts, we have chosen a third method to statistically determine the characteristics of the cluster population: to fit a power-law plus Schechter function (*i.e.* a *field* plus *cluster* distribution) to the galaxy counts in each field, individually,

$$N_{\rm gal}(m) = \left[n \times 10^{\gamma(m-16)}\right] + \left[\phi^* 10^{-0.4(\alpha+1)m} \times \exp\left(-10^{0.4(m^*-m)}\right)\right], \qquad (3.2)$$

where n and ϕ^* are the field and cluster normalizations, respectively, γ defines the power-law slope of the field counts, and m^* and α describe the overall shape of the cluster luminosity distribution (where m^* is the apparent magnitude of the "characteristic" Schechter function absolute magnitude, M^*).

Since the cluster counts are often dominated by the noise in the background counts, it is not feasible to simultaneously fit for all five parameters in equation 3.2 in each field, as oftentimes the fit does not converge. Furthermore, we cannot just add the counts from all fields together to derive an average cluster luminosity, since each cluster has a different SN detection control time, which must then be multiplied by its own individual control luminosity before they are summed up to compute the

total SN rate. We therefore choose, for each of the two passbands, fiducial values for the *shape* parameters in equation 3.2 (γ, M^*, and α) and then determined the best-fit values (via least-χ^2) for the normalization parameters, n and ϕ^*, in each field.

The slope of the field galaxy counts depends strongly on the passband in use and the apparent magnitude range examined, with authors such as Metcalfe *et al.* 1991 obtaining slopes of 0.494 ± 0.013 ($B_{ccd} > 20.5$) and 0.373 ± 0.10 ($R_{ccd} > 20$), while Gaidos 1997 counted 0.505 ± 0.014 for $17 < R < 21$. Values for the Schechter parameters seen in rich clusters have also varied from study to study; overall it seems that $M^* \simeq (-20 \pm 0.5) + 5 \log h$ is reasonable for R, while M^* is ~ 1 mag fainter in B. Meanwhile, α appears to be near $\sim -1.10 \pm 0.2$ in R and slightly steeper at $\sim -1.20 \pm 0.2$ in B (Gaidos 1997, Lumsden *et al.* 1997, Valotto *et al.* 1997, Garilli, Maccagni, & Andreon 1999).

Prior to performing the least-χ^2 fitting, the counts were truncated at 0.25 mag brighter than the magnitude where the distribution was observed to peak due to the sharp decrease in the detection efficiency for fainter galaxies. This cut was typically made near $V_M \simeq R_M \simeq 20.5$ but varied by ± 1 mag or so depending on the seeing FWHM of the observation.

The shape parameters which we used were chosen iteratively, by fitting each of the shape parameters one at a time (plus the two normalization parameters) for all fields, and then taking its median value using only those fields whose fits converged to reasonable values and had low resulting χ^2 ($\lesssim 2$). Each time a different shape parameter was fit, the other two would be kept constant at the best value that was determined from the last fit. The γ–M^*–α fits would be repeated until the parameters appeared to settle to consistent values. All parameters were most easily constrained for the fits in fields at low redshift, *i.e.* $z \lesssim 0.04$, where a larger part of the cluster luminosity function could be sampled above the detection limits $m \lesssim 20.5$ (to constrain M^* and α), and the background counts could become sufficiently dominant

at fainter magnitudes (to constrain γ) but brighter than the cutoff. α was the least readily constrained, as it was strongly correlated with γ; however the fits were consistent with the values found by previous researchers (see above), and showed that α_{V_M} was consistently steeper than α_{R_M} by about 0.1. The chosen values for these parameters for both MaCHO passbands are listed in Table 3.2. The uncertainties are taken to be the dispersions in the parameters across all fields for which the fits appeared to be well-constrained.

Figure 3.2 shows, in the solid and dashed lines, the typical results of fitting n and ϕ^* in equation 3.2 to a field's galaxy counts, while constraining γ, M^* and α to the values listed in Table 3.2. The inset shows the residuals resulting in subtracting off the parameterized fit to the field counts, overlaid with the shape of the Schechter function fit, showing that the fits do appear to be characterizing the large-scale shape of the cluster counts in a reasonable manner.

3.4.3 The Integrated Cluster Luminosity

The total cluster luminosities were calculated via a simple integration of the best-fit Schechter function determined in Section 3.4.2. Fortunately, the integral of the Schechter function, $L = \phi^* L^* \Gamma(\alpha + 2)$, is rather insensitive to small uncertainties in the Schechter parameters since they are inversely correlated and compensate for each other in their overall effect on the integral.

The integrated cluster luminosities, computed in the non-standard V_M and R_M must be converted to B and R luminosities on an absolute scale. We chose to do this by synthesizing the colors of a "typical" cluster galaxy and offsetting the derived cluster luminosities so that their colors match. Our synthetic photometry is computed for a "composite" galaxy spectrum derived from the spectrophotometry of Kennicutt 1992, extrapolated to the red via a power-law fit, similar to the methods of Fukugita, Shimasaku, & Ichikawa 1995. The composite was an average of spectra of various galaxy types from E through Sc, weighted accordingly so that the fractional

contributions to the total luminosity of the galaxy were 21%, 44%, and 35% for E, S0 and Sa/b/c/Im galaxies, respectively, to match the observed composition of rich clusters (Dressler 1980, Schechter & Dressler 1987), and so its $B-V$ color matched the median colors from observations of cluster galaxies out to large radius . Our synthetic colors derived from the Kennicutt 1992 SEDs agreed with the average observed colors of galaxies of similar type (de Vaucouleurs *et al.* 1991) and with those synthesized by Fukugita, Shimasaku, & Ichikawa 1995, to better than 0.05 mag. Figure 3.3 shows the measured $V_M - R_M$ colors of the clusters in our sample as a function of redshift. Also shown for comparison are the synthetic $V_M - R_M$ colors of our composite cluster galaxy spectrum, redshifted by the appropriate amount and reddened with a color excess of $E_{B-V} = 0.03$. The match lends support to the claim that our cluster luminosity calculations are indeed reasonable, to within ± 0.1 mag with a small possible systematic uncertainty.

The V_M and R_M cluster luminosities are converted to standard solar luminosities using $M_{B_\odot} = 5.48$, $(B-V)_\odot = 0.65$ and $(V-R)_\odot = 0.51$, and the synthetic colors of the composite cluster spectrum,

$$V = V_M + (V - V_M)_{\rm syn}, \tag{3.3}$$

$$R = R_M + (R - R_M)_{\rm syn}, \tag{3.4}$$

$$B = V_M + (V - V_M)_{\rm syn} + (B - V)_{\rm syn}. \tag{3.5}$$

where the composite spectrum was redshifted and reddened by the appropriate amount for each cluster. The resulting color-color diagram for the clusters is shown in Figure 3.4, along with the range in synthetic colors computed for the cluster composite over $0 < z < 0.08$. It is apparent that the $V-R$ colors are ~ 0.1 mag too blue, which is not unexpected due to the extrapolations that were required to compute the synthetic colors at wavelengths $\lambda > 7000$Å. All in all, we believe that ~ 0.1 mag is a reasonable estimate of the systematic uncertainty in the average conversion of

the cluster luminosities to standard passbands.

To provide further evidence that we have measured accurate total cluster luminosities, we have performed the following tests. While no one test is convincing by itself, the charts plotted in Figure 3.5, along with those of the derived and synthesized cluster colors (above) should paint a compelling picture.

The original Abell, Corwin and Olowin (Abell, Corwin, & Olowin 1989) catalogue of rich clusters from which the MSACSS derived its cluster sample contains a very uncertain distance-independent measure of each cluster's galaxy counts. This parameter, N_{gal}, is the total number of galaxies counted (by eye in POSS plates) within one Abell radius ($\sim$ 1500 kpc; Abell 1958) that have brightnesses between m_3 and $m_3 + 2$, where m_3 is the apparent magnitude of the third-brightest cluster galaxy (and is itself uncertain by nearly ± 1 mag). This number should correlate with the total measured cluster luminosity. Figure 3.5a shows a coarsely binned plot of N_{gal} compared to the blue cluster luminosities, L_B, derived for our cluster sample. While there is an extremely large dispersion in N_{gal} values at a given L_B, there is evidence for a correlation between the two cluster richness measurements, lending support that we have measured accurate cluster luminosities.

Figure 3.5b shows a comparison of the measured blue and red cluster luminosities, two parameters which are derived from completely independent observations and measurements of the same cluster. There is a strong correlation between L_B and L_R with an unexpectedly small dispersion. This is the best evidence that we are truly measuring cluster galaxy counts above those of the background field counts and that the counts-fitting method we employ is doing a reasonable job of counting them. The correlation seen in Figure 3.5b, however, could reflect a correlation between n and ϕ_* resulting from the fitting as there will certainly be a correlation between the n values seen in the R_M and V_M images. Figure 3.5c reveals that there does not appear to be any such correlation between n and ϕ_*, and that the normalization in the background counts is not affecting the normalization measured in the cluster

counts. Finally, we would expect that if we are indeed counting up the luminosities of cluster galaxies in our analysis, then nearby clusters would have a smaller measured total luminosity because our fixed image size covers a smaller fraction of the total projected area of the cluster. Figure 3.5d shows the results of this effect. The solid vertical line shows the redshift beyond which one Abell radius lies completely within the 1/2 deg^2 field of the MaCHO camera. The dashed line shows the relative amount by which one would expect the observed cluster luminosity to increase if a cluster had a uniform projected density of galaxies within one Abell radius. The overall picture is clear: we are measuring the total cluster luminosity, which increases with distance as more cluster galaxies are projected within the 1/2 deg^2 of the MaCHO focal plane.

As a final comparison, we compare in Figure 3.6 the binned set of X-ray luminosities (0.1–2.4 keV) of those clusters satisfying the X-ray selection criteria of Ebeling *et al.* 1996 (there are only 39) with the derived B-band luminosities. There is a clear correlation. Moreover, the histogram (dotted line) reveals the number of clusters in the MSACSS sample which fail to reach the flux limits of the X-ray sample; those at faint optical luminosities clearly dominate this sample, as one would expect.

The final integrated BVR "control luminosity" used to compute the supernova rates is shown in Figure 3.7, in analogue to Figure 2.4 for the field SN rates. Also shown for comparison is the total luminosity contributed by the field galaxies (equation 2.10, Chapter 2). The cluster galaxies clearly dominate the sample at these redshifts and it is reasonable to assume that each SN with a recession velocity close to that of the cluster in its field has indeed occurred within the cluster.

For completeness, we list the total derived cluster control luminosities and their resulting colors in table 3.3, for our entire sample. Those values with a "–" indicate that the fit to the cluster's galaxy counts (eq. 3.2) indicated a negative (unrealistic) galaxy luminosity for that passband.

3.5 The Cluster Supernova Rates

The redshift distribution of detected cluster supernovae can be computed much in the same way as for the field SN rates (eq. 2.11, 2). Here, the only difference is that each field represents a discrete point in redshift space at the redshift of its target cluster, rather than a continuous distribution as was the case for the field measurements. Figure 3.8 shows the cluster SN distribution expected from our search (solid lines) compared to the observed distribution (histogram; SNe Ia are red, SNe II are yellow, unclassified SNe are blue). The specific parameters describing the SN population distributions are the same as those used to compute the field SN rates (Chapter 2). The match between the expected and observed distributions is notable. A Komolgorov-Smirnov test suggests that it is possible to reject the hypothesis that the observed sample and the predicted distribution are not the same with only a 35% probability. The primary reason for the fine match is probably that the uncertainty in the detection limits play a small role here for this volume-limited sample. This makes the predicted distribution less sensitive to uncertainties in the parameters describing the characteristics of the SN populations.

The SN rate is determined just the same way as are the field rates (Chapter 2, equation 2.12). Following the methodology used to compute the field rates, unclassified SNe are probabilistically "assigned" a classification based on the relative values of the predicted SN counts at the redshift of each unclassified SN. Furthermore, a fraction of the SNe with no redshift or classification are given cluster SN status and contribute to the rates in a similar manner. Following Table 2.2 we list the numbers of SNe predicted both before and after "reassignment" in Table 3.5.

The derived rates are 0.180 $(H_0/65)^2$ SNu and 0.124 $(H_0/65)^2$ SNu for SNe Ia and II respectively. These values were used to normalize the predicted redshift distribution of SNe in Figure 2.5.

We also computed the cluster SN rates in units of SNu_R. We find 0.164 and

0.115 SNu_R for SNe Ia and core-collapse SNe, respectively. The uncertainties in these values will be very close to those derived for the rates computed in SNu.

3.6 Uncertainties and Systematic Errors

The statistical uncertainties are computed just as in Chapter 2, Section 2.7, and are listed in Table 3.6 (where σ_{stat} is simply the $\sqrt{N}$ statistical uncertainty, σ'_{stat} is the error estimated due to the forced classification of certain unclassified SNe based on the predicted SN redshift distribution, and σ_{tot} is the quadratic sum of these two uncertainties.

The cluster SN rates are subject to most of the same systematic uncertainties as the field SN rates (Section 2.7, Chapter 2). The only difference is that here the uncertainties in the total control luminosity reflect uncertainties in the method used to extract the cluster luminosity function, as well as uncertainties in the luminosity function parameters. We list the various parameters which contribute in a systematic manner to the uncertainty in the cluster rates in table 3.7, column (1). Column (2) lists the values which were used for the rates derived in this thesis, and columns (3) and (4) show the estimated $\sim$ 1-σ uncertainties in these parameters which contribute to an increase in the upper and lower error-bars of the SN rates, respectively. Most of these parameters and their uncertainties are the same as those used to derive the systematic uncertainty in the field SN rates (table 2.4). Finally, columns (5-6) and (7-8) list the individual contributions to the uncertainty of the upper- and lower-limits of the systematic errors for type Ia and type II SN rates, respectively.

The final cluster SN rates are therefore $(0.180^{+0.054\ +0.046}_{-0.054\ -0.058})\ \ (H_0/65)^2$ SNu for SNe Ia and $(0.124^{+0.076\ +0.085}_{-0.076\ -0.052})\ \ (H_0/65)^2$ SNu, for core-collapse SNe.

3.7 Discussion

Whereas the SN rates in galaxy clusters have not previously been measured, Cappellaro *et al.* 1997, Cappellaro, Evans, & Turatto 1999) have measured SN rates (in SNu) over a wide range of galaxy types. It seems reasonable that we can then take an average of the rates in Table 4 of Cappellaro, Evans, & Turatto 1999, weighted by galaxy type using the same fractional contributions as those which were used to compute the cluster colors (3.4.3). This enables us to test whether the SN rates are dependent on host galaxy type alone, or whether the galaxy environment and past interactions which the host galaxy has experienced may play an additional role. We derive a "cluster composite" SN Ia rate of (0.154 ± 0.054) $(H_0/65)^2$ SNu and a core-collapse SN (II+Ib/c) rate of (0.477 ± 0.258) $(H_0/65)^2$ SNu from Cappellaro, Evans, & Turatto 1999. Our cluster SN Ia rate, while somewhat higher, does not disagree, given the uncertainties. Our core-collapse rate appears smaller than the "cluster composite" core-collapse rate. Perhaps this may be attributed to an effect of the cluster environment on the star formation rates of the target galaxies, over and above the simple difference in ages between the mean stellar populations of cluster and field galaxies. Tidal interactions and stripping of the ISM in cluster galaxies are expected to suppress star-formation in these galaxies at current epochs, relative to their counterparts in the field. Of course the lower cluster SN-II rate may be explained by the large uncertainties in both calculations; achieving a more significant measurement of this difference, if it indeed exists, would be a very worthwhile endeavor.

We can more directly compare the cluster supernova rates derived here with the field SN rates computed from the same search using the same methodology, in Section 2.6. The ratio of field to cluster SN Ia rates, $r_{\rm Ia}$, may be compared to the ratio of field to cluster core-collapse SN rates, $r_{\rm II}$. In doing so, many of the systematic effects listed in Table 3.7 "cancel", resulting in lower overall uncertainties in the

ratios of SN rates between cluster and field. In particular, the systematics related to the cosmology, the magnitude limits of the search, and the parameters which describe the SN populations are all eliminated because the same such parameters were used to compute the cluster rates as were used to compute the field rates. All that remain are the systematic errors resulting from the estimation of the control luminosity. We find $r_{\rm Ia} = 0.906 \pm 0.43 \pm 0.28$ and $r_{\rm II} = 7.8 \pm 2.4 \pm 0.63$. The systematic errors have now decreased so that they are now smaller than the (still large) statistical uncertainty, revealing the power of doing a *comparison* of SN rates between galaxies with different average stellar populations. Not surprisingly the core-collapse SN rate appears to be substantially lower in clusters than in the field, while the SN Ia rate does not differ significantly between the two galaxy populations. One finds the same trend by comparing the average (field) SN rates with "cluster composite" rates derived above from Cappellaro, Evans, & Turatto 1999, although the "cluster composite" ratio $r_{\rm II}$ is closer to two than the ~ 8 we derive here. This could be a hint of a further depletion of core-collapse SN progenitors over that seen in field early-type galaxies, perhaps due to the effects of the surrounding cluster environment. The comparison also assumes that the type-II SN luminosity and extinction distributions are the same in both environments. Of course, the extinction distributions are not expected to be the same due to differences in large-scale dust distributions, however for type-II SNe, the small scale (star-formation region) dust distribution should dominate. Furthermore, if core-collapse SNe are intrinsically fainter in clusters, for example, that could explain this difference as well.

Another interesting diagnostic is a comparison of the SN rates in the bluer half of our cluster sample with those of the redder half. We divide our sample into two groups, those redder or bluer than the median color or $B-R = 1.253$, and divide the cluster SN sample similarly (with 12 SNe lying within the "blue" clusters and 10 in the "red" clusters). The advantage of this comparison is that *all* of the systematics cancel, although the statistical uncertainty increases by $\sim \sqrt{2}$. The computed rates

are (0.166 ± 0.065) and (0.159 ± 0.084) SNu for Ia and core collapse SNe in the bluer clusters and (0.209 ± 0.083) and (0.074 ± 0.097) SNu in the redder clusters. Ignoring the uncertainties, this result conforms to the already-known observation that core-collapse SNe follow the underlying blue galaxy luminosity more than SNe Ia which are presumably tied to an older stellar population, on average. It is particularly telling that only one of the five core-collapse SNe identified in clusters lie in the red cluster sample. The large uncertainties reduce the significance of this result, however; they cannot discern a significant difference in SN Ia rate between red and blue clusters, and there is a $\sim \frac{1}{2}$-σ difference between the SN II rates – a promising, if certainly not conclusive, result. Again, it would be extremely interesting to be able to do a similar comparison with a larger sample of cluster SNe. Differentiating further between stellar population effects and galaxy environment effects on the rate of SNe Ia would go a long way towards constraining the progenitors of these events.

In any effect, the overall picture is clear: the SN Ia rate is surprisingly constant going from field to cluster galaxies (per blue-band luminosity) whereas there is a large depletion of core-collapse SNe. This suggests that while the core-collapse progenitors have had sufficient time to evolve between the median field galaxy and cluster galaxy ages, the SN Ia progenitors have not, probably because they have longer lifetimes than the corresponding difference in stellar ages between field and cluster galaxies.

3.8 The Rate of "Unusual" SNe

There have been two distinct events which bracket the observed extremes in supernova luminosities. These are SN 1987A in the LMC, and SN 1997cy, detected during the course of the MSACSS (Germany *et al.* 1999).

The first of these is among the faintest known SNe II, reaching a peak brightness of $M_B \simeq -14.7$ ($\sim$ 2 mag brighter in R and I). Since it is also the nearest SN to have occurred in the past 200 years and itself was subject to 0.6 mags of fore-

ground extinction, it begs the question of whether events like SN 1987A are common throughout the universe and are simply not detected in SN surveys due to their extreme faintness. This question can be addressed by the MSACSS, which should have been able to detect such events out to $z \simeq 0.04$, where there is an enhancement of galaxy luminosity in clusters over that of the underlying field. There was one SN detected by the survey, SN 1998bt in the field surrounding Abell 1736, which had a broad light curve more similar to that of SN 1987A than to that of other known SN type. Unfortunately, this SN had no apparent host galaxy, and we were unable to get a spectrum of the object, so no redshift is available. However, if we assume that it lies at the redshift of Abell 1736 ($z = 0.046$), then the SN had a peak magnitude and light curve morphology much like that of SN 1987A (Figure 3.9). (This is not an unreasonable assumption given recent measurements of large populations of "intra-cluster" giants in rich galaxy clusters [Ferguson, Tanvir, & Von Hippel 1998].)

Following the control-times formulation of Section 2.4, we have computed the total control time for a SN-1987A light-curve (Menzies 1988), including K-corrections (Phillips *et al.* 1990), and multiplied these by the total underlying cluster control luminosity (Figure 3.7). Since we have absolutely no information on what a "1987A-type" SN population might look like, we have used δ-functions centered on the observed values for SN 1987A for the luminosity and extinction distributions when integrating the control times. Figure 3.10 shows that had we even detected *one* object that behaved like SN 1987A, this would have implied a rate for these objects of 0.43 SNu. In fact, the control time contributed by field galaxies nearly doubles the total control time of our search, and therefore decreases this number by 50%. We are able then to derive a rate of SN 1987A-like events (assuming SN 1998bt is the only such object detected during the MSACSS) of 0.2 ± 0.2 SNu. Regardless of how compelling a case may be made that SN 1998bt is indeed similar to SN 1987A, a firm upper (3-4σ) limit on the rate of SN 1987A-like events may be set at $\lesssim 0.8$ SNu, suggesting that they occur no more frequently than do "normal" core-collapse

SNe. This conclusion is consistent with, though not nearly as constraining as, the one reached by Cappellaro *et al.* 1993a, who place an upper limit on the relative SN 1987A-like to "normal" core-collapse (SN II+Ib/c) rate of < 0.07. However, the result is in stark contrast to the claims of Schmitz & Gaskel 1988 and others who suggest that faint SN 1987A-like events must be extremely frequent.

SN 1997cy was found (Germany *et al.* 1999) to have peaked at $M_B << -19.6$, and ~ 0.5 mag brighter in R. Its extreme photometric and spectroscopic properties coupled with its compelling association with gamma ray burst GRB970514 lends itself to the claim that it is an excellent candidate for the rare core-collapse of a star with mass $\gtrsim 50 M_\odot$ (Germany *et al.* 1999). We have computed the rate of objects identical in photometric characteristics to those observed in SN 1997cy, in the same manner as that computed for SN 1987A-like events described above (with the exception that color-corrections are not needed because we have direct V_M and R_M observations of this object, and K-corrections are not used). Because this SN is a cluster SN (by our criterion in Equation 3.1), it is natural to compute the rate using only the integrated cluster luminosities; doing this we derive a rate of $(4.7 \pm 4.7) \times 10^{-3}$ SNu, ignoring all systematic errors which are dwarfed by the statistical uncertainty in this case. Adding the field galaxy luminosity (eq. 2.10) and control times out to $z = 0.3$ (which we show in Figure 3.11) decreases the overall rate significantly to $r_{97\mathrm{cy}} = (1.7 \pm 1.7) \times 10^{-3}$ SNu. Again, these rates are based on the assumption that we have detected only one of this type of object; a more reasonable measurement is a 3–4-σ upper limit to their rate of $\sim 6.6 \times 10^{-3}$ SNu.

If this event is indeed indicative of the core collapse of a star with mass $\gtrsim 50 M_\odot$, then the ratio of this rate to that of "normal" core-collapse events should be equivalent to the relative number of stars within the hypothesized mass ranges that produce each of these events, namely

$$\frac{r_{97\mathrm{cy}}}{r_{\mathrm{cc}}} = \frac{\int_{M_{SN}}^{M_U} M^{-2.35} dM}{\int_{M_L}^{M_{SN}} M^{-2.35} dM}. \tag{3.6}$$

M_L and M_{SN} define the lower and upper ends to the range in stellar masses that terminate with "normal" core-collapse SNe ($\sim 12M_\odot$ and $\sim 50M_\odot$, respectively), and M_U is the upper theoretical mass limit for star formation (somewhere near $200M_\odot$ but equation 3.6 is rather insensitive to this value); $dN/dM \propto M^{-2.35}$ is the Salpeter stellar initial mass function. Using these mass limits in equation 3.6 results in a ratio of SN rates $r_{97\mathrm{cy}}/r_{\mathrm{cc}} \simeq 0.17$, which is significantly greater than the observed ratio of ~ 0.002 (upper limit of ~ 0.007). Reconciling this difference (a factor of nearly 20) would require either steepening the slope of the IMF to $\lesssim -4$ (an unrealistic slope), or alternatively increasing the mass cutoff M_{SN} to $\gtrsim 400M_\odot$. Barring any change to the stellar IMF at extremely high stellar masses (which is entirely plausible as well), this result would suggest that only the extremely massive stars with $M >> 200M_\odot$ undergo a massive explosion similar to that seen in SN 1997cy, or that only $\lesssim 5\%$ of the stars with $M \gtrsim 50M_\odot$ do so, perhaps as a result of neutron star or black-hole collisions, or that only a similar fraction of these massive explosions are seen, due to asymmetry in the explosion.

Table 3.1: Table of cluster supernovae discovered in the MSACSS, including the observed type and redshift, if available, and the redshift of its Abell cluster.

SN	Abell	Type	z	Cluster z
1996am	A3809	Ia	0.065	0.062
1996ao	A3128	Ia	0.058	0.060
1996ap	A3806	?	0.075	0.076
1997by	A1736	Ia	0.045	0.046
1997cl	A3577	II-n	0.047	0.050
1997cu	A3128	Ia	0.062	0.060
1997cy	A3266	II-pec	0.063	0.059
1997df	A3223	II?	0.059	0.060
1997dr	A3112	Ia?	0.075	0.075
1997fb	A3301	Ia	0.053	0.054
1997fc	A3301	Ia	0.054	0.054
1997fe	A3266	Ia?	0.059	0.059
1998O	A3566	II?	0.049	0.050
1998Z	A3341	Ia	0.038	0.038
1998br	A2029	Ia?	0.081	0.077
1998ch	A3559	II	0.047	0.046
1998cm	A1780	Ia	0.080	0.079
1998dp	A2401	?	0.057	0.057
1998du	A2819	?	0.076	0.075
1998dw	A151	Ia	0.049	0.053
1998ea	A3266	Ia	0.057	0.059
1998ez	A3188	?	0.072	0.076
1998bs	A3558	?	??	0.048
1998bt	A1736	II?	??	0.046
1998dy	A3266	?	??	0.059
1998fb	A3128	?	??	0.060

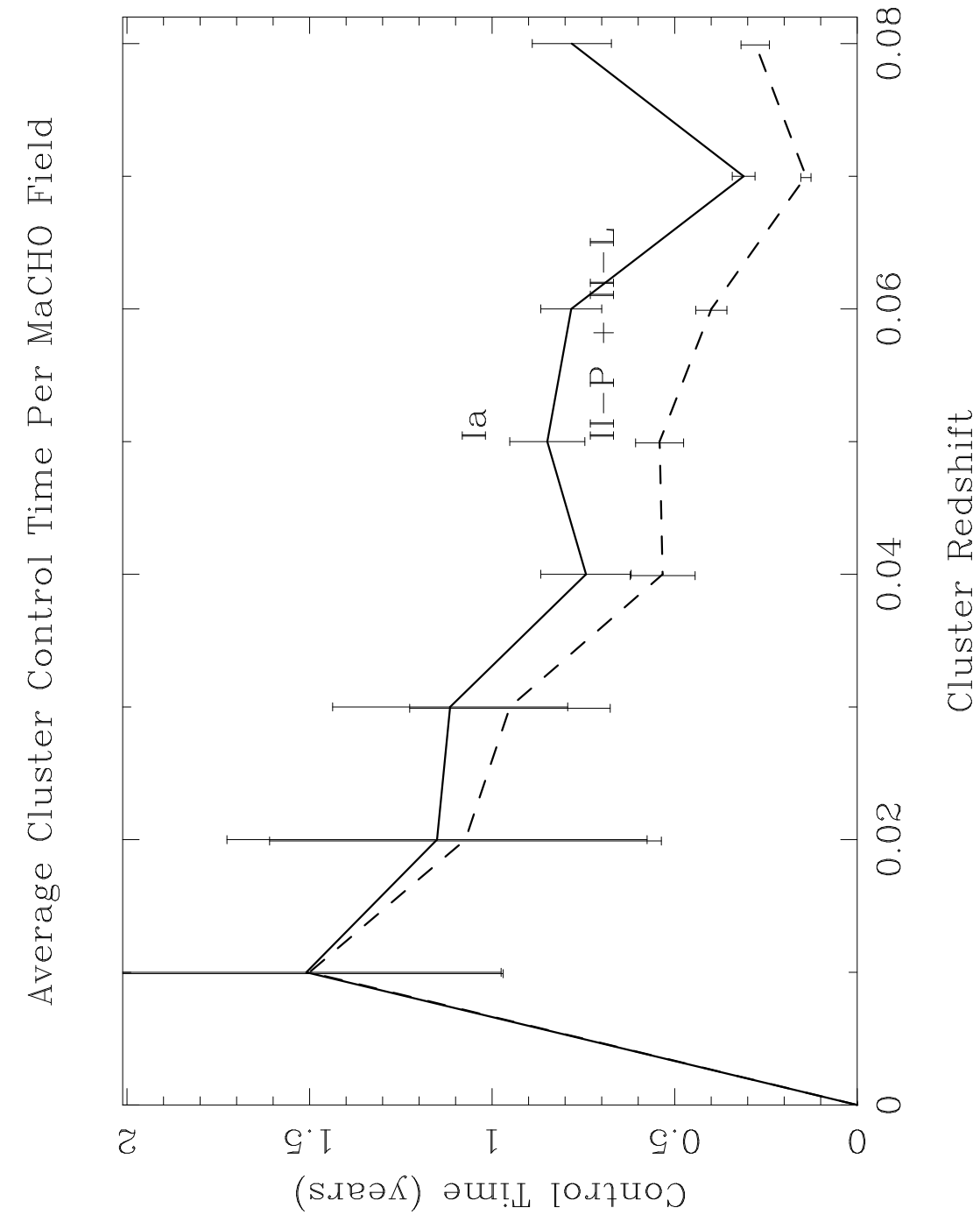

Figure 3.1: Integrated average cluster SN control time for the MSACSS, as a function of redshift. Shown are total control times for SNe Ia (solid curve) and for SNe II-P + II-L added together in the ratio 5:1. Error bars show statistical uncertainty only.

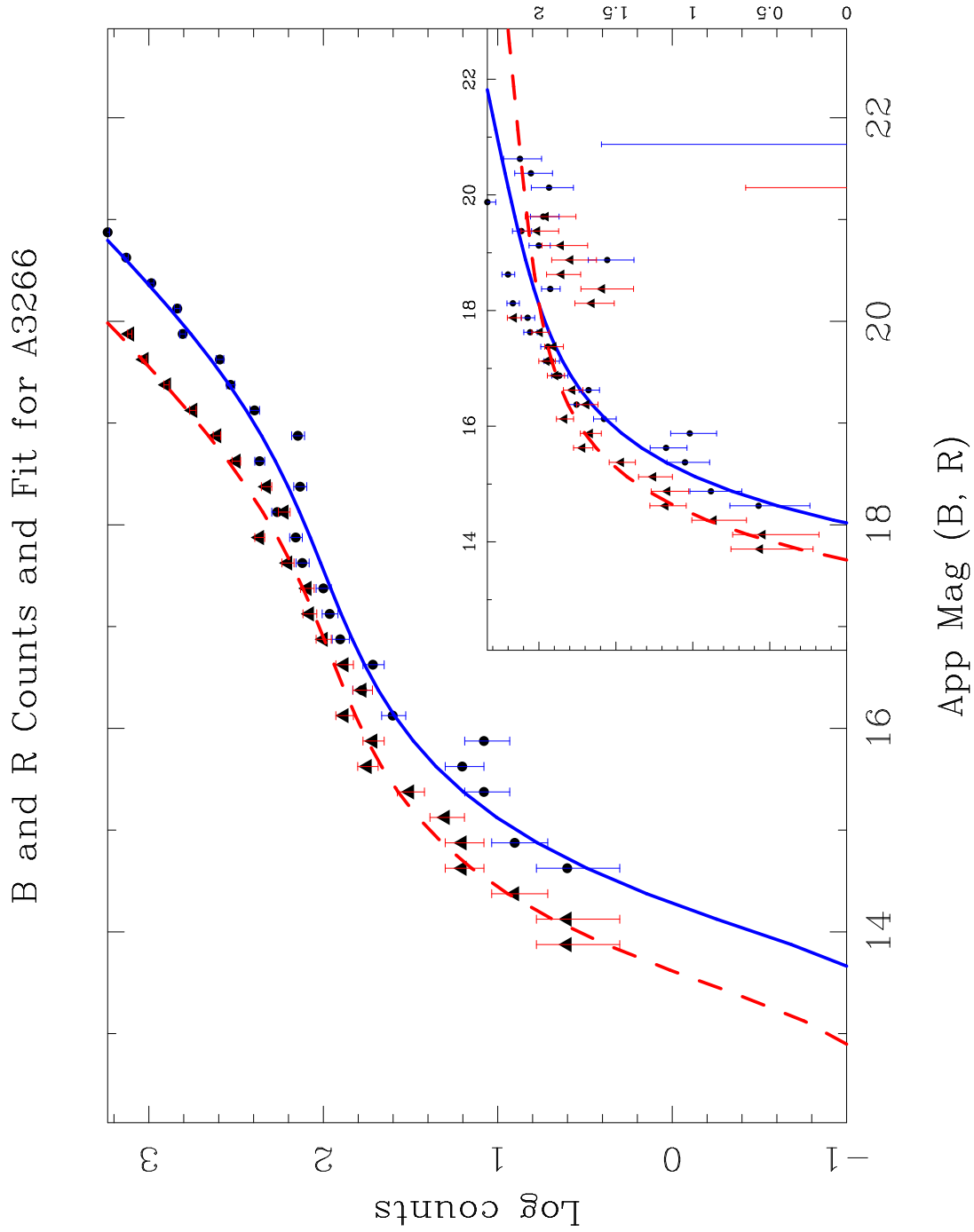

Figure 3.2: Galaxy counts of a typical search field of the MSACSS (Abell 3266), as a function of apparent magnitude. The points show the measured counts, and the lines the analytic fits to these counts, with circles and solid line for the V_M counts and triangles and dashed line for the R_M. *Inset:* The galaxy counts with the fit to the field galaxy contribution subtracted off, plus the best-fit Schechter function, for each passband. The error bars are statistical only.

Table 3.2: The shape parameters used for fits to the galaxy counts of each cluster field (eq. 3.2).

Param.	V_M value	R_M value
γ	0.61 ± 0.1	0.60 ± 0.1
M_*	-20.45 ± 0.4	-21.03 ± 0.4
α	-1.19 ± 0.2	-1.09 ± 0.2

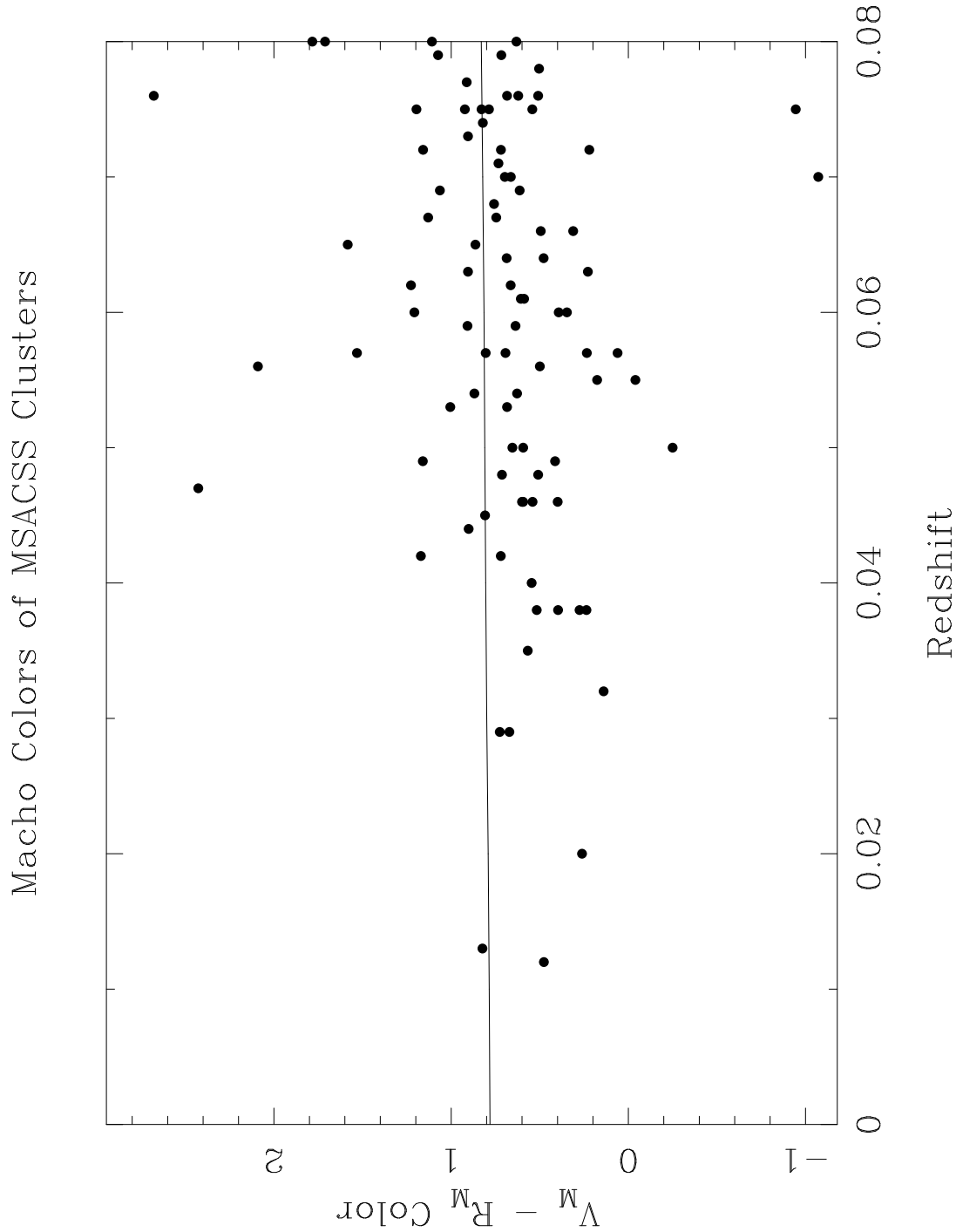

Figure 3.3: Observed V_M and R_M colors of the MSACSS clusters, plotted as a function of cluster redshift. Also shown are synthetic colors of a "cluster composite" spectrum (see text for details).

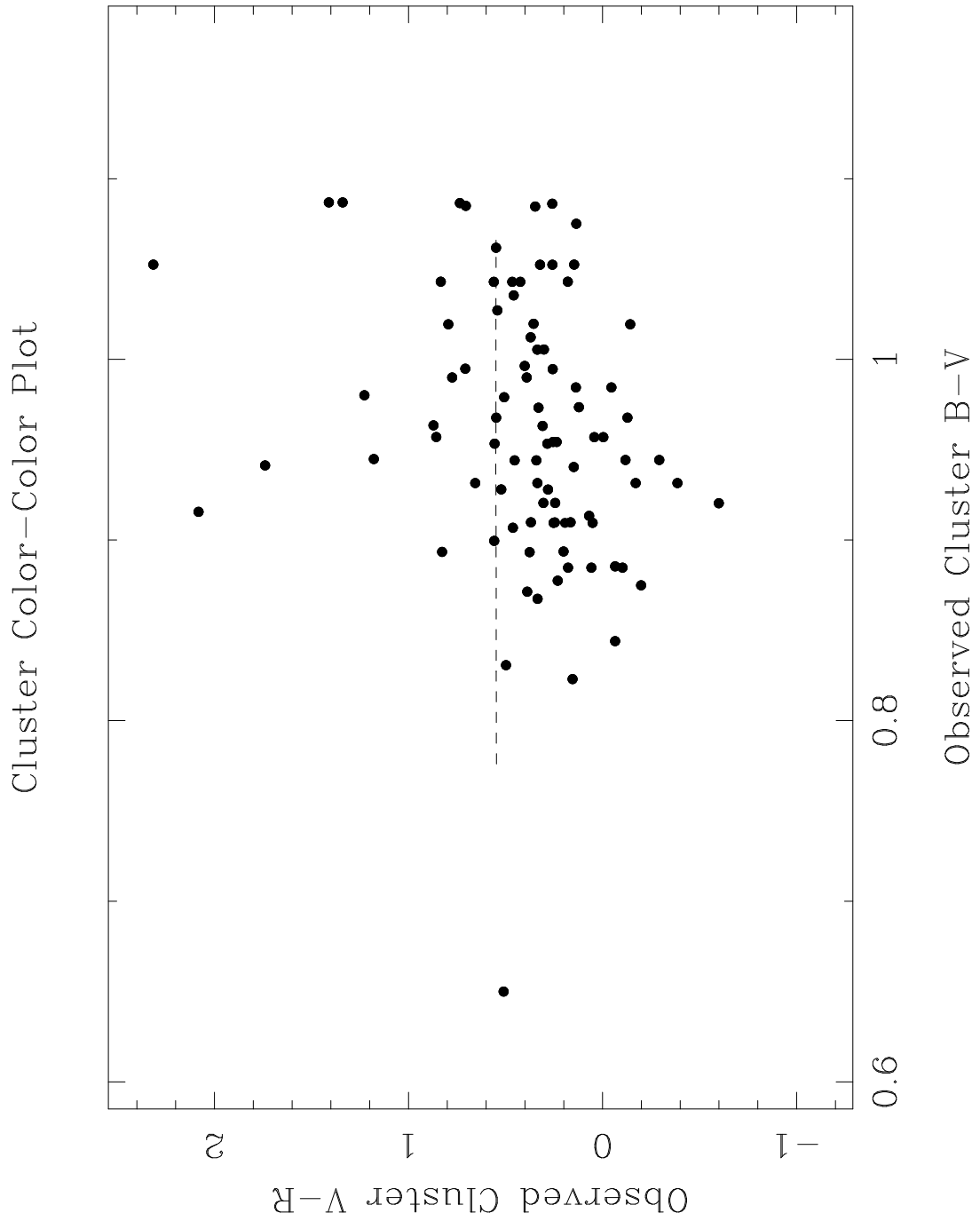

Figure 3.4: Standard $B-V$ vs. $V-R$ color-color diagram of the MSACSS clusters, plotted alongside synthetic colors of a "cluster composite" spectrum, over the redshift range $0 < z < 0.08$.

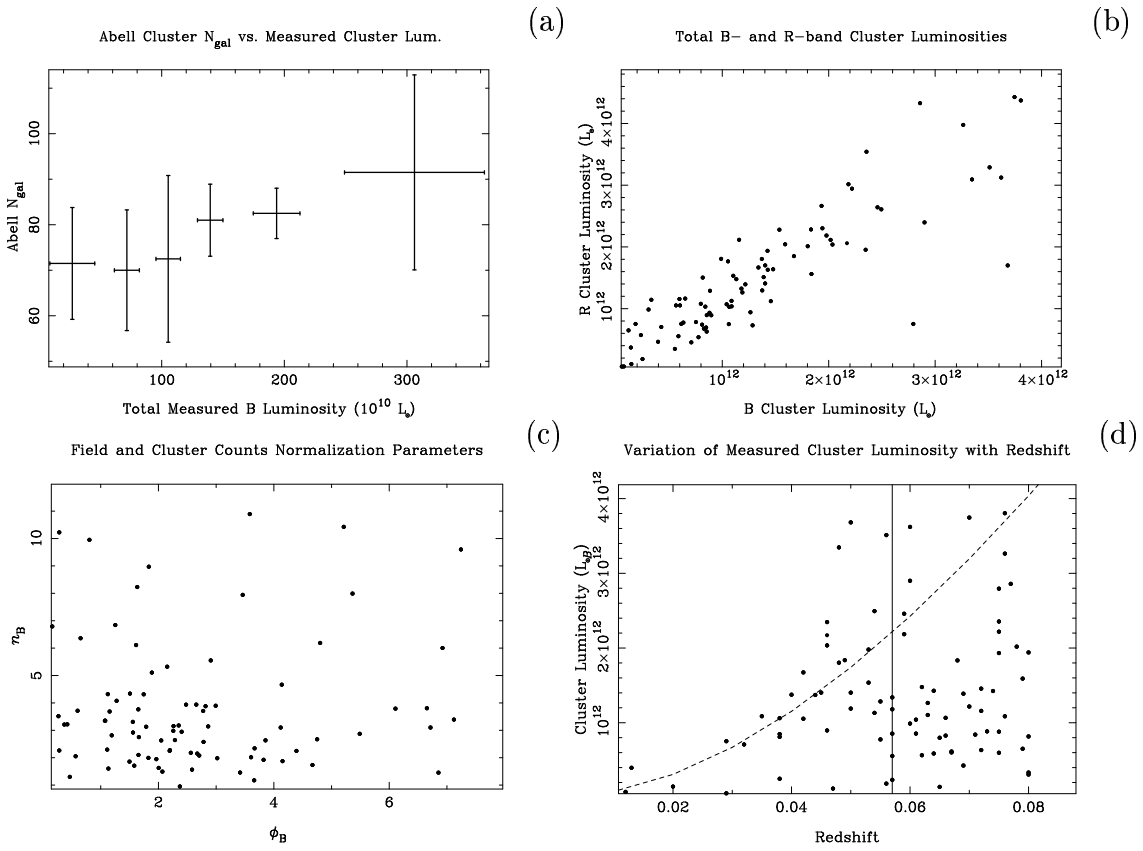

Figure 3.5: Proporties of the measured cluster luminosities. (a): Abell, Corwin, & Olowin 1989 galaxy counts plotted vs. the derived cluster luminosities; (b): measured B vs. R-band cluster luminosities; (c): field normalization values compared to cluster normalization parameters for each cluster; (d): cluster luminosity as a function of cluster redshift. See text for details.

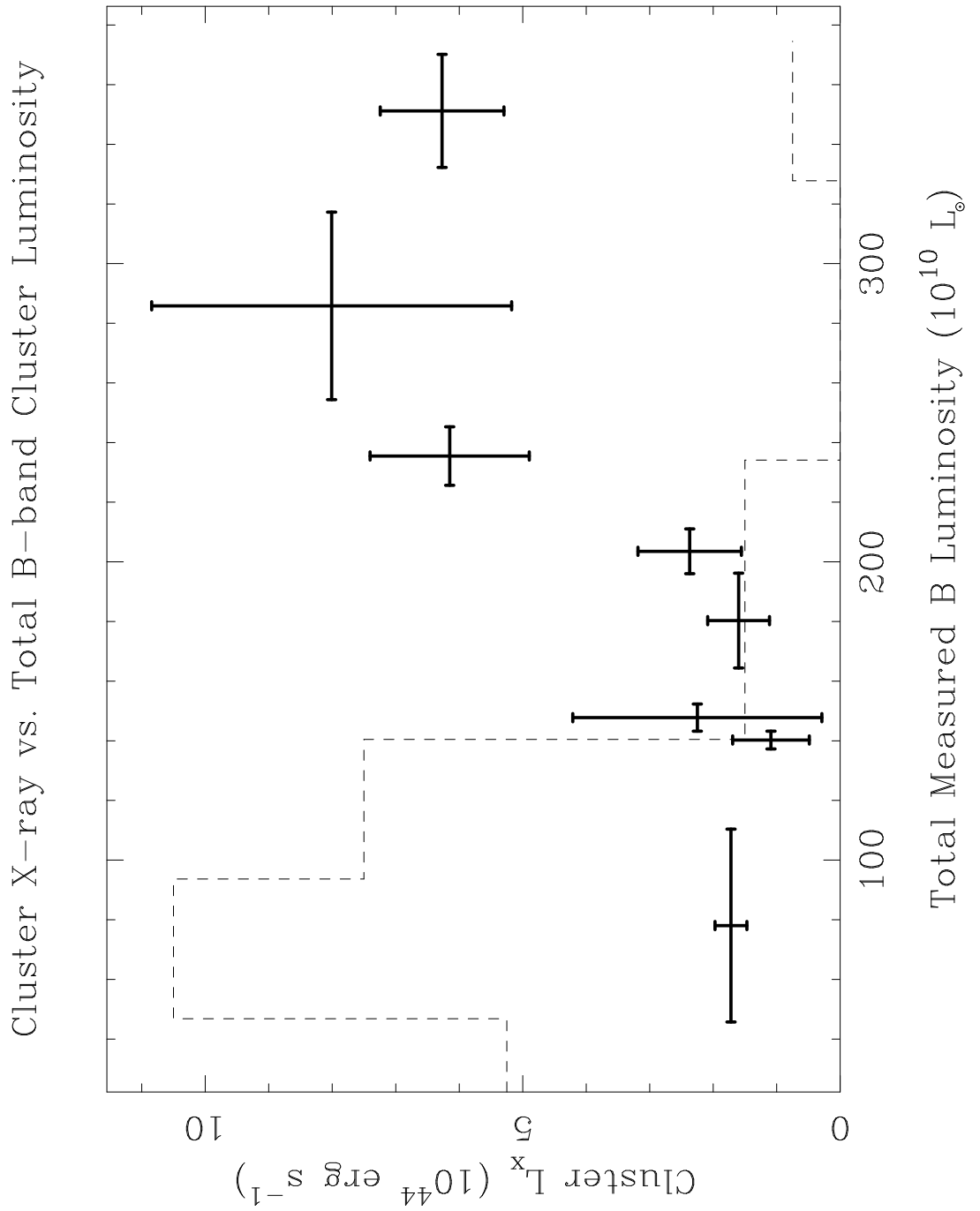

Figure 3.6: Total cluster B-band luminosity vs. X-ray luminosity of Ebeling *et al.* 1996, coursely binned to average over large statistical uncertainties. Also shown (dashed line) is a histogram of those clusters which were too faint to make the X-ray flux limits.

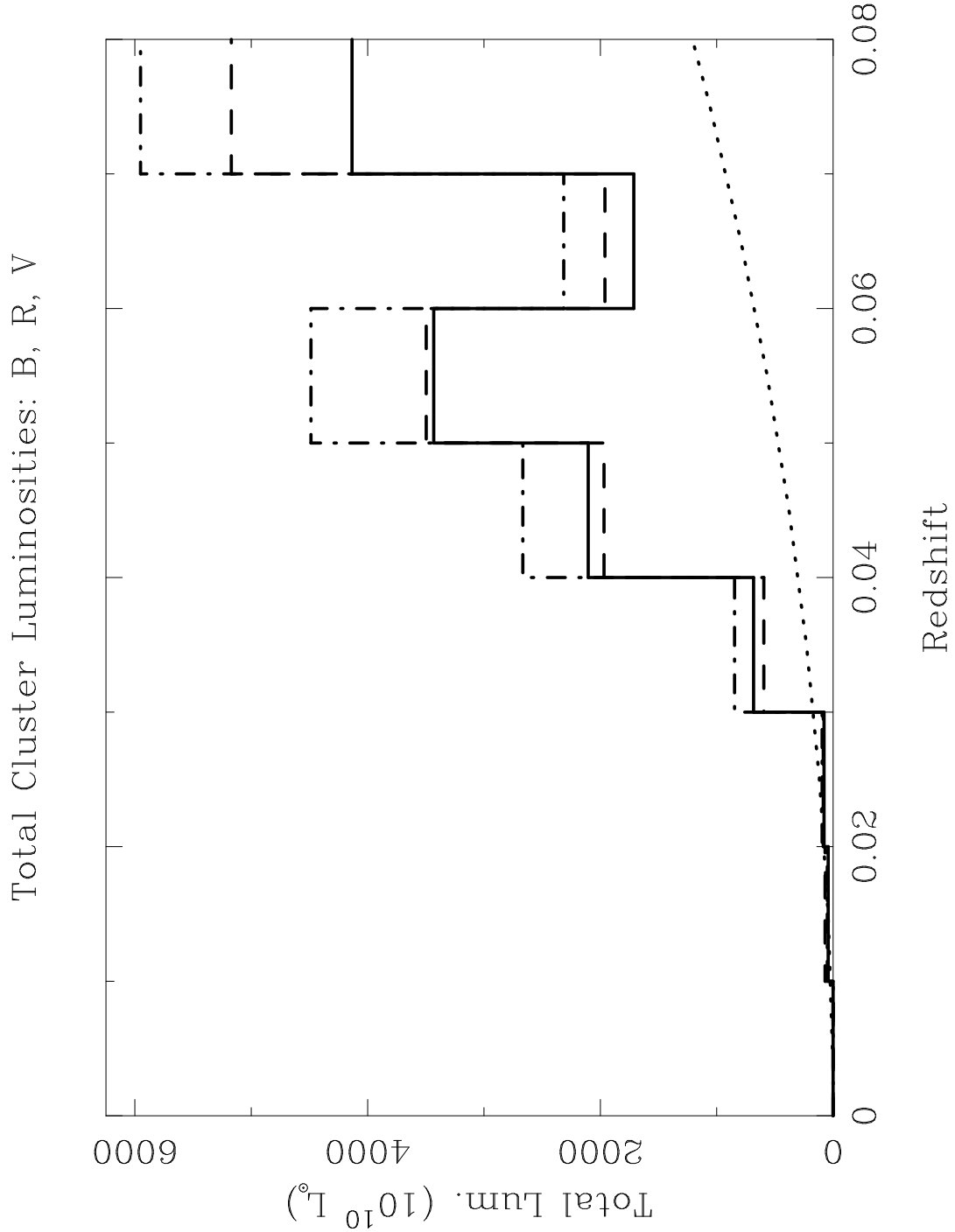

Figure 3.7: Total BVR cluster "control luminosity", binned with redshift, in analogue to Figure 2.4 for the field SN rates. B, V, and R luminosities are shown respectively in solid, dot-dashed, and dashed histograms. The dotted line reveals the total luminosity (equation 2.10, Chapter 2) contributed by field galaxies to the sample at these redshifts.

Table 3.3: Table of MSACSS cluster luminosities and colors used in the derivation of the cluster SN rates. Continues on next page.

Abell	z	Abell N_{gal}	$10^{10}L_{B_\odot}$	$10^{10}L_{R_\odot}$	$10^{10}L_{V_\odot}$	$B-R$	$B-V$	$V-R$
44	0.056	60	33.2566	43.4759	70.6993	2.095	0.941	1.153
119	0.044	69	158.6049	199.5879	166.0214	1.215	0.899	0.316
133	0.057	60	191.4873	251.0655	148.2276	0.925	0.944	-0.019
151	0.053	72	212.3318	275.1677	246.9338	1.364	0.931	0.432
168	0.045	89	182.5916	231.3031	154.4076	1.002	0.907	0.095
261	0.047	63	51.8275	66.0714	45.7538	1.409	0.914	0.495
279	0.080	70	58.6090	87.6198	126.5704	2.102	1.087	1.016
401	0.074	90	152.0015	216.7720	207.5222	1.498	1.035	0.462
423	0.080	89	199.9716	298.8599	237.8130	1.348	1.086	0.262
754	0.054	92	492.2736	635.8727	494.5480	1.179	0.928	0.251
1020	0.065	68	86.4660	117.0662	135.2325	1.626	0.979	0.647
1066	0.070	68	274.7930	381.2311	344.3252	1.435	1.005	0.430
1238	0.072	63	177.6230	249.6189	231.0504	1.512	1.019	0.492
1317	0.072	82	250.7722	352.4178	161.9874	0.849	0.835	-0.171
1644	0.048	92	201.2535	255.6627	267.3453	1.440	0.910	0.530
1648	0.070	68	122.0486	169.3341	134.9319	1.268	1.006	0.263
1736	0.046	104	210.3396	267.1200	204.9251	1.132	0.909	0.223
1773	0.078	66	195.1116	288.6061	220.4700	1.292	1.075	0.217
1780	0.079	71	233.4427	348.3373	168.1626	1.148	1.085	0.063
1809	0.079	78	175.6135	262.0638	217.4019	1.395	1.085	0.310
2029	0.077	82	314.5440	459.6424	430.1607	1.504	1.062	0.443
2063	0.035	63	103.8221	128.0208	96.6681	1.081	0.877	0.203
2362	0.061	69	106.7976	141.3432	109.2810	1.189	0.954	0.235
2401	0.057	66	116.0839	152.2016	127.4972	1.261	0.944	0.317
2469	0.066	61	149.9459	194.1815	136.7542	1.021	0.947	0.074
2480	0.072	108	216.9074	304.8144	52.2448	-0.152	1.020	-1.171
2492	0.071	62	114.4244	148.5420	120.4609	1.244	0.948	0.296
2559	0.080	73	54.4478	78.8991	83.7421	1.242	1.016	0.226
2661	0.064	147	86.0930	115.9565	131.0918	1.454	0.973	0.480
2670	0.076	142	78.0543	113.0840	596.4032	2.264	0.851	1.413
2675	0.071	60	9.6903	11.3527	251.1650	0.732	0.736	-0.090
2799	0.063	63	127.5419	170.9015	99.1348	0.885	0.968	-0.083
2819	0.075	90	172.8956	248.2740	235.0157	1.491	1.043	0.448
2854	0.061	64	104.8108	138.7137	111.6653	1.228	0.954	0.274
2889	0.067	65	35.6450	48.7668	69.1638	2.061	0.991	1.070
2954	0.057	121	56.3158	73.8601	40.0057	0.744	0.945	-0.200
2995	0.038	69	77.3092	98.6729	84.3142	1.071	0.903	0.168
3094	0.068	80	184.3179	253.5788	253.8167	1.502	0.996	0.506
3108	0.062	73	115.2112	153.7488	111.0630	1.282	0.963	0.318
3112	0.075	116	254.1131	364.9004	390.4895	1.625	1.043	0.582
3122	0.064	100	157.9044	212.6627	156.5242	1.155	0.973	0.181
3128	0.060	140	362.0227	480.2713	332.0541	1.064	0.957	0.107
3135	0.063	111	102.2464	137.0063	141.6533	1.514	0.968	0.546
3142	0.066	78	122.6616	166.8999	133.6429	1.233	0.984	0.249
3158	0.059	85	215.2976	284.6764	285.4160	1.465	0.953	0.511
3188	0.076	67	201.2321	291.5116	104.7252	0.577	1.052	-0.476

Table 3.4: Table of MSACSS cluster luminosities and colors used in the derivation of the cluster SN rates (continued from previous page).

Abell	z	Abell N_{gal}	$10^{10}L_{B_\odot}$	$10^{10}L_{R_\odot}$	$10^{10}L_{V_\odot}$	$B-R$	$B-V$	$V-R$
3202	0.069	65	145.2547	199.5062	139.9620	1.117	0.995	0.123
3223	0.060	100	120.4248	159.7844	187.9014	1.660	0.957	0.703
3231	0.057	65	58.2303	76.3699	47.6010	1.157	0.945	0.212
3266	0.059	91	244.5939	323.4135	293.9824	1.354	0.953	0.401
3301	0.054	172	138.3398	178.7172	147.4119	1.247	0.928	0.319
3341	0.038	87	58.4433	72.5540	62.3615	1.299	0.885	0.414
3381	0.038	69	114.7964	142.5030	103.5498	1.024	0.885	0.139
3390	0.032	63	75.2706	92.5982	51.5609	0.743	0.875	-0.132
3392	0.055	77	115.4724	149.6498	76.3484	0.717	0.931	-0.215
3404	0.070	64	240.2237	333.2748	66.6712	0.091	1.006	-0.915
3490	0.069	91	338.2620	464.5678	515.3778	1.657	0.995	0.662
3528	0.053	70	163.5312	211.9394	193.6059	1.359	0.932	0.427
3549	0.075	65	279.4647	401.3047	115.5688	-0.264	0.846	-1.307
3552	0.075	60	85.7195	123.1103	115.1559	1.533	1.043	0.490
3555	0.049	61	99.4320	126.7341	96.4758	1.144	0.782	0.362
3558	0.048	226	370.8100	471.0590	308.1131	0.964	0.910	0.054
3559	0.046	141	159.0780	202.0317	106.4841	0.825	0.910	-0.085
3560	0.013	184	36.4348	43.0338	54.3604	1.587	0.831	0.756
3562	0.050	129	305.8062	392.3098	171.7766	0.557	0.920	-0.364
3565	0.012	64	8.5634	10.0368	6.4078	0.854	0.822	0.032
3566	0.050	100	134.9144	173.0880	145.5840	1.243	0.920	0.322
3571	0.040	126	140.2671	175.5475	134.6019	1.115	0.894	0.221
3577	0.050	103	96.7160	124.0923	105.3790	1.261	0.921	0.340
3651	0.060	75	281.9352	374.0246	546.0925	1.673	0.957	0.716
3667	0.056	85	341.7451	446.5605	335.3712	1.140	0.940	0.199
3698	0.020	71	21.8968	26.1693	19.4479	0.959	0.844	0.115
3716	0.046	66	235.5649	299.1548	183.3330	0.885	0.909	-0.024
3744	0.038	70	114.1418	141.6903	90.1220	0.891	0.885	0.006
3775	0.080	76	52.0767	77.8544	110.8338	2.073	1.087	0.987
3781	0.057	79	50.2928	65.9543	41.9519	0.953	0.944	0.008
3806	0.076	115	360.2496	521.8496	423.5363	1.339	1.052	0.286
3809	0.062	73	152.2455	203.1589	147.5511	1.120	0.963	0.157
3822	0.076	113	414.5646	600.5290	477.7656	1.314	1.052	0.262
3825	0.075	77	246.6652	354.2054	299.8816	1.377	1.043	0.335
3826	0.075	62	84.6622	121.5919	88.4513	1.207	1.043	0.164
3831	0.065	81	20.0575	27.1725	29.7287	1.603	0.980	0.623
3879	0.067	114	72.2976	98.8828	60.1595	0.937	0.990	-0.053
3897	0.073	63	81.5076	110.4343	106.7140	1.432	0.974	0.459
3990	0.029	98	111.3831	141.3277	106.0755	1.181	0.890	0.291
4008	0.055	66	88.2965	111.3195	71.7104	0.907	0.904	0.003
4038	0.029	117	73.6308	89.9543	78.3752	1.228	0.867	0.361
4053	0.072	64	168.4709	236.7572	135.2798	0.916	1.019	-0.104
4059	0.049	66	288.9708	402.6066	302.7665	1.143	0.983	0.160
5481	0.042	80	134.5908	168.4075	169.0541	1.436	0.893	0.542
5482	0.042	80	118.2441	147.9643	172.9998	1.579	0.893	0.686

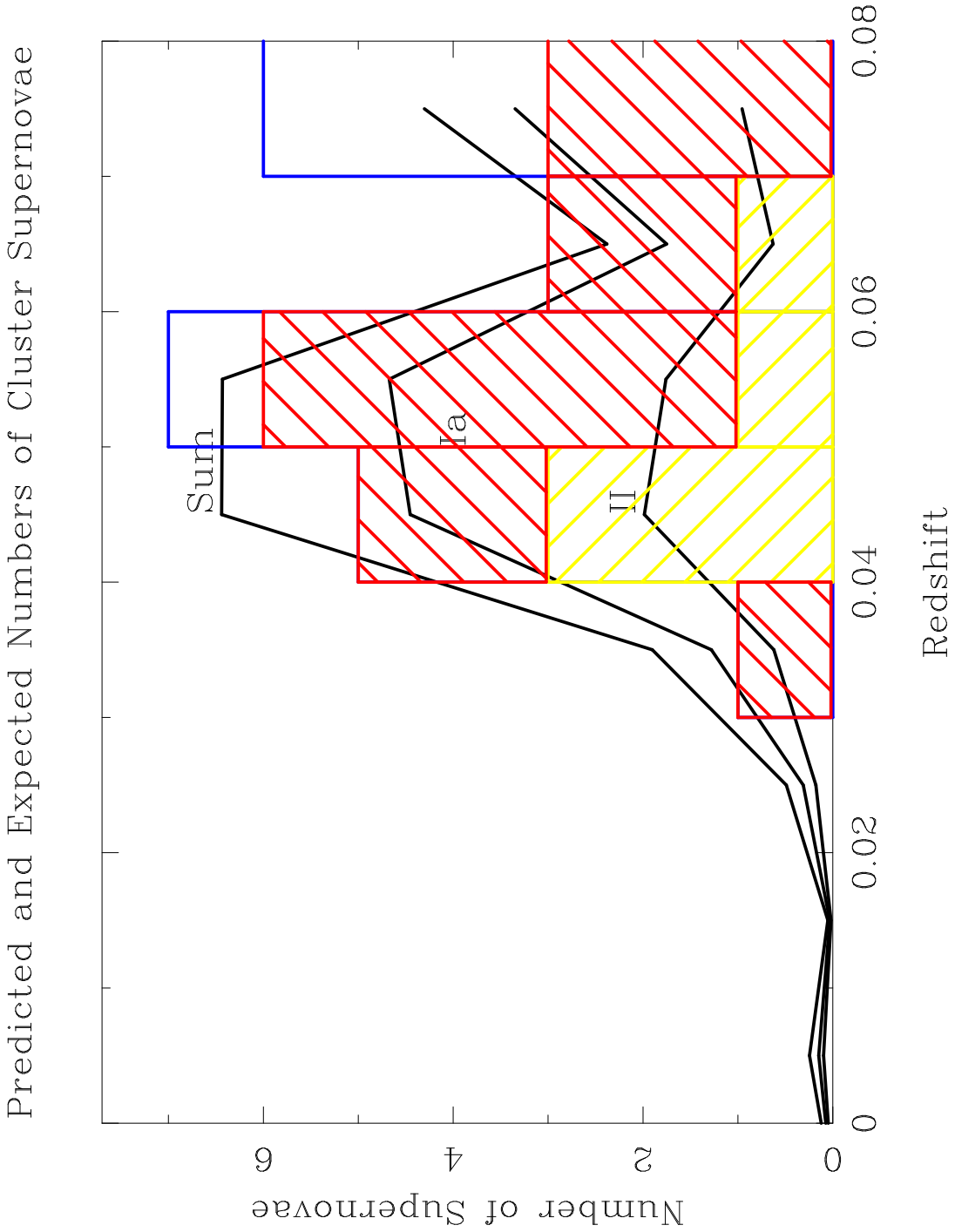

Figure 3.8: The expected and observed numbers of cluster SNe as a function of redshift, calculated for a SN rate of 0.180 (Ia) and 0.124 (II) $(H_0/65)^2$ SNu. Also shown is the observed distribution, with SNe Ia in red, SNe II in yellow, and unclassified SNe in blue.

Table 3.5: Cluster SN numbers, before and after assignment of SN type: observed, expected (with redshifts) and expected (total, including those without redshifts).

SN Type	$N_{\rm obs}$	$N_{{\rm exp},z}$	$N_{\rm exp,tot}$
Ia	13	16.00	17.29
II	5	6.25	7.05
Total	18	22.25	24.34

Table 3.6: Statistical uncertainties in the cluster SN rates: $\sqrt{N}$ statistical uncertainty, uncertainty due to possible mis-classification of SNe, and total uncertainty, in SNu.

SN Type	$\sigma_{\rm stat}$	$\sigma'_{\rm stat}$	$\sigma_{\rm tot}$
Ia	0.044	0.033	0.054
II	0.049	0.058	0.076

Table 3.7: Systematic uncertainty in cluster SN rates: parameters contributing to the uncertainty, the values used to compute the rates, ranges in those parameters, and resulting ranges in SN rates (SNu). The total systematic error is the quadratic sum of all listed contributions except for those marked by an (*).

Parameter	Value	+ limit	- limit	Ia Uncert.		II Uncert.	
H_0 (km sec^{-1} Mpc^{-1})(*)	65	+10	-10	+0.059	-0.051	+0.040	-0.032
Ω_M, Ω_Λ(*)	0.3, 0.7	1.0, 0.0	–	+0.000	-0.006	+0.000	-0.005
Ω_M, Ω_Λ(*)	0.3, 0.7	0.3, 0.0	–	+0.000	-0.004	+0.000	-0.003
γ_B	0.610	+0.1	-0.1	+0.018	-0.029	+0.014	-0.012
M_B^*	-20.45	+0.5	-0.5	+0.030	-0.025	+0.027	-0.027
α_B	-1.19	+0.2	-0.2	+0.012	-0.018	+0.008	-0.009
$\overline{M}_{B,\mathrm{Ia}}$ (mag)	-19.33	+0.2	-0.2	+0.018	-0.016	+0.002	-0.001
$\overline{\sigma}_{\Delta,\mathrm{Ia}}$ (mag)	0.41	+0.05	-0.05	+0.001	-0.002	+0.000	-0.000
Gaussian $F_{\mathrm{Ia}}(E_{B-V})$ w/ $\sigma = 0.3$ mag				+0.000	-0.033	+0.000	-0.001
Gaussian $F_{\mathrm{Ia}}(E_{B-V})$ w/ $\sigma = 0.5$ mag(*)				+0.000	-0.023	+0.000	-0.001
No SN Ia extinction (delta-func. at $E_{BV} = 0$)(*)				+0.002	-0.002	+0.055	-0.032
$\overline{M}_{B,\mathrm{II-P}}$; $\overline{M}_{B,\mathrm{II-L}}$ (mag)	-17.0, -18.0	+0.5	-0.5	+0.003	-0.000	+0.029	-0.006
$\overline{\sigma}_{\Delta,\mathrm{II}}$ (mag)	1.25	+0.5	-0.5	+0.000	-0.000	+0.019	-0.016
$\overline{A_{V,\mathrm{II}}}$ (mag)	1.0	+0.5	-0.5	+0.002	-0.001	+0.040	-0.022
$\sigma_{A_V,\mathrm{II}}$ (mag)	1.0	+0.5	-0.5	+0.001	-0.000	+0.021	-0.010
$\overline{A_{V,\mathrm{II}}} = 0.6$ mag; $\sigma_{A_V,\mathrm{II}} = 0.75$ mag(*)				+0.000	-0.000	+0.000	-0.028
m_{lim} (systematic; mag)	–	+0.1	-0.1	+0.010	-0.009	+0.010	-0.008
m_{lim} (statistical; mag)	–	+0.3	-0.3	+0.002	-0.001	+0.002	-0.002
m_{ceil} (mag)	20.5	21.0	–	+0.000	-0.018	+0.000	-0.008
calibration error (mag)	–	+0.1	-0.1	+0.017	-0.018	+0.013	-0.003
color-conversion error (mag)	–	+0.1	-0.1	+0.017	-0.018	+0.013	-0.003
area searched (% of image)	95%	+3%	-3%	+0.005	-0.005	+0.004	-0.004
Total				+0.046	-0.058	+0.085	-0.052

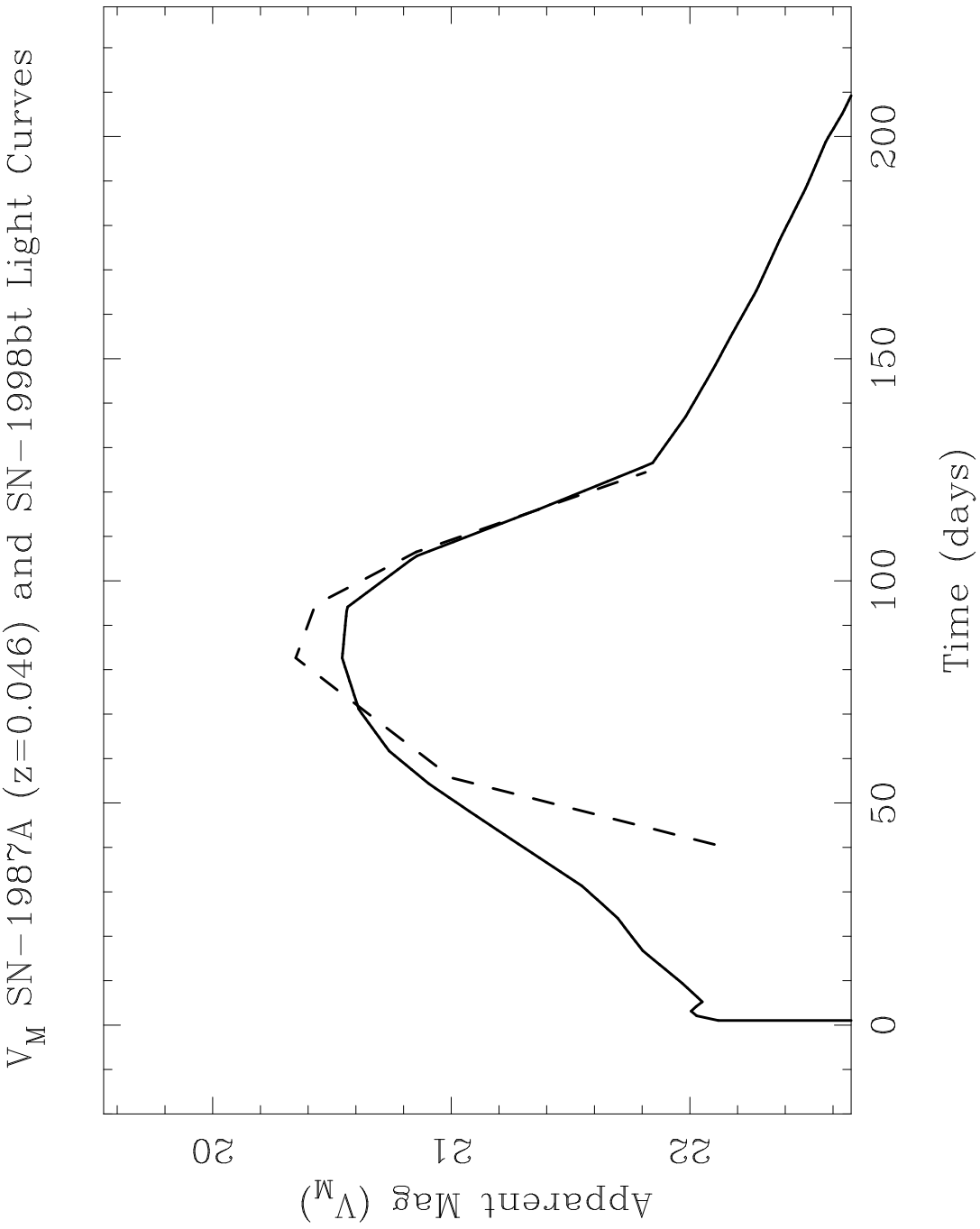

Figure 3.9: The apparent magnitude light-curve of SN 1998bt, and that of SN 1987A, as it would appear if it were at a redshift of 0.046.

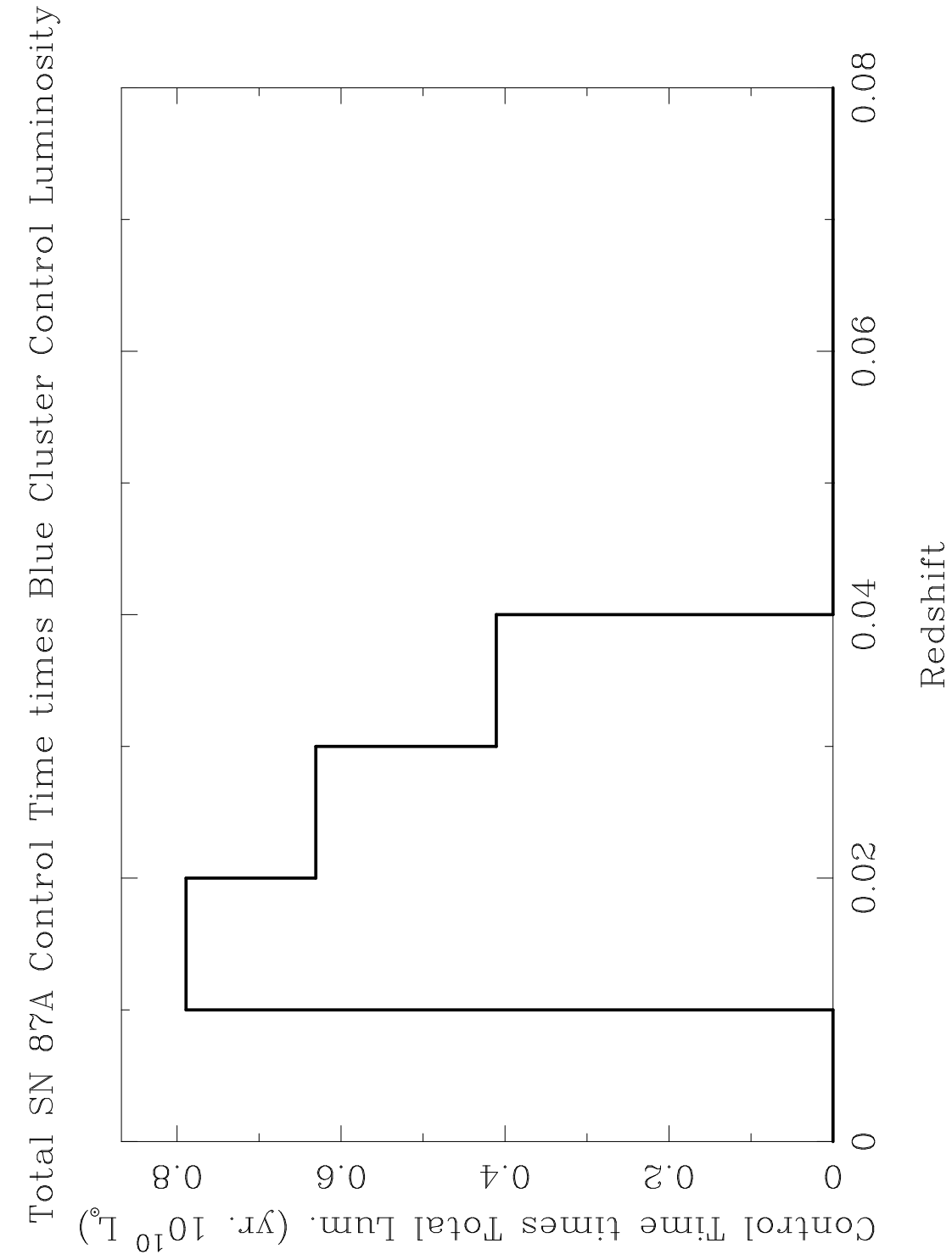

Figure 3.10: Integrated control time × cluster control luminosity for "SN 1987A-like" events in the MSACSS.

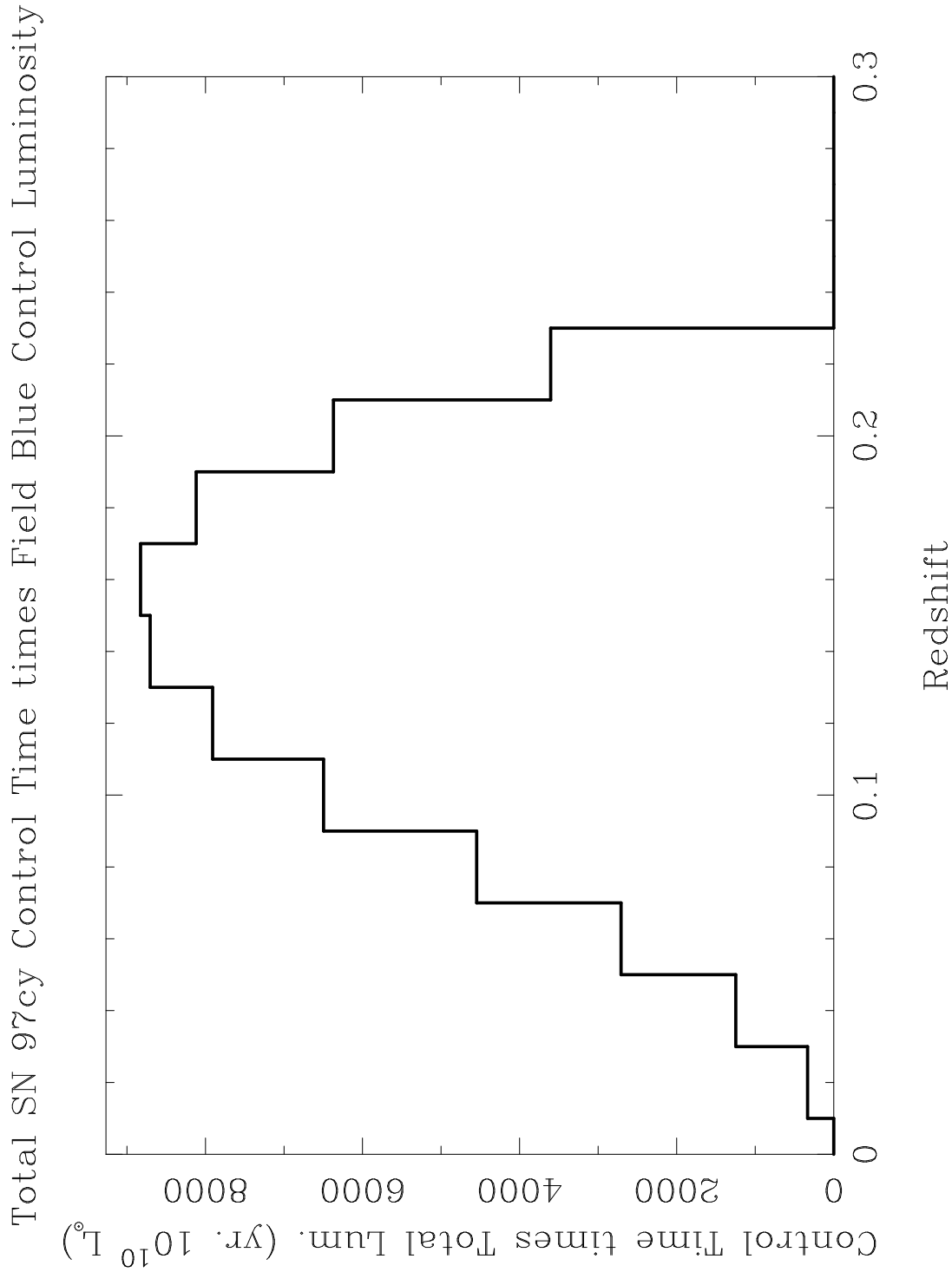

Figure 3.11: Integrated control time × field control luminosity for "SN 1987cy-like" events in the MSACSS.

Chapter 4

THE RATE OF SUPERNOVAE IN DISTANT FIELD GALAXIES FROM THE HIGH-Z SUPERNOVA SEARCH

4.1 Introduction

The recent detections of large numbers of supernovae at high redshift (Riess *et al.* 1998; Perlmutter *et al.* 1997) provide an excellent source for constraining the rate of SNe Ia at $z \simeq 0.5$ and core-collapse SNe at slightly lower redshifts. These endeavors to detect distant SNe have spawned a great amount of interest in the use of SN rates at high redshift to trace the history of various cosmological quantities such as galaxy and star formation (Madau 1998, Sadat *et al.* 1998), heavy element enrichment of the ISM (Renzini 1998, Nagataki & Sato 1998, Barbuy, de Freitas Pacheco, & Castro 1994), cosmological parameters (Ruiz-Lapuente & Canal 1998), and more locally, the nature of SN Ia progenitors (Ruiz-Lapuente & Canal 1998, Ruiz-Lapuente, Canal, & Burkert 1996).

Recently, Pain *et al.* 1996 estimated a distant SN Ia rate at $\overline{z} \simeq 0.38$ from the first sample of three SNe detected early in their search program (Perlmutter *et al.* 1997). Their rate was higher than the currently accepted local value (Cappellaro, Evans, & Turatto 1999), but contained large uncertainties simply due to the small size of their sample and the large systematic uncertainties inherent in estimating distant SN rates. The earlier detection by Norgaard-Nielsen *et al.* 1989 of a SN Ia at $z = 0.31$ also hinted that the high-redshift SN Ia rate might be larger than it is at current epochs. These measurements seemed to imply a short lifetime of the progenitors of Type-Ia SNe because their rate appeared to be increasing with redshift, following

the increase in star-formation seen with increasing look-back time.

In this chapter , we derive the distant SN Ia rate from a sample of $\sim$ 50 SNe detected during the course of the *High-Z* Supernova Search project (Schmidt *et al.* 1997). The implementation of the search as well as the computations involved in determining the rates are the same as those of the Mount Stromlo Abell Cluster Supernova Search (MSCACSS; Reiss *et al.* 1998), for which we have computed nearby field galaxy SN rates at $\overline{z} \simeq 0.11$ (Reiss *et al.* 1999b and Reiss *et al.* 1999a), and rates in nearby rich galaxy clusters (Reiss *et al.* 1999c). They will provide an excellent backdrop for comparison to the rates computed here.

The primary difference between the SN sample described in this chapter and that of the MSACSS lies in the fact that the distant SN sample is collected from a variety of different searches spanning the course of several years, which were performed on different telescopes with different passbands and therefore had varying coverage and depth. Moreover, the purpose of these searches has been to collect as large a number of faint type Ia SNe in real time as is possible; usually more are detected than can be spectroscopically confirmed with 1-2 nights on the Keck and other smaller telescopes. The "better" candidates must be selected for confirmation through a wide array of subjective criteria. This means that there are selection effects involved in this search which are far more difficult to quantify than those of the MSACSS.

Oftentimes (particularly in the case of the fainter candidates), after the search and confirmation spectroscopy has been completed, we still do not know the SN classification, or even the redshift, of a significant number of candidates (see below). We cannot eliminate these objects from our sample because that would bias our derived rates low. On the other hand, we cannot treat them as definite SNe as (due to contamination by AGN and other time-variable objects) this would bias our rate high. These problems are extreme at fainter discovery magnitudes ($m \gtrsim 23.5$), but because brighter objects are easier to classify, a larger fraction of objects with $m \lesssim 23.2$ are classified and have measured redshifts. Imposing a magnitude cutoff, both on the

SN sample and in the computation of the control times, is a straightforward route to take in this case. Choosing a reasonable cutoff so as to maximize the fraction of the sample with measured redshifts and classifications will help to reduce both classification and completeness problems. Furthermore, varying the magnitude cutoff slightly should not change the derived SN rate, if the computation is to be deemed robust. This is the method we employ here. The sample of SNe used in this paper is described in section 4.2. We briefly summarize the calculations of the control time and control galaxy luminosity used to compute the rates in sections 4.3.1 and 4.3.2. We then derive the SN rates in section 4.4, and discuss their uncertainties, and their implications, in sections 4.5 and 4.6.

4.2 The Sample of High-Z Supernovae

The sample of SNe was collected from the discoveries of five different searches conducted between April 1997 and January, 1999. All relevant information about these searches and their resulting detections are listed in tables 4.1 and 4.2(a–e). Table 4.1 lists the time and site of the search observations, and the passband use for the search. *dt* denotes the time (in days) elapsed between the template and search observations, and is required in the computation of the total control time of each search. The Jan. 1999 search utilized templates obtained at various times more than a year prior to the dates of the search observations. Also listed are the total area searched, the effective limiting magnitude, and the mean galactic reddening over the area that was searched.

The approximate limiting magnitudes of the searches were derived both through an analysis of the apparent magnitudes of the discovery candidates (listed in tables 4.2 and shown in Figure 4.1), as well as through a series of Monte-Carlo simulations in which a number of false stars were placed at random locations on the search images and processed through the search software (Schmidt *et al.* 1997), in a

Table 4.1: The characteristics of the High-Z SN searches used in this paper

Date	Telescope/Camera	Passband	dt (days)	Area (deg^2)	m_{lim}	$\overline{E_{B-V}}$
Apr. 1997	CFHT/8k mosaic [1]	I	24	0.929	23.3	0.1301
Jan. 1998	CTIO4m/BTC [2]	I	26	1.029	23.3	0.0411
Mar. 1998	CTIO4m/BTC	I	27	1.512	23.3	0.0329
Jan. 1999	CTIO4m/BTC	I	$\gtrsim 365$	1.731	23.0	0.0425
Jan. 1999	CTIO4m/BTC	R	$\gtrsim 365$	3.029	23.3	0.0458

[1]Metzger, Luppino, & Miyazaki 1995

[2]Wittman *et al.* 1998

manner very similar to that described in Chapter 2, §2.3. These five searches were chosen because they covered a large area of sky, they resulted in a large enough number of discoveries that would allow a statistically significant measurement of the rate on small subsamples, and they furthermore were deemed (due to their apparent depth) to be spectroscopically complete (*i.e.* have measured redshifts and/or spectral classifications) to $m \lesssim 23.0$. Figure 4.1 supports these characterizations clearly by showing that the overall sample of SNe increases in number following a power-law distribution at bright magnitudes (as is expected in a purely magnitude-limited sample at magnitudes significantly brighter than the magnitude limit), and then begins falling off at magnitudes fainter than $m \simeq 23.5$. Only one of the five searches (the Jan. 1999 I-band one) was judged to have a brighter limiting magnitude than the others, due to fringing problems experienced on the Big Throughput Camera (Wittman *et al.* 1998) on the CTIO 4m in this passband, which resulted in poorer subtractions.

The mean galactic reddening $\overline{E_{B-V}}$ for each search was computed from the reddening maps provided by Schlegel, Finkbeiner, & Davis 1998, averaged over the

values for the central coordinates of each field observed during the given search. These values are later used in the calculation of the total control time for each field, following the computations of Chapter 2(equation 2.5).

The last column in table 4.2 reveals details about several objects that were originally thought to be SNe and therefore are listed in the sample above for completeness. Among these objects are variable stars and apparent QSOs which were only identified as such after spectroscopy was performed. Many of the objects listed as QSOs were classified as such simply because they were not recognizable as any known SN type. Note that these are more numerous in the Jan. 1999 sample, because the template images were obtained more than one year prior to the search, allowing plenty of time for AGNs to vary by enough to become detectable. Many other objects have no classification or redshift because there was not sufficient time to obtain any spectroscopy whatsoever. Because these objects were not ranked with enough urgency to require spectroscopy, they have a smaller probability of being SNe than those that *were* classified. However we have no choice here but to consider them as likely to be SNe than their classified counterparts were. Many of these likelihoods are shown in the lower panel of figure 4.1 as a function of limiting magnitude. The brighter samples have a greater fraction of spectroscopically-confirmed objects, and are less contaminated by objects such as QSOs, however at no limiting magnitude is a sample 100% complete.

It should be apparent that the task of choosing a reasonably complete sample for computing SN rates from these data is difficult. We choose to assign unclassified objects reasonable classifications based on the remainder of the sample that has been classified. Similarly, we will assign redshifts to objects with no measured redshift, based on the predicted redshift distribution of SNe that will be computed in the next section. Finally, we will do this for varying limiting magnitudes to test the consistency of the calculation; the brighter samples will be more trustworthy (for example, spectra were obtained for $\sim$ 90% of the objects with mags brighter than

$\sim$ 23.0, but this number decreases to $\sim$ 70% when the magnitude cut is increased to 23.75), but will have a larger statistical uncertainty with their smaller numbers. Note also that the total number of classified SNe Ib/c is extremely small (one), and it is reasonable to merge the core-collapse SNe together in the calculation of the rates.

4.3 Summary of the Calculations

4.3.1 The Control Times

The control times of the searches are computed individually for each of the five searches using the parameters listed in Table 4.1. The procedure is essentially identical to that described in Reiss *et al.* 1999b. The only differences are that in this case there is only *one* observation (whereas there were 20–40 per field in the MSACSS), and that the search is in one passband only. Therefore the implementation of the control time computation is much more straightforward. In summary, the control time, which gives the duration which a SN would be detectable, must be calculated as a function of several parameters, all of which affect the evolution of the apparent magnitude of the SNe. These parameters are the SN type (through the light curve shape and mean intrinsic magnitude, plus the difference from the mean, Δ, if there is an intrinsic dispersion), the redshift z (through the luminosity-distance, K-correction, and time-dilation of the light curve), and the host-galaxy reddening E_{B-V}. Furthermore, due to the nature of the subtraction process which is used to detect SNe within galaxies, the time separation between template and search observations is important. For the Apr. 1997, Jan. 1998 and Mar. 1998 searches, the small time-separation of $\Delta t \simeq 26$ days results in a control time that cannot get much larger than one month. On the other hand, the Jan. 1999 search with $\Delta t \gtrsim 1$ year between template and search observations has a significantly greater control time. Figure 4.2 portrays the effects of the subtraction on the observed light curve, and on

the control time for a typical type-Ia SN, at various redshifts, in which the search has a limiting search magnitude of 23.4, and a Δt of 26 days (solid curves). Also shown for comparison are light curves for a $\Delta t > 365$ day search (dashed curves), which displays no effect of the subtraction. The computed control times at each redshift are also listed for both cases of Δt, revealing that at low-redshift, the January 1999 search will dominate the control times simply because of its large Δt (as well as its large sky coverage).

In figure 4.3 we display the total control time for a typical ($\Delta = 0$, $E_{B-V} = 0$) SN Ia, with a limiting magnitude of 23.4 and time-separations Δt of 26 and 365 days, respectively in the solid and dashed thick lines. The latter has control times which are always greater than the former, though this discrepancy decreases monotonously with redshift.

The control time $t_c\,(\text{type}, z, \Delta, E_{B-V})$ is then convolved with model distributions which describe the luminosity function and reddening distributions for each SN type, resulting in $t_c\,(\text{type}, z)$. The SN population distributions and K-corrections are identical to those that were used in the MSACSS calculations (Reiss *et al.* 1999b). Once the control times are integrated over the distributions, for each search, they are added together to derive a total integrated control time, as a function of redshift and SN type, which describes all of the searches together. This means that, with a combined sample of ~ 70 SNe (including a few possible QSOs), we may estimate the SN rates after imposing magnitude cuts at brighter values than those reported in table 4.1, both in the sample and in the computed control times. This is an excellent test of the robustness of the rate calculations. The total number of SNe which are used in such computations may be visualized in the lower chart of figure 4.1.

There are several reasons to believe that the control times computed at $z \lesssim 0.3$ and $z \gtrsim 0.7$ will be subject to large inaccuracies. At high redshift, the cross-filter K-corrections which contribute to the control times become larger and more uncertain due to poor spectrophotometry available at short wavelengths. Any uncertainty

in the apparent peak brightness of SNe at these redshifts could contribute a large fractional error to the total control time, since the control times are rather short (see figure 4.2). These small errors in the control times are further amplified when multiplied by the quickly rising galaxy control luminosity at high redshift (see below) to estimate the total SNu^{-1} to which the search is sensitive. To reduce these effects, we will therefore not include any SNe or control times from redshifts higher than 0.7.

At low redshift, there are two problems with the control times. The first is that, as figure 4.2 reveals, at low-z the control times are dominated by the Jan. 1999 search with its long time separation between template and search observations. These control times are themselves dominated by estimates of the brightness of the SNe at times long past peak brightness, where the K-corrections are extremely uncertain due to lack of spectrophotometry to compute them. We simply linearly extrapolate the K-corrections from those of early times ($t \lesssim 40$ days). This is a reasonable approach, as the colors at these late epochs evolve linearly, however any extrapolation of noisy data is dangerous and we could easily be in error by $\gtrsim 1$ mag in the K-corrections at very late epochs ($t \gtrsim 100$ days).

Another result of the fact that at low redshift the control times (for $\Delta t \gtrsim 365$ days) are dominated by SNe far after peak brightness is that they are also dominated by SNe that are far fainter than their host galaxy. This effect is true particularly for SNe Ia, and can best be viewed in figure 4.4, which shows the median *absolute* magnitude of SNe that contribute to the overall control time, for the three primary SN types, at different redshift. The dispersion for the SNe Ia is included for reference. At $z \lesssim 0.3$, where a large fraction of SNe Ia should be detected when they are ~ 2 mag fainter than a "typical" galaxy while such a galaxy has a bright apparent magnitude (and will therefore be noisier in the subtractions), it is likely that a large fraction of such SNe are missed. This is supported by the fact that no confirmed SNe Ia were found during the Jan. 1999 search at epochs greater than about two weeks

past peak, and very few were found at $z \lesssim 0.3$. It is not in contradiction to the claims of Reiss *et al.* 1999b, which suggested that the search is sky limited even in the centers of galaxies; no Monte-Carlo simulations to test the efficiency of the search technique were run in extreme cases where $M_{\rm SN} - M_{\rm hostgalaxy} > 2$. Rather than incorporating the result of such a test into the control times through models of the redshift evolution of the mean luminosities of field galaxies, which would add additional potential systematics into the calculations, we simply choose to not include any SNe or control times from redshifts below 0.3 in our rates calculations.

Imposing these redshift cut-offs will not decrease the statistics substantially, as there are few SNe with measured redshifts $z < 0.3$ or $z > 0.7$ in our sample, while it should potentially eliminate a few pesky systematics.

4.3.2 The Total Galaxy Control Luminosity

The total control luminosity is computed, just as are the control times, in an identical manner to those of the low-redshift rates of the MSACSS (Reiss *et al.* 1999b). We use the power-law parameterization of Lilly *et al.* 1996 to describe the redshift-dependence of the luminosity density, adjust it to a ($\Omega_{\rm M} = 0.3$,$\Omega_\Lambda = 0.7$) cosmology, and normalize this to the local luminosity density as summarized by Fukugita, Hogan, & Peebles 1998 (eq. 2.10). This blue luminosity density parameterization, $\mathcal{L}_B(z)$, is valid to at least $z \simeq 1.0$. A multiplication of $\mathcal{L}_B$ by the total cosmological volume (Carroll, Press, & Turner 1992), or by volumes binned by redshift, results in the total "control luminosity" surveyed, $L_B(z)$. This method of describing the total galaxy luminosity, when computed for a $(\Omega_{\rm M}, \Omega_\Lambda) = (1.0, 0.0)$ cosmology, for example, results in a total galaxy luminosity per redshift bin at $z \simeq 0.5$ that is very close to that computed by Pain *et al.* 1996. The large uncertainty in the rate of increase in the galaxy luminosity density [$\mathcal{L}_B(z) \propto (1+z)^{(2.7\pm0.5)}$] results in a large uncertainty in the total control luminosity at these higher redshifts, and therefore in a greater systematic uncertainty, which will be enumerated in section 4.5, in the high-z rates.

The control luminosity over $0.0 < z < 1.0$, integrated in bins of $z = 0.05$ for a 1 deg^2 field, is shown alongside the SN-Ia control times, in figure 4.3 as the thin solid line.

4.4 The High-Z Supernova Rates

Multiplying the total control luminosity per redshift bin $L_B(z)$ by the integrated control time for each SN type (here, just SNe Ia and II), $t_c\,(\mathrm{type}, z)$, results in the un-normalized expected redshift distribution of SNe. This portrays the number of SNu^{-1} surveyed, and the number which directly normalizes the curve to the sample of detected supernovae is the SN rate, r_{type}. Figure 4.5 shows the normalized curves, $N_{\mathrm{exp}}(z) = r_{\mathrm{type}} \times L_B(z) \times t_c(\mathrm{type}, z)$, for the two SN types, alongside redshift histograms of the detected SNe with $m < 23.3$, for each of the five searches considered here. Due to the small numbers, a valid comparison of the observed and predicted redshift distributions for each search is difficult, however a combination of the five samples shown in figure 4.6 reveals that the match is good. A Komolgorov-Smirnov shows that we can reject the hypothesis that the predicted and observed distributions are *not* the same (within $0.3 \leq z \leq 0.7$) with a probability of only 50%.

The fine match of the cumulative observed and model distributions, especially at the higher-redshift end of the distribution, is further testament to the completeness of the searches, which confirms that they go at least as faint as the characteristic limiting magnitudes listed in table 4.1. The high-redshift tail of the distribution also shows the power that this technique can be in independently providing a simultaneous constraint on the star-formation history and makeup (*i.e.* Ω_{M} and Ω_{Λ}) of the universe, and the population and evolution of the SN Ia progenitors (Ruiz-Lapuente & Canal 1998). For example, in an open universe, we would predict more detected SNe at high-redshift due to the more rapid increase in physical galaxy density with redshift.

Perhaps a bit disconcerting is the apparent lack of low-redshift SNe Ia in the

detected sample relative to the predicted distribution. There is certainly a selection bias against detecting SNe Ia at $z \lesssim 0.1$ as these will be saturated in the search images, and saturated regions are not searched. However, as discussed in section 4.3.1, a large percentage of SNe Ia are probably not detected at low redshift because of the decreased contrast between intrinsically faint SNe and apparently bright host galaxies. A SN redshift distribution compiled from the IAU circulars from the Supernova Cosmology Project ($\sim$ 90 SNe in all), who use a similar image-subtraction search technique to ours, shows a very similar deficit at low redshifts, which they quantify in Pain *et al.* 1996 as a decrease in search efficiency when the disparity in SN and host galaxy magnitude increases past $\sim$ 1.5 mag. This selection bias is further enhanced by the fact that faint SNe detected on bright hosts are usually recognized as either SNe II or SNe Ia long past peak and are not given high priority for spectral and photometric follow-up observations. Following this analysis and the results of Pain *et al.* 1996, we correct our final derived rates by not including any control time computed for SNe Ia with discovery magnitudes fainter than $M_V > -17.3$, to account for this selection effect. We use this approximation because most of the SN Ia control time occurs in galaxies brighter than $M_V > -19.3$, and as was noted, a significant number of SNe are missed when they reach $\sim$ 2 mag fainter than their host galaxies.

Table 4.4 lists the effective redshift of the sample ($\overline{z_{\rm eff}}$; equation 2.13), and the SN rates r for both type Ia and core-collapse SNe, computed as a function of the imposed magnitude cutoff. The uncertainties are statistical only, and include the estimated uncertainty contributed by the probabilistic assignment of SN types to objects which were not classified and of redshifts to those for which a redshift was not available (see section 2.7). These contribute substantially to the statistical uncertainty since there are a large number of such objects, particularly as the magnitude limits get fainter. This is the reason that the statistical uncertainties do not decrease significantly with increasing cutoff magnitude (as one would expect as the sample size increases). This

is easily seen in columns (3-6) where we describe the entire sample of SNe brighter than each cutoff magnitude listed: the sample's size (N_{SN}), the number of positively classified SNe Ia and SNe II ($N_{\rm Ia}$ and $N_{\rm II}$), and the total number of objects for which redshifts were unattainable ("no z").

The SN rates of table 4.4 are shown in figure 4.7, where the low-redshift field (F) and cluster (C) SN rates are also plotted for comparison (their x-axis position is irrelevant; the low-z field type-II rate is off the scale at 0.896 ± 0.39 SNu). The most encouraging point of this chart is that the high-z SN Ia rate calculation is apparently rather robust, regardless of the magnitude cutoff (within reasonable limits), given the uncertainties. There is a trend of a small increase in the rate at brighter m_{cut}'s than the true limiting magnitudes of the searches listed in table 4.1 (perhaps due to an increasing contamination by fainter QSOs or other objects in the fainter sample), followed by a decrease in the rate at limiting magnitudes where the search was not complete. This trend may also be a symptom of the fact that we seem to have detected fewer low-redshift SNe than are predicted (see above); this will have the effect of biasing the SN rate low for the bright samples. It may also be explained by Poisson statistics as portrayed by the error-bars on the SN-Ia rates in figure 4.7.

We choose the rate at our fiducial magnitude cutoff ($m_{lim} = 23.3$) as the most appropriate: $r_{\rm Ia} = 0.278\ (H_0/65)^2$ and $r_{\rm II} = 0.423\ (H_0/65)^2$ SNu. A systematic uncertainty of $0.026\ (H_0/65)^2$ and $0.067\ (H_0/65)^2$ SNu in these values, from the range of rates computed at varying magnitude cutoff, may also be inferred; these are smaller than the total statistical uncertainty in the rates, and they include certain possible systematic effects such as contamination by QSOs and AGNs, as well as the low-redshift deficit described above. This systematic will be re-addressed in section 4.5.

It is obvious from the figure 4.7 that the core-collapse rate is extremely uncertain, simply due to the small numbers of confirmed objects (*e.g.* three for a m_{cut} of 23.3) and the large uncertainties involved in the computation of their control time due to

their great photometric inhomogeneity (see section 2.4.4), and due to the difficulty of finding these fainter objects in typically (apparently) brighter host galaxies. There furthermore exists a selection bias against classifying type-II SNe during the searches, because apparent SNe that appear bright relative to their host galaxies are often preferentially selected for spectroscopy over those that appear faint relative to large or bright (and particularly spiral) host galaxies. For the remainder of this paper, the core-collapse rate will be considered only inasmuch as it affects the calculation of the SN Ia rate by quantifying the approximate amount of "contamination" of the SN Ia sample by type-II SNe. On the other hand, given these various selection biases against finding type-II SNe in these searches, the derived SN II rate may be considered a reasonable *lower limit* of the true value at these look-back times.

4.5 Uncertainties and Systematic Errors

The various contributions to the statistical uncertainties, computed using the methods described in Reiss *et al.* 1999b, section 2.7 are summarized, for the case of $m_{cut} = 23.3$, in table 4.5. It is clear that the uncertainty contributed by SNe that were not classified spectroscopically ($\sigma'_{\rm stat}$) dominate over the regular $\sqrt{N}$ statistical uncertainty ($\sigma_{\rm stat}$); this is true for all m_{cut}, but more particularly at faint m_{cut}. In order to decrease the statistical uncertainty in the future, it will be more important to spectroscopically classify a larger fraction of the objects than it will be to simply increase the size of the detected sample.

The distant SN rates are subject to systematic uncertainties from identical sources to those which affect the nearby field SN rates Reiss *et al.* 1999b. However, the magnitudes of many of these systematics are larger here. Following the analysis of Reiss *et al.* 1999b, section 2.7, we quantify the systematics plaguing the High-Z rates in table 4.6. The total systematic error is computed as the quadratic sum of the components listed in the table that have no (*). The ranges computed for the pa-

rameters marked with a (*) are listed for reference only. These include the effects of cosmology ($H_0, \Omega_{\rm M}$ and Ω_Λ), as well as different SN luminosity and reddening distributions that are not outside the realm of possibility. Also included is the additional systematic error describing the range in rates computed at different m_{cut}, as listed in table 4.4. We summarize, then, that we can constrain the SN Ia and core-collapse rates at a redshift of $\overline{z_{eff}} \simeq 0.49$, including statistical and systematic 1-σ uncertainties, as $r_{\rm Ia} = 0.278^{+0.091\ +0.098}_{-0.091\ -0.086}\,(H_0/65)^2$ SNu, and $r_{\rm II} \geq 0.423^{+0.31\ +0.33}_{-0.31\ -0.24}\,(H_0/65)^2$ SNu, respectively (the type-II rate being a lower limit).

4.6 Discussion

We summarize the SN Ia and core-collapse rates derived in this chapter with those computed from the MSACSS (Reiss *et al.* 1999b, Reiss *et al.* 1999a) in table 4.7. A comparison of the SN Ia rates derived from the MSACSS to that found here (as also viewed in figure 4.7) reveals that the high-redshift SN Ia rate is $\sim 50\%$ greater than in the nearby cluster and field rates. It is worthwhile to note that in a comparison of the high-z and low-z field rates, nearly all systematic uncertainties vanish to first order since they were both computed using the same assumptions throughout. A comparison with the cluster rates is still subject to some systematics (mostly based on the field vs. cluster galaxy control luminosity), although the most egregious ones still vanish. The fact that in such a comparison the SN Ia rate appears to have evolved over the past few Gyr implies that the lifetimes of their progenitors must be significantly less than the age of the universe. However, the SN Ia rate is not increasing (with redshift) as fast as is the SFR. This observation, when combined with the SN rate in clusters reported in Chapter 3, which suggests that SN Ia progenitor lifetimes cannot be extremely short, places weak lower *and* upper limits on their lifetimes. Since L_B traces, on average, stars with mean ages of $\sim$ 1Gyr, the implication is that SN Ia progenitors live for $\gtrsim$1Gyr. We can therefore conclude

that the mean lifetime of the progenitors of SNe Ia is on the order of a few time 10^9 years (Nomoto *et al.* 1999; Madau 1998; Sadat *et al.* 1998; Ruiz-Lapuente & Canal 1998).

Despite the fact that the high-redshift SN-II rate is a lower-limit, it is still higher than the cluster rate (Reiss *et al.* 1999a), while the low-redshift SN-II rate is significantly higher (Reiss *et al.* 1999b). Therefore, the core-collapse rate appears to be tracing, in some sense, the overall star-formation rate per unit L_B of its underlying galaxy population (in which field galaxies in general have a higher star-formation rate per B-band luminosity than cluster galaxies). On the other hand, the type-Ia SN rate (in SNu) remains approximately constant across all of these stellar populations, hinting that it traces a progenitor population whose majority changes more slowly than the SFR, as the underlying stellar population ages.

Models of SN Ia progenitors are still extremely uncertain, and their are a number of models which result in fise times of significantly different durations. Among the models considered by Nomoto *et al.* 1999, for example, a close white-dwarf–red-giant binary system progenitor is sufficient to result in progenitor ages $\gtrsim 10$ Gyr, whereas close white-dwarf–white-dwarf accretion progenitors (so-called "double-degenerate" [DD] systems) have lifetimes of $\lesssim 0.3$ Gyr. Kobayashi, Tsujimoto, & Nomoto 1999 suggest two paths for binaries which lead to SNe Ia – one with a long lifetime involving the accretion from a red giant (1-1.5 $M_\odot$ zero-age main sequence) onto a white dwarf, and another with accretion from an evolved main sequence star (2-3 $M_\odot$). This second path produces most of its SNe Ia within 1 Gyr, and therefore is probably not responsible for the majority of SNe which we observe today.

However, Ruiz-Lapuente, Canal, & Burkert 1996 suggest that DD progenitors' lifetimes are sufficient to provide a slow evolution of the SN Ia rates, as are other types of progenitors such as "symbiotic systems" which share mass through winds and ejection of planetary nebulae. Of course, any progenitor population could be a combination of any of these models. In fact, the results of this chapter when

combined with the rates measured in Chapter 2 and Chapter 3 may be reconciled with a population comprised of at least two different progenitors, one which is short-lived (and explains the decrease in SN Ia rates as the SFR decreased over the past few Gyr), and one which is long-lived (and explains the non-zero rate observed among elliptical galaxies (Cappellaro *et al.* 1997) and rich galaxy clusters). This interpretation is also entirely consistent with the observation of an enhancement of SNe Ia in the spiral arms of spiral galaxies (van den Bergh & McClure 9894), as well as the observation that only the most luminous SNe Ia (with the broadest light curves) occur in late-type galaxies, whereas both early-type and late-type galaxies provide hosts for fainter SNe Ia with narrower light curves (Hamuy *et al.* 1996a). The implication is that there is a short-lived SN Ia progenitor that also results in brighter exposions, while a population of longer-lived progenitors which produces dimmer explosions, also exsists. If such an interpretation of the SN Ia rates is to be true, we would expect that the large sample of higher-redshift SNe Ia will prove to contain broader light curves, on average, than their nearby counterparts.

This complex interpretation of the SN Ia rates does not bode well for using SNe Ia as an independent indicator of star-formation at high redshift. Rather, a complete sample of type-II SNe would be required to achieve this goal. This may be seen in the models of both Nomoto *et al.* 1999 and Sadat *et al.* 1998, which both predict that the rate of SNe Ia remain roughly constant with look-back time (to $z \lesssim 1.0$) whereas the core-collapse (type-II) SN rate is expected to increase by $\sim 50\%$ to $\sim 150\%$ at this redshift as the SFR increases.

By reporting the SN rates in SNu we are by definition comparing them to the evolution of the young stars in the control galaxies (*i.e.* the blue ones). This makes sense for the SNe II, but given these results which suggest that a large fraction of SNe Ia derive from an older stellar population, perhaps SNu are not the best units to use. We have also computed the High-z SN rates in SNu_R (per R-band luminosity of the host galaxies), following the precepts described in Chapter 2, section 2.5 in which

we used the local luminosity density derived from the Century (R-band; Geller *et al.* 1997) and Canada-France Redshift (Gunn-r; Lin *et al.* 1996) Surveys. We then scaled the luminosity density with redshift by interpolating between the two reported Lilly *et al.* 1996 exponents to derive $\mathcal{L}_R(z) \simeq 1.64 \times (1+z)^{1.4} \times 10^8 L_{R_\odot} \mathrm{Mpc}^{-3}$. Our R-band SN rates are 0.257 $(H_0/65)^2$ SNu_R for SNe Ia and 0.394 $(H_0/65)^2$ SNu_R for SNe II (with similar uncertainties to those derived in SNu above).

We have furthermore derived the rates per unit volume (by in effect estimating a *control volume* for our search rather than a control luminosity). We find rates of $(0.66 \pm 0.24)(H_0/65)$ SNv and $(0.92 \pm 0.92)(H_0/65)$ SNv, for SNe Ia and SNe II, in units of 1 SNv $\equiv$ 1 (Century $\times$ $[10^{-2}\mathrm{Mpc}^3]$)$^{-1}$. The effective redshifts for these measurements are 0.48 and 0.43, respectively. These rates may be compared to rates derived locally from the MSACSS (Chapter 2) of $(0.20 \pm 0.074)(H_0/65)$ (type-Ia) and $(1.37 \pm 0.67)(H_0/65)$ (type-II), in the same units. The comparison does reveal that the SN-Ia rate per unit volume, not surprisingly, increases significantly with redshift, following the same trend in galaxy luminosity density.

As hinted at in section 4.1, the results presented here are lower than the measurement of the SN Ia rate at $z \simeq 0.38$ of $0.35^{+0.23}_{-0.16}{}^{+0.16}_{-0.11}\,(H_0/65)^2$ SNu by Pain *et al.* 1996. Apparently a more recent measurement by Pain *et al* (as reported by Nomoto *et al.* 1999) reaches the conclusion that the SN Ia rate at $z \simeq 0.55$ is $\sim (0.3 \pm 0.1)\,(H_0/65)^2$ SNu (presumably including systematic uncertainties), which is more consistent with ours. It is questionable whether increasing the SN sample size by, for example, combining the samples of both the High-z and the Supernova Cosmology Project, will result in a significant decrease in the total uncertainty in the rates. Only by adding the requirement of complete spectroscopic and photometric completeness to these searches (perhaps in a search more dedicated to determining high-redshift SN rates rather than to simply detecting SNe Ia near b=peak brightness) will the statistical and systematic uncertainties be reduced beyond their current levels.

Table 4.2: The High-Z SN sample used throughout this paper. Continues on next page. See text for details.

SN	Type	Redshift	Mag. at discovery	Notes
1997cm	Ia	0.52	22.6	
1997cn	II?	0.28	23.7	
1997co	?	??	23.5	no spec.
1997cp	Ia	0.51	22.9	
1997cq	Ia	0.44	23.3	
1997cr	?	??	23.7	no spec.
1997cs	?	??	23.5	no spec.
1997ct	?	??	23.5	no spec.
1997cu	?	??	23.5	no spec.
1997cv	Ia	0.50	22.8	
1997cw	Ia	0.97	24.0	
–	QSO	1.03	23.7	
–	var?	??	23.8	red variable
1998F	?	0.52	24.5	
–	?	??	24.1	not a SN?
1998G	II?	0.31	22.8	
1998H	?	0.66	23.0	
1998I	Ia	0.89	23.6	
1998J	Ia	0.83	23.5	
1998K	?	??	23.8	no spec.
1998L	II?	??	23.6	
1998M	Ia	0.63	23.3	
1998N	?	0.26	23.1	
–	var?	??	20.5	variable star?
1998ac	Ia	0.46	23.7	
1998ad	II?	0.44	23.4	
–	?	??	24.0	no spec.
–	?	??	24.0	no spec.
1998ae	?	1.1	23.9	
–	?	??	23.1	no spec.
1998af	II	0.23	23.7	
1998ag	Ia	0.67	23.5	
–	?	??	23.4	no spec.
1998ah	Ia	0.43	22.6	
1998ai	Ia	0.49	22.7	
–	?	??	23.7	no spec.
1998aj	Ia	0.83	24.1	
1998ak	Ia?	0.74	23.7	
1998al	Ia?	0.71	23.4	
1998am	II	0.24	23.8	

Table 4.3: The High-Z SN sample used throughout this paper. Continued from previous page.

SN	Type	Redshift	Mag. at discovery	Notes
1999Q	Ia	0.46	22.29	
–	QSO?	??	23.52	not a SN
–	QSO?	??	23.43	not a SN
–	Ia?	0.60	22.87	
–	?	??	24.48	no spec.
1999R	Ia	0.68	23.53	
1999S	Ia	0.46	23.81	
1999T	Ia	0.69	24.05	
1999U	Ia	0.50	23.13	
1999V	II?	??	23.59	
–	QSO?	??	22.50	not a SN
1999W	II	0.12	23.40	
–	?	??	24.46	no spec.
1999K	II	0.037	21.47	
–	?	??	23.62	no spec.
–	?	??	24.33	no spec.
–	?	??	23.34	no spec.
–	?	0.91	23.43	
–	?	0.81	23.35	
1999L	Ia	0.65	23.20	
–	?	??	23.21	no spec.
–	QSO	??	23.73	
–	?	??	23.14	no spec.
1999M	Ia	0.50	23.43	
–	QSO?	??	23.24	not a SN
1999N	Ia	0.54	23.30	
–	QSO?	??	23.04	
1999O	II	0.21	24.09	
–	QSO?	1.61	22.41	
–	QSO?	1.80	24.70	
–	?	0.3?	22.94	
–	?	??	24.24	no spec.
1999P	Ib/c	0.06	21.81	
–	QSO?	??	23.84	not a SN
–	QSO?	??	22.34	not a SN
–	flare?	??	22.60	quick fade

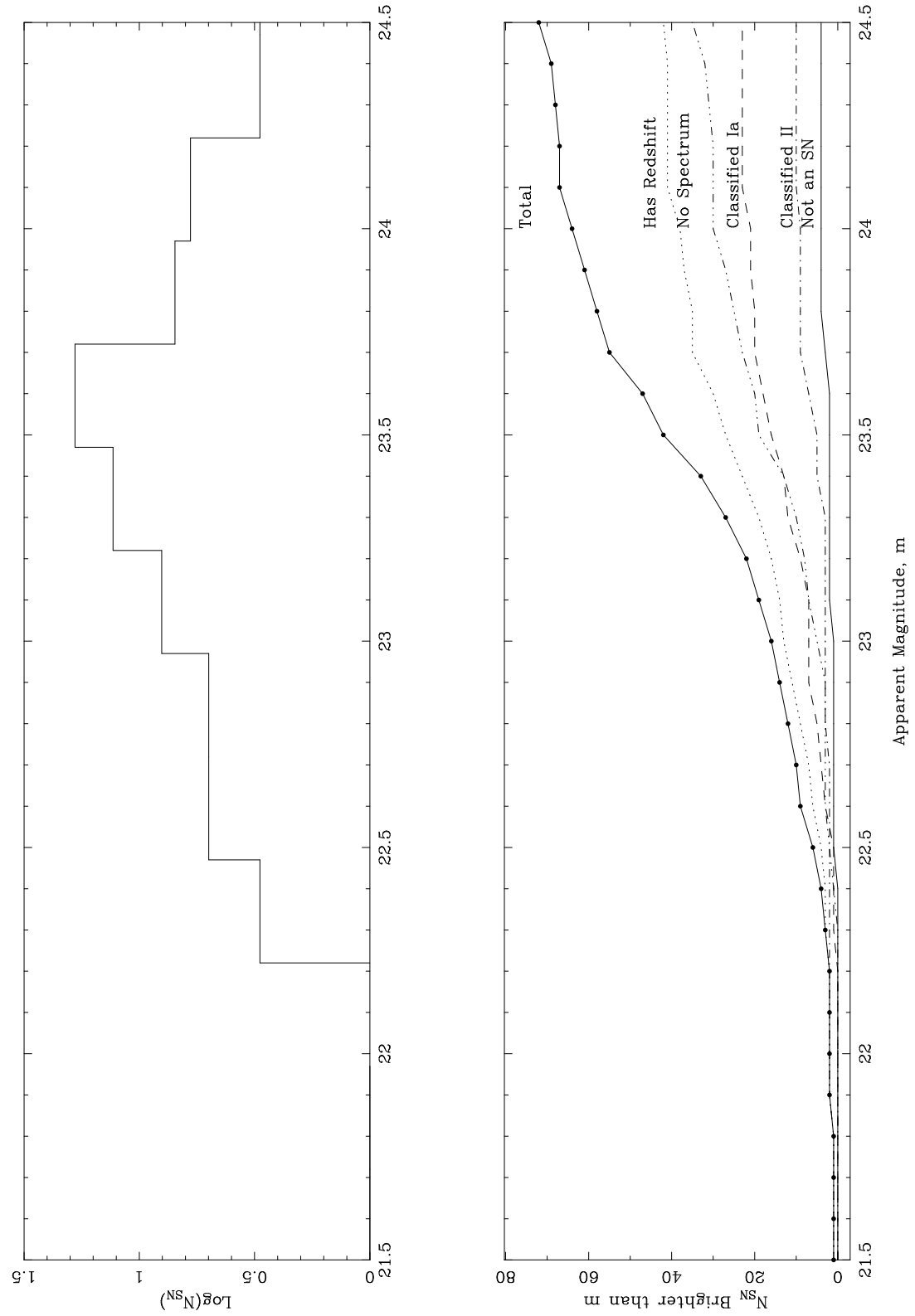

Figure 4.1: Global magnitude distributions of the High-Z SN sample used in this paper to determine SN rates. At top is a histogram of the objects' discovery magnitudes, with a clear peak at $m \simeq 23.5$; at bottom is the integrated distribution, revealing that only $\sim$ half of the objects are detected at $m \lesssim 23.5$; those at fainter magnitudes are not used here.

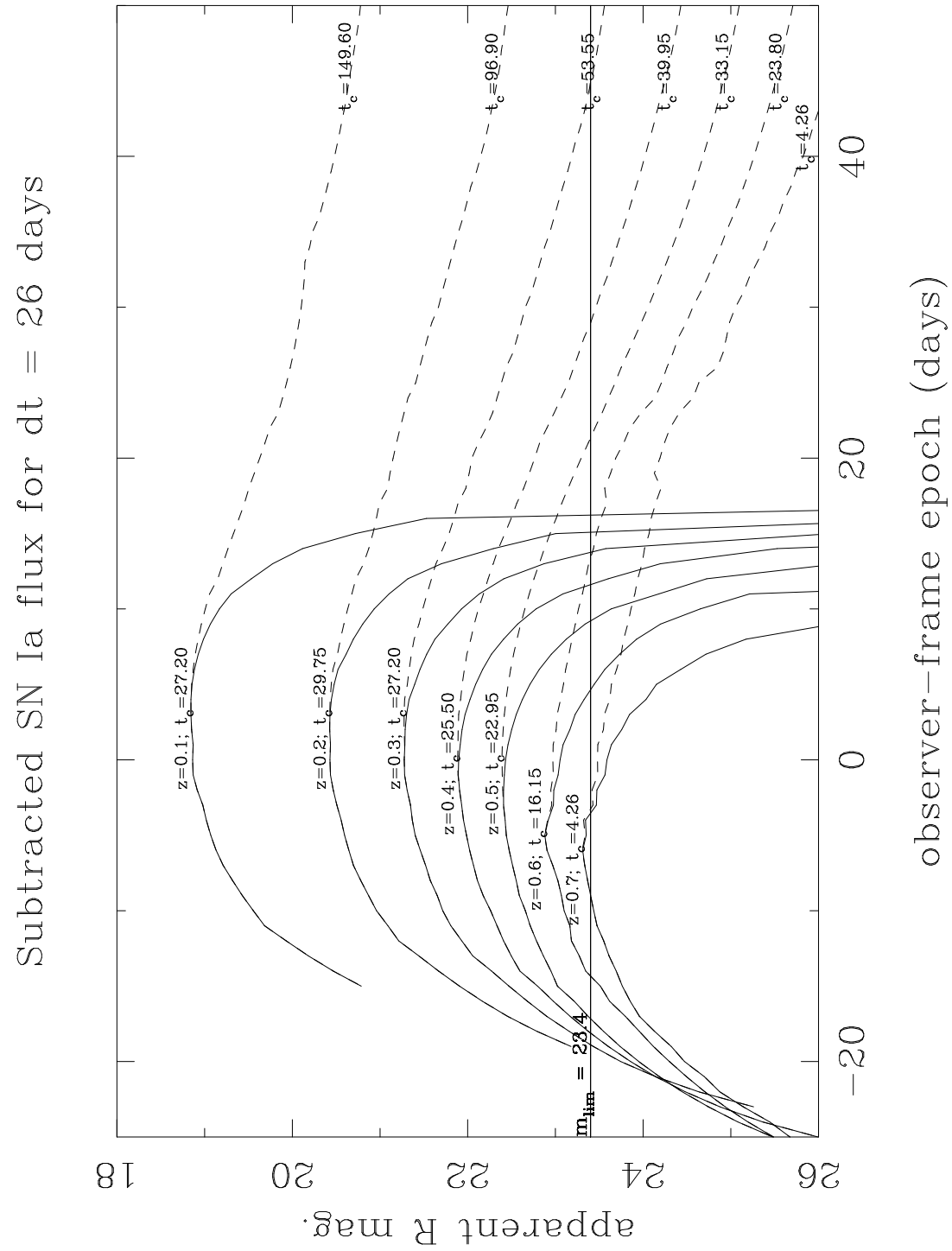

Figure 4.2: Control times for searches with $\Delta t = 26$ days (solid lines) and $\Delta t > 365$ days (dashed lines), at increasing redshift. Curves show the template-subtracted, observed SN-Ia light curves for each case. Computed control times for a limiting search magnitude of 23.4 are listed next to the respective light curves.

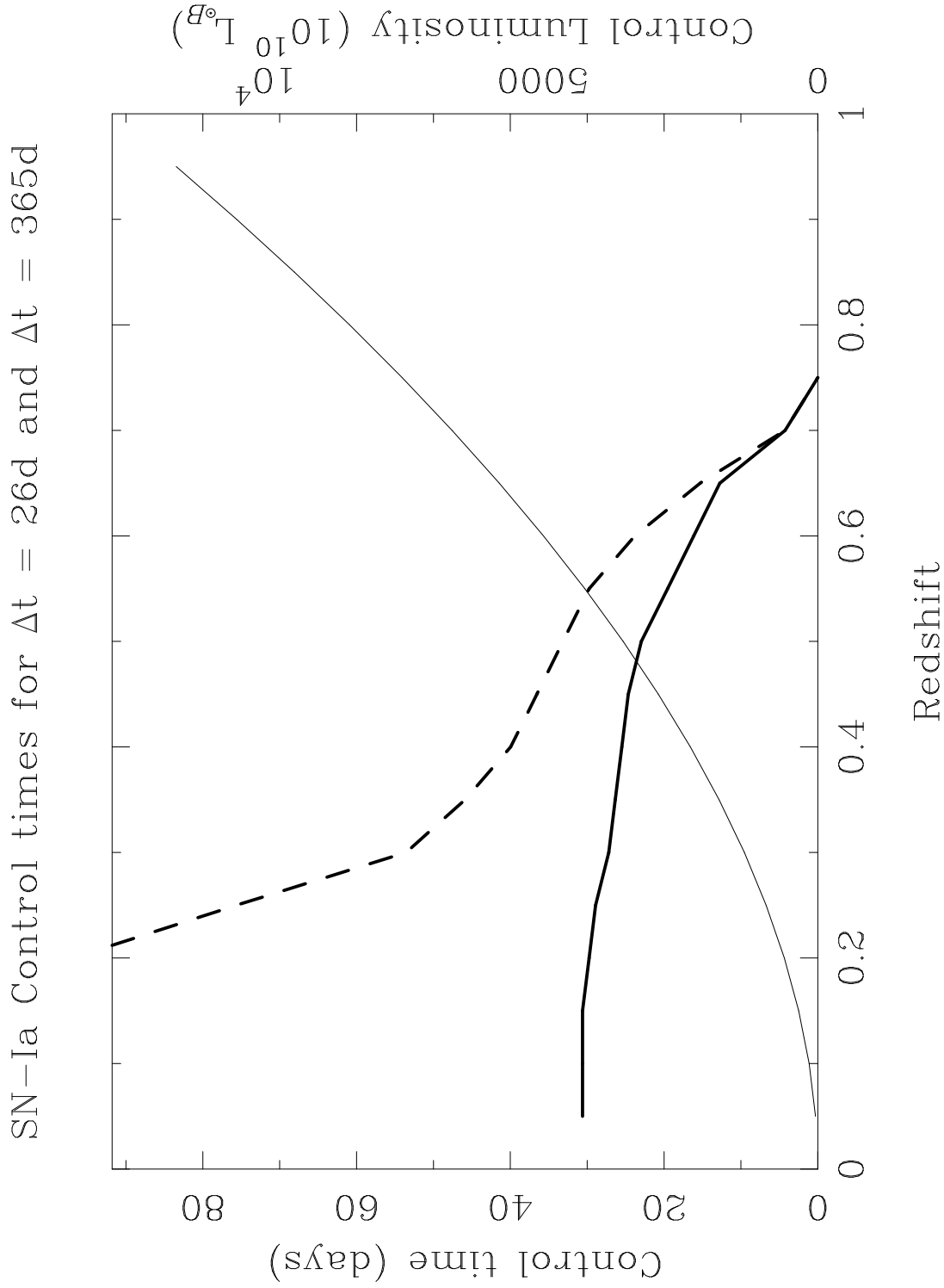

Figure 4.3: Control times for searches with $\Delta t = 26$ days (solid lines) and $\Delta t > 365$ days (dashed lines), as a function of redshift. Also shown is the total blue galaxy control luminosity over a 1 deg^2 field, integrated over 0.05 bins in redshift.

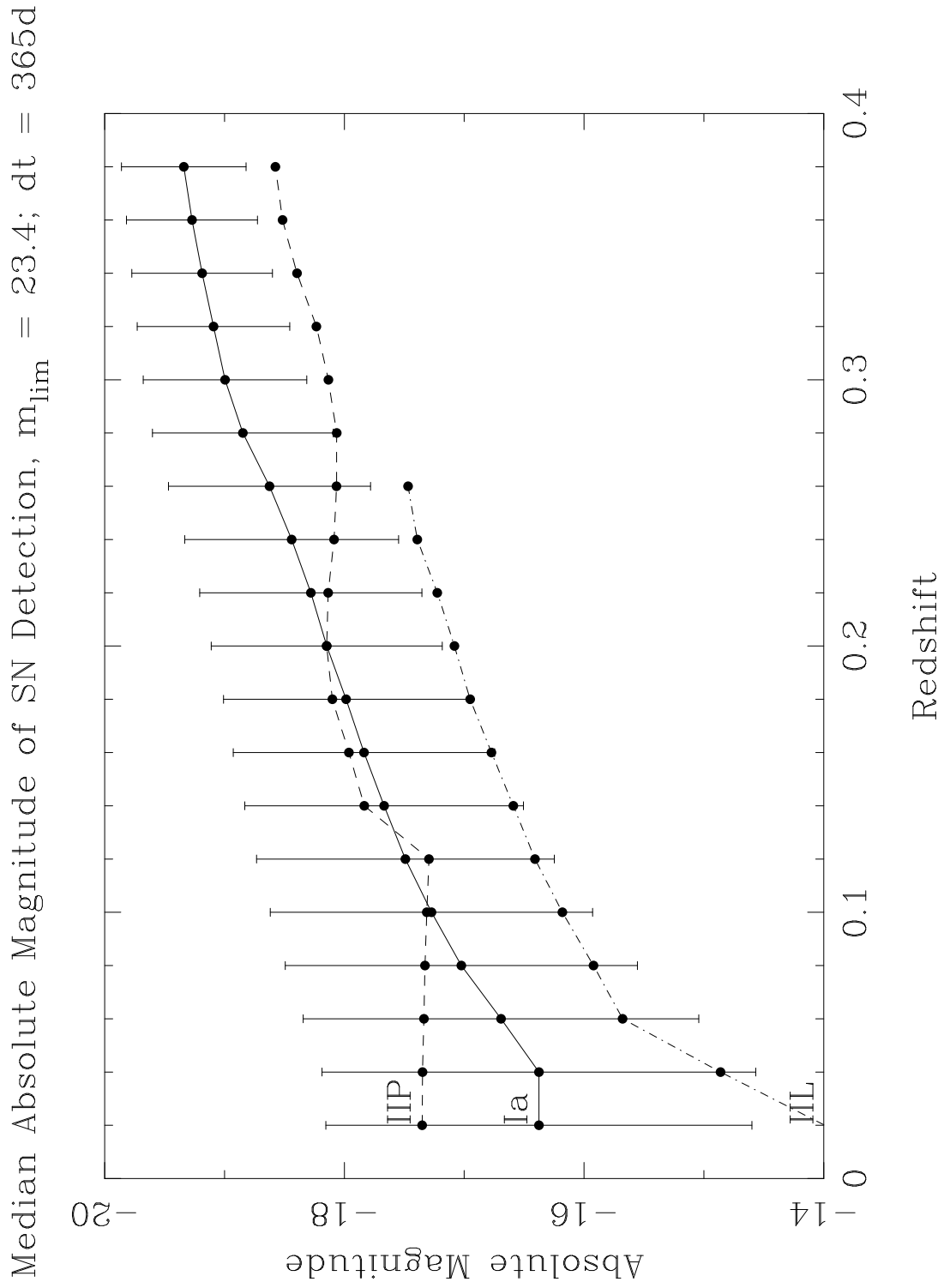

Figure 4.4: Median detection magnitudes of SNe as a function of redshift when the time between template and search observation is $\gtrsim$ 365 days.

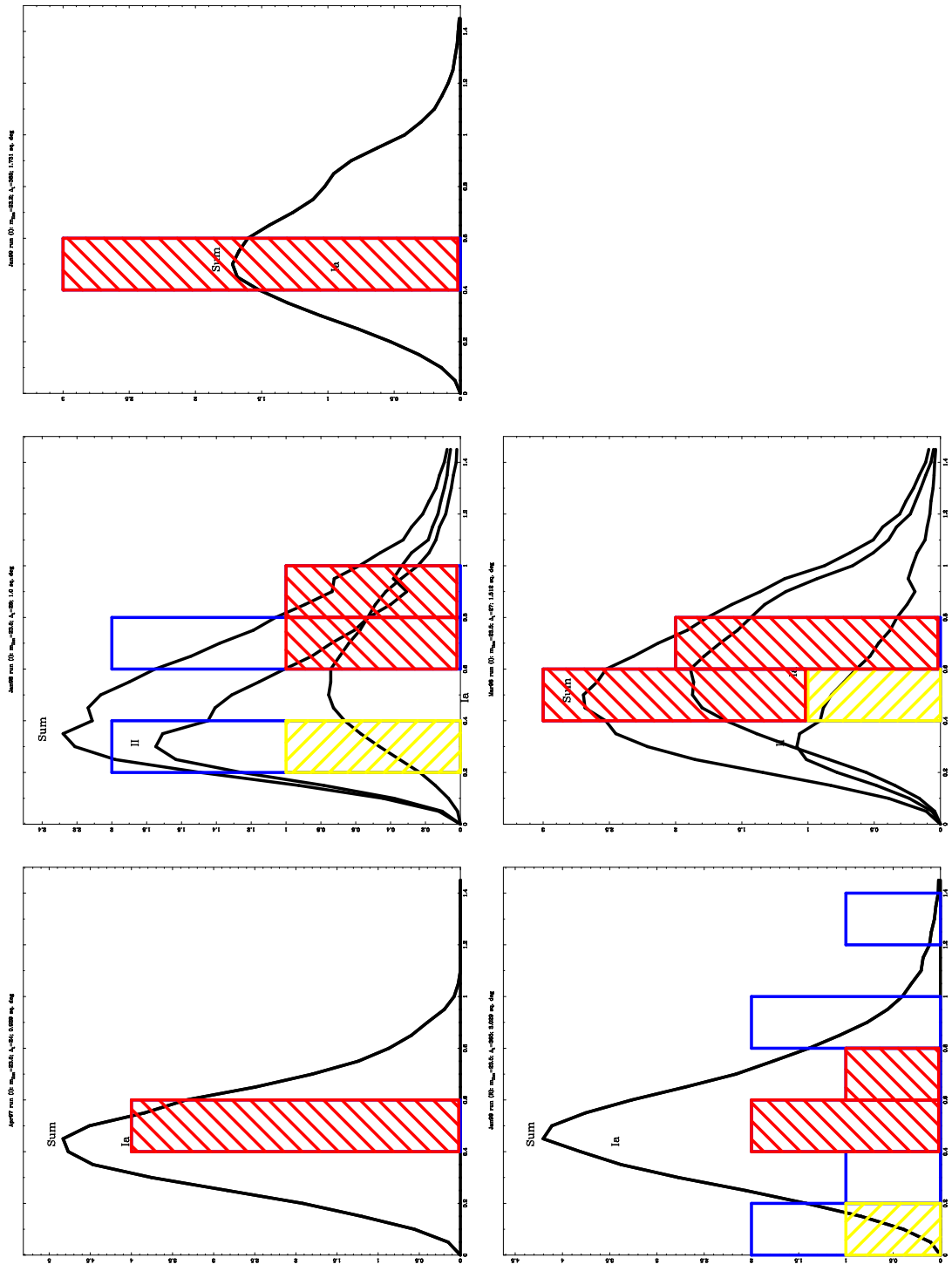

Figure 4.5: Predicted and observed redshift distributions of individual High-Z searches, analogous to figures 2.5 and 3.8.

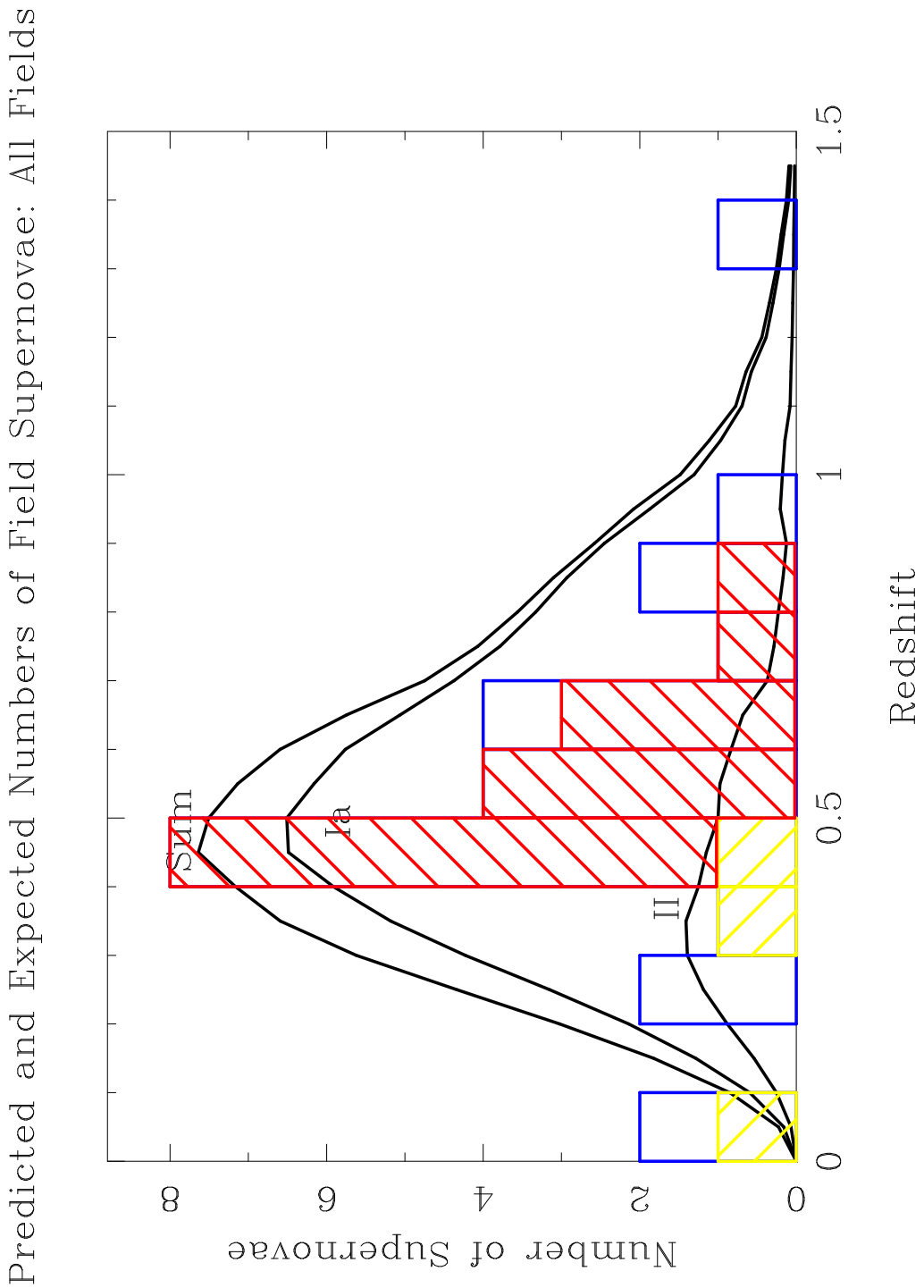

Figure 4.6: Predicted and observed redshift distributions over all five High-Z searches. See figure 4.5.

Table 4.4: The High-Z SN rates listed as a function of cutoff magnitude, m_{cut}. Also listed are the mean effective redshift of the SN sample, as well as some of its attributes at each cutoff magnitude.

m_{cut}	$\overline{z_{\rm eff}}(Ia)$	$\overline{z_{\rm eff}}(II)$	N_{SN}	$N_{\rm Ia}$	$N_{\rm II}$	no z	$r_{\rm Ia}$ (SNu)	Uncert.	$r_{\rm II}$ (SNu)	Uncert
23.0	0.472	0.437	16	7	3	5	0.184	0.080	0.384	0.320
23.1	0.476	0.440	19	7	3	7	0.212	0.083	0.329	0.333
23.2	0.480	0.443	22	9	3	8	0.249	0.087	0.273	0.334
23.3	0.484	0.445	27	12	3	10	0.242	0.091	0.455	0.368
23.4	0.488	0.448	33	13	5	13	0.288	0.093	0.446	0.402
23.5	0.491	0.450	42	16	5	19	0.278	0.091	0.423	0.393
23.6	0.494	0.453	47	18	7	20	0.288	0.100	0.561	0.438
23.7	0.496	0.455	55	20	9	23	0.278	0.098	0.525	0.407
23.8	0.499	0.458	58	20	9	25	0.265	0.103	0.486	0.365
23.9	0.501	0.460	61	21	9	27	0.265	0.099	0.265	0.370
24.0	0.503	0.463	64	21	9	30	0.253	0.097	0.253	0.332

Table 4.5: Statistical uncertainties in the High-Z SN rates: $\sqrt{N}$ statistical uncertainty, uncertainty due to possible mis-classification of SNe, and total uncertainty, in $(H_0/65)^2$ SNu.

SN Type	$\sigma_{\rm stat}$	$\sigma'_{\rm stat}$	$\sigma_{\rm tot}$
Ia	0.052	0.021	0.091
II	0.75	0.67	0.71

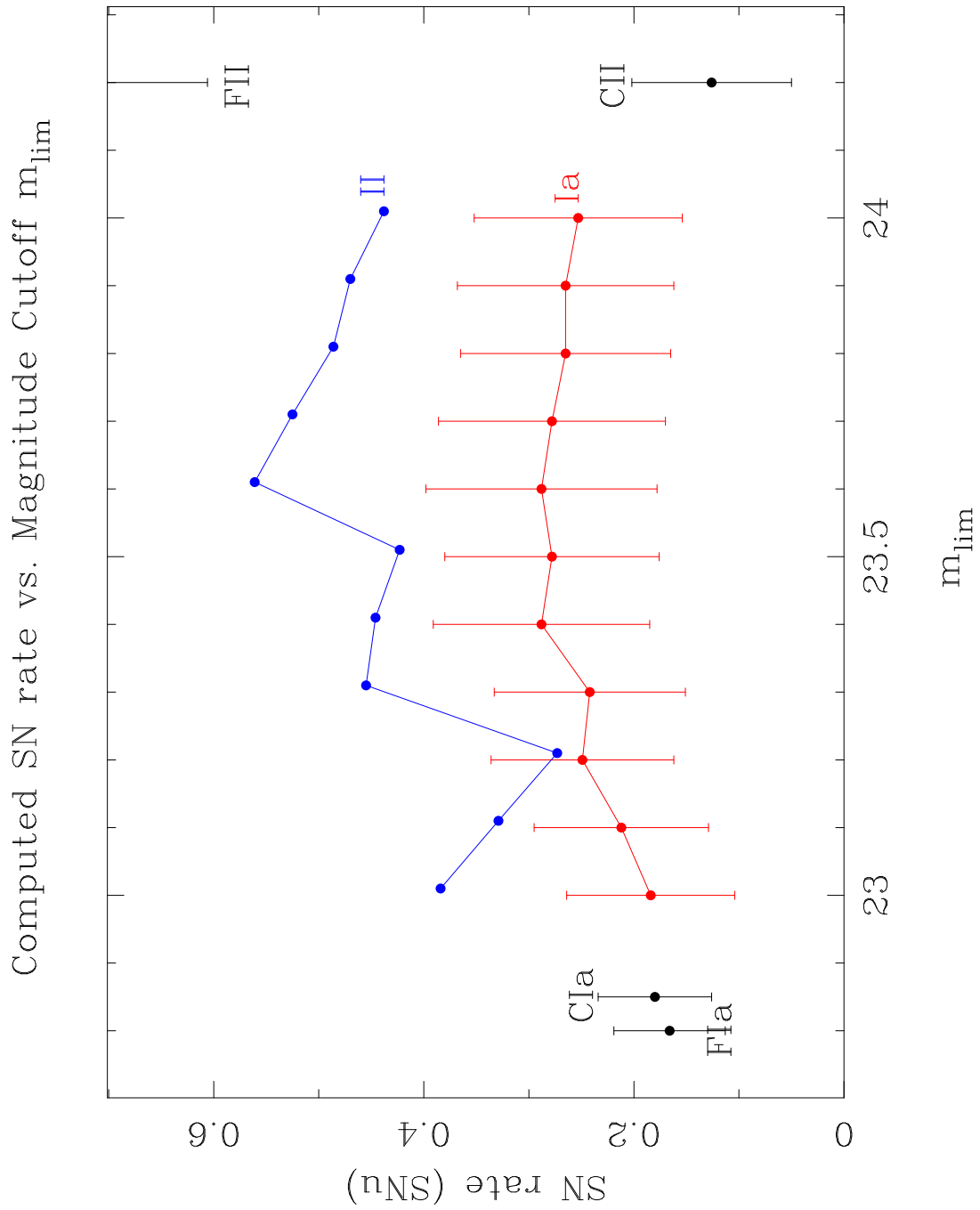

Figure 4.7: High-Z SN-Ia and -II (core-collapse; lower limit only) rates graphed as a function of cutoff magnitude. Also shown for comparison are the nearby field (F) and cluster (C) SN rates computed from the MSACSS (papers Chapter 2 and Chapter 3, respectively); the field type-II rate is off the chart at 0.896 SNu.

Table 4.6: Systematic uncertainty in the High-Z SN rates: parameters contributing to the uncertainty, the values used to compute the rates, ranges in those parameters, and resulting ranges in SN rates (SNu). The total systematic error is the quadratic sum of all listed contributions except for those marked by an (*).

Parameter	Value	+ limit	- limit	Ia Uncert.		II Uncert.	
H_0 (km sec^{-1} Mpc^{-1})(*)	65	+10	-10	+0.068	-0.058	+0.105	-0.090
$\Omega_{\rm M}$, Ω_Λ(*)	0.3, 0.7	1.0, 0.0	–	+0.000	-0.102	+0.000	-0.084
$\Omega_{\rm M}$, Ω_Λ(*)	0.3, 0.7	0.3, 0.0	–	+0.000	-0.061	+0.000	-0.046
$\mathcal{L}_{B,\rm local}(h \times 10^8 L_\odot Mpc^{-3})$	2.00	+0.2	-0.2	+0.024	-0.018	+0.036	-0.029
α_L	2.7	+0.5	-0.5	+0.045	-0.037	+0.048	-0.043
$\overline{M}_{B,\rm Ia}$ (mag)	-19.33	+0.2	-0.2	+0.076	-0.055	+0.005	-0.001
$\overline{\sigma}_{\Delta,\rm Ia}$ (mag)	0.30	+0.05	-0.05	+0.010	-0.007	+0.002	-0.001
Gaussian $F_{\rm Ia}(E_{B-V})$ w/ $\sigma = 0.3$ mag				+0.000	-0.066	+0.005	-0.000
Gaussian $F_{\rm Ia}(E_{B-V})$ w/ $\sigma = 0.5$ mag(*)				+0.000	-0.038	+0.002	-0.000
No SN Ia extinction (delta-func. at $E_{BV} = 0$)(*)				+0.000	-0.089	+0.007	-0.000
$\overline{M}_{B,\rm II-P}$; $\overline{M}_{B,\rm II-L}$ (mag)	-17.0, -18.0	+0.5	-0.5	+0.000	-0.004	+0.192	-0.115
$\overline{\sigma}_{\Delta,\rm II}$ (mag)	1.75	+0.5	-0.5	+0.003	-0.001	+0.195	-0.113
$\overline{A_{V,\rm II}}$ (mag)	1.0	+0.5	-0.5	+0.003	-0.001	+0.116	-0.103
$\sigma_{A_V,\rm II}$ (mag)	1.0	+0.5	-0.5	+0.001	-0.000	+0.037	-0.000
$\overline{A_{V,\rm II}} = 0.6$ mag; $\sigma_{A_V,\rm II} = 0.75$ mag(*)				+0.000	-0.001	+0.000	-0.079
m_{cut} (mag)	23.3	+0.5	-0.5	+0.026	-0.026	+0.067	-0.067
area searched (% of image)	98%	+3%	-3%	+0.001	-0.001	+0.002	-0.002
Total				+0.098	-0.086	+0.332	-0.244

Table 4.7: The SN rates derived from the MSACSS and the High-z SN searches

Sample	$\overline{z_{eff}}$ (Ia)	$r_{\rm Ia}$($(H_0/65)^2$ SNu)	$\overline{z_{eff}}$ (II)	$r_{\rm II}$($(H_0/65)^2$ SNu)
MSACSS, cluster	0.060	$0.180^{+0.054\ +0.046}_{-0.054\ -0.058}$	0.057	$0.124^{+0.076\ +0.085}_{-0.076\ -0.052}$
MSACSS, field	0.114	$0.164^{+0.058\ +0.050}_{-0.058\ -0.056}$	0.084	$0.997^{+0.54\ +1.21}_{-0.54\ -0.47}$
High-z	0.488	$0.278^{+0.091\ +0.098}_{-0.091\ -0.086}$	0.448	$> 0.423^{+0.31\ +0.33}_{-0.31\ -0.24}$

REFERENCES

Abell, G. O. 1958, Astrophys. J. Supp. Series, 3, 211.

Abell, G. O., Corwin, H. G., J., & Olowin, R. P. 1989, Astrophys. J. Supp. Series, 70, 1.

Adams, M. T., Howell, D. A., Ward, M. H., Wheeler, J. C., & Wren, W. 1997, IAU Circ, 6674.

Barbon, R., Ciatti, F., & Rosino, L. 1982, Astr. Astrophys., 116, 1.

Barbuy, B., de Freitas Pacheco, J. A., & Castro, S. 1994, Astr. Astrophys., 283, 32.

Bertin, E. & Arnouts, S. 1996, Astr. Astrophys., 117, 393.

Bessell, M. & Germany, L. M. 1999, apj, *submitted*.

Branchini, E., Plionis, M., & Sciama, D. W. 1996, Astrophys. J., 461, L17.

Cappellaro, E., Evans, R., & Turatto, M. 1999, submitted (astro-ph/9904225).

Cappellaro, E., Turatto, M., Benetti, S., Tsvetkov, D. Y., Bartunov, O. S., & Makarova, I. N. 1993a, Astr. Astrophys., .

Cappellaro, E., Turatto, M., Benetti, S., Tsvetkov, D. Y., Bartunov, O. S., & Makarova, I. N. 1993b, Astr. Astrophys., .

Cappellaro, E., Turatto, M., Tsvetkov, D. Y., Bartunov, O. S., Pollas, C., Evans, R., & Hamuy, M. 1997, Astr. Astrophys., 322, 431.

Carroll, S. M., Press, W. H., & Turner, E. L. 1992, Ann. Rev. Astr. Ap., 30, 499.

Ciardullo, R., Tamblyn, P., & Phillips, A. C. 1990, Publ. Astr. Soc. Pacific, 1113, 102.

Colless, M. 1995, Astron. J., 109, 1937.

d. Li, W., l. Qiu, Y., y. Qiao, Q., Zhang, Y., Zhou, W., & y. Hu, J. 1997, *IAU Circ #6661.*

de Vaucouleurs, G., de Vaucouleurs, A., Corwin, H. G., Buta, R. J., Paturel, G., & Fouqué, P. 1991, Third Reference Catalogue of Bright Galaxies, (Berlin: Springer).

Dressler, A. 1980, Astrophys. J., 236, 351.

Ebeling, H. *et al.* 1996, Mon. Not. R. astr. Soc., 281, 799.

Evans, C. R. & Kochanek, C. S. 1989, Astrophys. J., 346, L13.

Evans, R. 1997, *IAU Circ #6613.*

Feldman, H. A. & Watkins, R. 1994, Astrophys. J., 430, l17.

Ferguson, H. C., Tanvir, N. R., & Von Hippel, T. 1998, Nature, 391, 461.

Fixsen, D. J. *et al.* 1994, Astrophys. J., 420, 445.

Fukugita, M., Hogan, C. J., & Peebles, P. J. K. 1998, Astrophys. J., 503, 518.

Fukugita, M., Shimasaku, K., & Ichikawa, T. 1995, Publ. Astr. Soc. Pacific, 197, 945.

Gaidos, E. J. 1997, Astron. J., 113, 117.

Garilli, B., Maccagni, D., & Andreon, S. 1999, Astr. Astrophys., 342, 408.

Geller, M. J. *et al.* 1997, Astron. J., 114, 2205.

Germany, L. M., Reiss, D. J., Sadler, E. M., Schmidt, B. P., & Stubbs, C. W. 1999, pasp, *submitted.*

Giovanelli, R., Haynes, M. P., Wegner, G., Da Costa, L. N., Freudling, W., & Salzer, J. J. 1996, Astrophys. J., 464, L99.

Goldhaber, G. 1998, Bull. American Astron. Soc., 193, 4713.

Graham, A. W. 1996, Astrophys. J., 459, 27.

Gramann, M., Bahcall, N. A., Cen, R., & Gott, J. R. 1995, Astrophys. J., 441, 449.

Groth, E. J. 1986, Astron. J., 91, 1244.

Hamuy, M., Phillips, M. M., Suntzeff, N. B., Schommer, R. A., Maza, J., & Aviles, R. 1996a, Astron. J., 112, 239.

Hamuy, M. & Pinto, P. A. 1999, Astron. J., 117, 1185.

Hamuy, M. *et al.* 1995, Astron. J., 109, 1.

Hamuy, M. *et al.* 1996b, Astron. J., 112, 2391.

Hamuy, M. *et al.* 1996c, Astron. J., 112, 2408.

Hart, J. *et al.* 1996, Publ. Astr. Soc. Pacific, 108, 220.

Hatano, K., Branch, D., & Deaton, J. 1998, Astrophys. J., 502, 177.

Hudson, M. J. & Ebeling, H. 1997, Astrophys. J., 479, 621.

Irwin, M. J. 1985, Mon. Not. R. astr. Soc., 214, 575.

Jha, S. *et al.* 1999, submitted (astro-ph/9906220).

Jorgensen, I. 1994, Publ. Astr. Soc. Pacific, 106, 967.

Kennicutt, R. C. 1992, Astrophys. J. Supp. Series, 79, 255.

Kennicutt, R. C. *et al.* 1984, Astrophys. J., 287, 116.

Kim, A., Goobar, A., & Perlmutter, S. 1996, Publ. Astr. Soc. Pacific, 108, 190.

Kim, A, G. A. & Perlmutter, S. 1996, Publ. Astr. Soc. Pacific, 108, 190.

Kobayashi, C., Tsujimoto, T., & Nomoto, K. 1999, submitted (astro-ph/9908005).

Kochanek, C. S. 1997, Astrophys. J., 491, 13.

Kolatt, T. S. & Bartelmann, M. 1998, Mon. Not. R. astr. Soc., 276, 763.

Landolt, A. 1992, Astron. J., 104, 372.

Lauer, T. R. & Postman, M. 1994, Astrophys. J., 425, 418. [LP].

Lilly, S. J., Le Fèvre, O., Hammer, F., & Crampton, D. 1996, Astrophys. J., 460, L1.

Lilly, S. J., Tresse, L., Hammer, F., Crampton, D., & Le Fèvre, O. 1995, Astrophys. J., 455, 108.

Lin, H. *et al.* 1996, Astrophys. J., 464, 60.

Loveday, J., Peterson, B. A., Efstathiou, G., & Maddox, S. J. 1992, Astrophys. J., 390, 338.

Lumsden, S. L. *et al.* 1997, Mon. Not. R. astr. Soc., 290, 111.

Madau, P. 1998, Mon. Not. R. astr. Soc., 297, 17.

Magnier, E. A. *et al.* 1997, Mon. Not. R. astr. Soc., 292, 490.

Martin, R., Williams, A., & Woodings, S. 1997, *IAU Circ #6558.*

Marzke, R. O., Geller, M. J., da Costa L. N., & Huchra, J. P. 1995, Astron. J., 110, 447.

Marzke, R. O., Huchra, J. P., & Geller, M. J. 1994, Astrophys. J., 428, 43.

Maza, J. 1997, IAU Circ, 6531.

McCall *et al.* 1985, Astrophys. J. Supp. Series, 51, 1.

Menzies, J. W. 1988, Proceedings of the Astronomical Society of Australia, 7, 401.

Metcalfe, N., Shanks, T., Fong, R., & Jones, L. R. 1991, Mon. Not. R. astr. Soc., 249, 498.

Metzger, M. R., Luppino, G. A., & Miyazaki, S. 1995, Bull. American Astron. Soc., 187, 7305.

Miller, D. L. & Branch, D. 1990, Astron. J., 100, 530.

Nagataki, S. & Sato, K. 1998, Astrophys. J., 504, 629.

Nomoto, K. *et al.* 1999, submitted (astro-ph/9907386).

Norgaard-Nielsen, H. U. *et al.* 1989, Nature, 339, 523.

Pain, R. *et al.* 1996, Astrophys. J., 473, 356.

Patat, F., Barbon, R., Cappellaro, E., & Turatto, M. 1993, Astr. Astrophys. Suppl. Ser., 98, 443.

Perlmutter, S. *et al.* 1995, Astrophys. J., 440, L41.

Perlmutter, S. *et al.* 1997, Astrophys. J., 483, 595.

Phillips, A. C. & Davis, L. E. 1995, in Astronomical Data Analysis Software and Systems IV, ed. R.A. Shaw, H.E. Payne, & J.J.E. Hayes, volume 77 of ASP Conference Series, 297.

Phillips, M. M. 1993, Astrophys. J., 413, L105.

Phillips, M. M., Hamuy, M., Heathcote, S. R., Suntzeff, N. B., & Kirhakos, S. 1990, Astron. J., 99, 1133.

Popov, D. V. 1993, Astrophys. J., 414, 712.

Postman, M., Lauer, T. R., & Strauss, M. A., *Private Communication.*

Press, W. J. & Schechter, P. L. 1974, Astrophys. J., 187, 425.

Reiss, D. J., Germany, L. M., Schmidt, B. P., & Stubbs, C. W. 1998, Astron. J., 115, 26. (Chapter 1).

Reiss, D. J., Germany, L. M., Schmidt, B. P., & Stubbs, C. W. 1999a, *submitted to A. J.* (Chapter 3).

Reiss, D. J., Germany, L. M., Schmidt, B. P., & Stubbs, C. W. 1999b, *submitted to A.J.* (Chapter 2).

Reiss, D. J., Germany, L. M., Schmidt, B. P., & Stubbs, C. W. 1999c, *submitted to A. J.* (Chapter 4).

Renzini, A. 1998, submitted (astro-ph/9801209).

Riess, A., Press, B., & Kirshner, R. P. 1995a, Astrophys. J., 438, L17.

Riess, A., Press, B., & Kirshner, R. P. 1995b, Astrophys. J., 445, L91.

Riess, A., Press, B., & Kirshner, R. P. 1996, Astrophys. J., 473, 88.

Riess, A. G., Davis, M., Baker, J., & Kirshner, R. P. 1997, Astrophys. J., 488, 1.

Riess, A. G., Filippenko, A. V., Li, W., & Schmidt, B. P. 1999a, submitted (astro-ph/9907038).

Riess, A. G. *et al.* 1998, Astron. J., 116, 1009.

Riess, A. G. *et al.* 1999b, submitted (astro-ph/9907037).

Ruiz-Lapuente, P. & Canal, R. 1998, submitted (astro-ph/9801141).

Ruiz-Lapuente, P., Canal, R., & Burkert, A. 1996, submitted (astro-ph/9609078).

Sadat, R., Blanchard, A., Guiderdoni, B., & Silk, J. 1998, Astr. Astrophys., 311L, 69.

Schechter, P. L. 1976, Astrophys. J., 203, 297.

Schechter, P. L. & Dressler, A. 1987, Astron. J., 94, 563.

Schechter, P. L., Mateo, M., & Saha, A. 1993, Publ. Astr. Soc. Pacific, 105, 1342.

Schlegel, D., Finkbeiner, D., & Davis, M. 1998, Astrophys. J., 500, 525.

Schmidt, B. P., Kirshner, R. P., & Eastman, R. G. 1992, Astrophys. J., 395, 366.

Schmidt, B. P. *et al.* 1993, Astron. J., 105, 2236.

Schmidt, B. P. *et al.* 1994, Astrophys. J., 432, 42.

Schmidt, B. P. *et al.* 1997, Bull. American Astron. Soc., 189(108).

Schmidt, B. P. *et al.* 1998, Astrophys. J., 507, 46.

Schmitz, M. F. & Gaskel, C. M. 1988, in Supernova 1987A in the Large Magellanic Cloud, p. 112.

Scowen *et al.* 1992, Astron. J., 104, 1.

Strauss, M. A., Cen, R., Ostriker, J. P., Lauer, T. R., & Postman, M. 1995, Astrophys. J., 444, 507.

Stubbs, C. W. *et al.* 1993, in Proceedings of the SPIE, volume 192, 1900.

Tammann, G. A. 1990, in Supernovae, ed. S. A. Bludman, R. Mochkovitch, & J. Zinn-Justin, Les Houches, 3.

Tammann, G. A. & Reindl, B. 1999, submitted (astro-ph/9903220).

Treffers, R. R., Peng, C. Y., Filippenko, A. V., & Richmond, M. W. 1997, IAU Circ, 6627.

Valotto, C. A. *et al.* 1997, Astrophys. J., 479, 90.

van den Bergh, S. 1990, Astron. J., 113, 197.

van den Bergh, S. & McClure, R. D. 19894, Astrophys. J., 425, 95.

van den Bergh, S., McClure, R. D., & Evans, R. 1987, Astrophys. J., 323, 44.

van den Bergh, S. & Tammann, G. A. 1991, Ann. Rev. Astr. Ap., 29, 363.

Watkins, R. & Feldman, H. A. 1995, Astrophys. J., 453, L73.

Wittman, D. M. *et al.* 1998, Proc. SPIE, 3355, 626.

Zwicky, F. 1938, Astrophys. J., 88, 529.

Zwicky, F. 1942, Astrophys. J., 96, 28.